



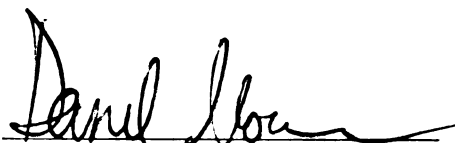
This is to certify that the
dissertation entitled
**A Time-Resolved Study of Electron Transfer
Mechanisms: Beyond Outer-Sphere Electron Transfer**

presented by

Claudia Turro

has been accepted towards fulfillment
of the requirements for

PhD degree in Chemistry


Major professor

Date August 27, 1992

LIBRARY
Michigan State
University

PLACE IN RETURN BOX to remove this checkout from your record.
TO AVOID FINES return on or before date due.

| DATE DUE | DATE DUE | DATE DUE |
|-----------------|-----------------|-----------------|
| _____ | _____ | _____ |
| _____ | _____ | _____ |
| _____ | _____ | _____ |
| _____ | _____ | _____ |
| _____ | _____ | _____ |
| _____ | _____ | _____ |
| _____ | _____ | _____ |

MSU is An Affirmative Action/Equal Opportunity Institution

**A TIME-RESOLVED STUDY OF ELECTRON TRANSFER
MECHANISMS: BEYOND OUTER-SPHERE ELECTRON TRANSFER**

By

Claudia Turró

A DISSERTATION

**Submitted to
Michigan State University
in partial fulfillment of the requirements
for the degree of**

DOCTOR OF PHILOSOPHY

Department of Chemistry

1992

ABSTRACT

A TIME-RESOLVED STUDY OF ELECTRON TRANSFER MECHANISMS: BEYOND OUTER-SPHERE ELECTRON TRANSFER

By

Claudia Turró

One of the primary objectives of our research has been to understand some of the fundamental mechanistic issues underlying electron transfer reactions. We have designed molecular systems to provide information on several aspects of charge transfer reactions, including the role of protons in long-distance electron transfer, bimolecular donor/acceptor pair reactivity at high driving forces, and excited state multielectron transformations. In our systems a photon can initiate the reaction by placing the molecules in an excited electronic state, which permits the reactant and product concentrations to be monitored as a function of time. These dynamic measurements are conducted by exciting the molecules with a short light pulse, and following the progress of the reaction by optical methods, such as transient absorption spectroscopy and emission lifetime.

Electron transfer reactions through a proton interface have been conducted by the design of hydrogen-bonded donor/acceptor pairs, where the donor, a carboxylic acid derivative of a Zn-substituted porphyrin, transfers an electron to several aromatic acceptors from its excited state. The charge separation and subsequent charge recombination rates have been determined utilizing picosecond transient absorption spectroscopy, for

protiated and deuterated donors and acceptors. A slight attenuation in the rates is observed, as compared to through-bond electron transfer.

The transient absorption technique has also been utilized to characterize the excited states that lead to two-electron reactivity in quadruply-bonded inorganic complexes of the type $M_2Cl_4(L)_n$, where M = molybdenum or tungsten and L = monodentate ($n = 4$) or bidentate ($n = 2$) phosphine ligands. It was observed that the reactions do not proceed directly from an excited electronic state, but from a conformationally-distorted intermediate formed following light excitation. The distorted intermediate is believed to possess favorable characteristics that permit the observed two-electron oxidative-addition reactions.

The driving force dependence of the bimolecular electron transfer rates between Ru^{II} complexes and cytochrome *c* has been determined. A decrease in charge separation rate at high driving forces, the inverted region, was observed for this donor/acceptor series, which is unusual in bimolecular reactions. The factors that govern bimolecular inverted region behavior have been considered.

ACKNOWLEDGMENTS

The work presented here would have never been possible without the people and atmosphere at Michigan State. In my *several* years here, I have learned much more than science.

In the absence of the technical help from the machine shop, the glass shop, and electronic shop, I would have been here a lot longer. Without Marty's wonderfully orchestrated pulsed devices none of the measurements presented here would have been possible. I've had many helpful discussions and collaborations with several MSU professors, including Shelagh Ferguson-Miller on proteins, Cukier on ET theory, Wagner on photochemistry, and Laser Lab faculty such as Jerry Babcock and Kris Berglund on qualitative and quantitative beer drinking skills.

I want to especially thank Colleen Partigianoni for introducing me to photochemical processes of quadruply-bonded compounds. Colleen was also known for doing unexpected things anytime, anyplace, which kept things interesting. Janice Kadis has told me (and the whole world) things I never thought physically possible, and Carolyn Hsu believed it all. Many interesting discussions flourished on Friday afternoons while at Lab Happy Hour, a tradition started by Randy King, which still lingers, now led by Doug Motry, JP Kirby, and Sara Helvoight - if she really joins the group. Which brings us to group parties: Zoe Pikraminou and Mark Torgerson were responsible for some of the finest. Mark Newsham helped me build my first instrument, and introduced me to the Nocera group (good?).

I also got to know a few people while here and to learn from them. Jeong-A Yu attempted to teach me Korean, and Tony Oertling showed me,

in a practical manner, to drink tequila with “a little salt and lime” while watching 4th of July fireworks from the roof of the Chemistry building (not everything I learned was good). The friendships of José Centeno, Juan López-Carriga, Hak-Hyun Nam, Elaine Hamon, Julie Jackson, and Renne Day were also invaluable. Friendships began and creativity peaked at establishments such as The Peanut Barrel, Harrison RoadHouse, The Green Door, Trippers, Dags, and the old Babbock group hangout, Cabaret.

The scientific insight and thoughtful guidance of George Leroi and Dan Nocera, along with their friendship have provided the underpinnings and shaped my graduate career. George always had words of wisdom and encouragement. Dan invariably had words, not necessarily wise or encouraging, but usually sincere and forceful.

Special friends, whose contributions range too far to be mentioned, are Sandy Nelson and Mariangel Gasalla. The support, love, and patience of my family has been invaluable. Their understanding of the short and far between visits is commendable. Seeing my family was always refreshing and provided new strength. They always encouraged me to continue in the pursuit of my scientific endeavors, although I know it was hard for them to understand why they took so long and occupied so much of my time.

The most important collaboration here, in more than one sense, was that with Jeff. We tripped over the same picosecond barriers, but always (somehow), we were able to help each other go on - especially in the early days, when nothing worked and our spectra were upsidedown. Once we had data, our scientific discussions became routine, using each other as “The Guide of Fast Phenomena and Excited State Processes”. Without him, the ps TA would probably still have crosstalk, the saturable absorber still be misaligned, and the continuum uncollimated. However, the friendship that grew from this, with him and his family, is by far more important. Without him, things would have been very different.

TABLE OF CONTENTS

| | | |
|----------------------|---|-----|
| LIST OF TABLES..... | viii | |
| LIST OF FIGURES..... | x | |
| INTRODUCTION..... | 1 | |
| References..... | 6 | |
| CHAPTER I | ELECTRON TRANSFER THROUGH HYDROGEN BONDED INTERFACES..... | 8 |
| | A. BACKGROUND..... | 8 |
| | B. EXPERIMENTAL METHODS..... | 18 |
| | C. RESULTS AND DISCUSSION..... | 28 |
| | 1. Electron Transfer in 1-H and 1-D..... | 28 |
| | 2. Electron Transfer in Systems 2 and 3..... | 49 |
| | 3. Comparison of the Three Protiated Systems | 57 |
| | D. REFERENCES..... | 59 |
| CHAPTER II | TRANSIENT ABSORPTION SPECTROSCOPY OF Mo AND W QUADRUPLY-BONDED DIMERS..... | 69 |
| | A. BACKGROUND..... | 69 |
| | B. EXPERIMENTAL METHODS..... | 79 |
| | C. RESULTS AND DISCUSSION..... | 81 |
| | 1. D_{2h} Complexes: $M_2Cl_4(\overline{P}P)_2$ | 81 |
| | 2. D_{2d} Complexes: $M_2Cl_4(PR_3)_4$ | 90 |
| | D. CONCLUDING REMARKS..... | 105 |
| | E. REFERENCES..... | 105 |

| | | |
|---------------|--|-----|
| CHAPTER III | THE DRIVING FORCE DEPENDENCE OF BI- | |
| | MOLECULAR PROTEIN ELECTRON TRANSFER: | |
| | *Ru(L) ₃ ²⁺ /CYTOCHROME <i>c</i> SYSTEM..... | 111 |
| | A. BACKGROUND..... | 111 |
| | B. EXPERIMENTAL METHODS..... | 114 |
| | C. THEORY..... | 120 |
| | D. RESULTS AND DISCUSSION..... | 122 |
| | E. REFERENCES..... | 136 |
| APPENDIX..... | | 141 |

LIST OF TABLES

| Table | | Page |
|--------------|--|-------------|
| I | Structures and Reduction Potentials (vs NHE) of the Acceptors 1 – 3 in their Protiated and Deuterated Forms | 17 |
| II | Observed ^1H NMR Shifts and FWHM of Carboxy Proton Resonances of CD_2Cl_2 Solutions of DNBCOOH and ZnPCOOH at Selected Concentrations of the Acid | 30 |
| III | Observed ^1H NMR Shifts and FWHM of Carboxy Proton Resonances of CD_2Cl_2 Solutions of DNBCOOH/ZnPCOOH at Selected Concentrations of the Acid Mixture | 30 |
| IV | Monomer and Dimer Vibrational Frequencies of DNBCOOH and ZnPCOOH in the OH and CO Stretching Regions | 30 |
| V | Calculated Self-Association Binding Constants for DNBCOOH and ZnPCOOH in CH_2Cl_2 at Room Temperature | 33 |
| VI | Concentration Dependence of the Charge Separation and Charge Recombination Rates of 1-H in CH_2Cl_2 | 40 |
| VII | Comparison of Charge Separation and Recombination ET Rates for the Three Acceptors with ZnPCOOH and their Respective Driving Forces | 57 |
| VIII | Ground State Electronic Absorption Maxima of Several Edge-Sharing Bioctahedral Complexes in the Visible Region | 87 |
| IX | Lifetimes and Emissive Quantum Yields of the $\delta\delta^*$ Excited State of $\text{Mo}_2\text{Cl}_4(\text{PR}_3)_4$ Complexes and Non-Emissive Transient Lifetimes | 91 |
| X | Cone Angles (ϕ) of PR_3 Ligands | 102 |

| | | |
|------|--|-----|
| XI | Emission Lifetimes and Excited State Redox Potentials of the Ru ^{II} Complexes Utilized in this Study | 123 |
| XII | Driving Force and Observed Rates for the ET Reactions between the MLCT Excited State of Ru ^{II} Complexes and Cytochrome <i>c</i> in the Oxidized (Fe ^{III}) and Reduced (Fe ^{II}) States | 123 |
| XIII | Driving Forces, Calculated Values of the Rates of Diffusion and Electronic Coupling, and Observed Bimolecular Electron Transfer Rates between Neutral and Negative Complexes and Fe ^{III} cytochrome <i>c</i> | 128 |
| XIV | Comparison of Reorganization Energy and Electronic Coupling in ET Reactions involving Cytochrome <i>c</i> | 131 |
| XV | Comparison of Electronic Coupling in ET Reactions of Organic and Inorganic Donor/Acceptor Systems | 132 |
| AI | IR Absorbances of DNBCOOH Utilized in the Self-Association Binding Constant Calculations Described in Chapter I | 141 |
| AII | IR Absorbances of ZnPCOOH Utilized in the Self-Association Binding Constant Calculations Described in Chapter I | 141 |
| AIII | IR Absorbances of ZnPCOOH and DNBCOOH Utilized in the Hetero-Association Binding Constant Calculation Described in Chapter I | 142 |

LIST OF FIGURES

| Figure | | Page |
|--------|---|------|
| 1 | Schematic representation of PSII showing the electron transfer pathway and rates | 11 |
| 2 | Pictorial representation of (a) cytochrome c oxidase in the inner mitochondrial membrane and (b) the reduction of oxygen at the bimetallic center | 13 |
| 3 | Schematic diagram of the picosecond laser system, pulsed dye amplification, and transient absorption spectrometer | 20 |
| 4 | ¹ H NMR spectra of CD ₂ Cl ₂ solutions containing DNBCOOH and ZnPCOOH where the concentration of each component is 4 × 10 ⁻⁴ M (top), 1 × 10 ⁻³ M (middle), and 3 × 10 ⁻³ M (bottom). The carboxy proton is denoted by (*) in all spectra | 31 |
| 5 | FTIR spectra in the CO stretching region of CH ₂ Cl ₂ solutions of (A) DNBCOOH, (b) ZnPCOOH, and (c) DNBCOOH and ZnPCOOH. The concentrations of each component for (a), (b), and (c) are 1.6 × 10 ⁻³ M (top), 1.0 × 10 ⁻³ M (middle), and 4.0 × 10 ⁻⁴ M (bottom) | 32 |
| 6 | Plot of the left side of eq 5 vs [DNBCOOH] | 35 |
| 7 | (a) Emission spectra and (b) luminescence decays of CH ₂ Cl ₂ solutions of ZnPCOOD in the absence (top trace) and presence (bottom trace) of 10 ⁻² M DNBCOOD | 36 |
| 8 | Transient absorption spectrum of a CH ₂ Cl ₂ solution of TCNE and ZnPCOOCH ₃ collected 1 μs after the laser pulse (10 ns, 532 nm) | 38 |
| 9 | Transient absorption spectra of ZnPCOOH collected 15 ps (—) and 1.5 ns (---) after the excitation pulse | 41 |

| | | |
|----|---|----|
| 10 | Transient absorption spectra of ZnPCOOD collected 15 ps (—) and 1.5 ns (---) after the excitation pulse | 42 |
| 11 | Transient (a) rise and (b) decay of the $^1\pi\pi^*$ excited state of a 10^{-3} M CH_2Cl_2 solution of ZnPCOOH in the 625 – 760 nm region | 43 |
| 12 | Transient absorption spectra at various delay times after the 580 nm, 3 ps excitation pulse of ZnPCOOH (1.4×10^{-3} M) and DNBCOOH (4×10^{-2} M) in CH_2Cl_2 | 44 |
| 13 | Transient (a) rise and (b) decay of a CH_2Cl_2 solution containing $[\text{ZnPCOOH}] = 1.6 \times 10^{-3}$ M and $[\text{DNBCOOH}] = 4.0 \times 10^{-2}$ M in the 625 – 760 nm region | 46 |
| 14 | Transient decay of the $^1\pi\pi^*$ excited state of a 10^{-3} M CH_2Cl_2 solution of ZnPCOOCH ₃ containing 5×10^{-2} M DNB-COOCH ₂ CH ₃ in the 625 – 760 nm region | 47 |
| 15 | Transient absorption spectra at selected delays following the pump pulse of CH_2Cl_2 solutions of $[\text{ZnPCOOH}] = 10^{-3}$ M and $[\text{DNTCOOH}] = 10^{-2}$ M, showing the decays (a) prior to and (b) after 300 ps | 49 |
| 16 | Plot of $-\ln(\Delta\text{OD})$ vs time showing the triphasic decay of the ZnPCOOH/DNTCOOH pair | 50 |
| 17 | Transient absorption spectra at selected delays following the pump pulse of CH_2Cl_2 solutions of $[\text{ZnPCOOH}] = 10^{-3}$ M and $[\text{DNTCOOH}] = 10^{-2}$ M, after subtraction of $^1\pi\pi^*$ signal | 52 |
| 18 | Transient absorption spectra collected at selected delay times after the pump pulse of CH_2Cl_2 solutions containing ZnPCOOH and AQCOOH, after subtraction of $^1\pi\pi^*$ signal .. | 54 |
| 19 | Plot of $-\ln(\Delta\text{OD})$ vs time showing the biphasic decay of the ZnPCOOH/AQCOOH pair | 55 |

| | | |
|----|---|----|
| 20 | Transient absorption spectra of a CH ₂ Cl ₂ solution containing [ZnPCOOD] = 10 ⁻³ M and [DNTCOOD] = 10 ⁻² M collected 20 ps (—) and 2 ns (---) after the excitation pulse | 56 |
| 21 | Molecular orbital diagram derived by uniting two d ⁴ ML ₄ fragments to form the bimetallic M ₂ L ₈ quadruply-bonded complex | 72 |
| 22 | Valence bond description of the electronic states formed by the d _{xy} orbitals, as well as the corresponding MO formalism .. | 74 |
| 23 | Qualitative MO diagram showing correlation between D _{2h} and D _{2d} geometries | 75 |
| 24 | Electronic absorption spectra of (—) Mo ₂ Cl ₄ (dppm) ₂ and (---) W ₂ Cl ₄ (dppm) ₂ in CH ₂ Cl ₂ | 76 |
| 25 | Electronic absorption spectra of (—) W ₂ Cl ₄ (PBU ₃) ₄ and (---) Mo ₂ Cl ₄ (PBU ₃) ₄ in CH ₂ Cl ₂ | 77 |
| 26 | Transient absorption spectra of Mo ₂ Cl ₄ (dmpm) ₂ in CH ₂ Cl ₂ collected 2, 20, and 50 ps following the 600 nm, 3 ps excitation pulse. The decay of the bleaching at 630 nm is shown in the inset | 82 |
| 27 | (a) Transient absorption spectrum of Mo ₂ Cl ₄ (dmpm) ₂ in CH ₂ Cl ₂ recorded 1 μs after 355 nm, 10 ns excitation and (b) electronic absorption spectrum of independently-prepared Mo ₂ Cl ₆ (dppm) ₂ | 84 |
| 28 | (a) Transient absorption spectra of W ₂ Cl ₄ (dppm) ₂ in benzene recorded 100 ns and 4 μs after 532 nm, 10 ns excitation. (b) Absorption spectra of W ₂ Cl ₆ (PEt ₃) ₄ (---) and W ₂ Cl ₆ (dppm) ₂ (—) in toluene and CH ₂ Cl ₂ , respectively | 85 |
| 29 | Proposed mechanism for the formation of the long-lived transient in D _{2h} complexes following high-energy excitation .. | 89 |

| | | |
|----|--|-----|
| 30 | Transient absorption spectrum of $\text{Mo}_2\text{Cl}_4(\text{PPh}_2)_4$ in CH_2Cl_2 collected 2 ps after the 600 nm, 3 ps, excitation. The inset shows the decay of the absorbance at 420 nm | 92 |
| 31 | Transient absorption spectrum of $\text{W}_2\text{Cl}_4(\text{PEt}_3)_4$ in toluene recorded 70 ns after the 683 nm excitation pulse; the inset shows the spectral profile in the near UV region | 93 |
| 32 | Transient absorption spectrum of $\text{W}_2\text{Cl}_4(\text{PBU}_3)_4$ in CH_2Cl_2 recorded 70 ns after the 683 nm excitation pulse; the inset shows the spectral profile in the near UV region | 94 |
| 33 | Transient absorption spectrum of $\text{W}_2\text{Cl}_4(\text{PPh}_2\text{Me})_4$ in THF recorded 70 ns after 683 nm, 10 ns excitation | 95 |
| 34 | Decays of (a) $\text{W}_2\text{Cl}_4(\text{PMe}_3)_4$ and (b) $\text{W}_2\text{Cl}_4(\text{PBU}_3)_4$ following 683 nm excitation; in both cases the top curve is that of the transient absorption signal at 500 nm and the bottom corresponds to the luminescence decay at 800 nm | 97 |
| 35 | Transient absorption spectra recorded 60 ns after 532 nm excitation of (a) $\text{Mo}_2\text{Cl}_4(\text{PBU}_3)_4$, (b) $\text{Mo}_2\text{Cl}_4(\text{PMe}_2\text{Ph})_4$, and (c) $\text{Mo}_2\text{Cl}_4(\text{PPh}_2\text{Me})_4$ in CH_2Cl_2 | 98 |
| 36 | Decays of $\text{W}_2\text{Cl}_4(\text{PPh}_2\text{Me})_4$ in CH_2Cl_2 followed at (Δ) 400 nm and (O) 440 nm after 532 nm, 10 ns excitation | 99 |
| 37 | Log-log plot of the emission quantum yield vs the $^1\delta\delta^*$ lifetime of complexes in the $\text{Mo}_2\text{Cl}_4(\text{PR}_3)_4$ series | 101 |
| 38 | Schematic representation of the ligands utilized in the driving force dependence study of the ET rate | 113 |
| 39 | Driving force dependence of the ET rate in (a) fixed-distance systems and (b) diffusion controlled reactions | 115 |
| 40 | Schematic representation of the normal ($-\Delta G < \lambda$), activationless ($-\Delta G = \lambda$), and inverted ($-\Delta G > \lambda$) regimes of electron transfer (see text) | 116 |

| | | |
|----|---|-----|
| 41 | Stern-Volmer plots of the quenching of 6×10^{-5} M solutions of $\text{Ru}(\text{diMe-phen})_3^{2+}$ in pH = 7, $\mu = 0.1$ M phosphate buffer by (a) <i>ferrocytochrome c</i> and (b) <i>ferricytochrome c</i> , showing the linear fit through the data points | 124 |
| 42 | Transient absorption spectrum obtained from a $\mu = 0.1$ M, pH = 7.4 phosphate buffer solution of 1×10^{-3} M $\text{Ru}(\text{diMe-phen})_3^{2+}$ and 1×10^{-3} M <i>ferricytochrome c</i> following 532 nm, 10 ns excitation | 125 |
| 43 | Plots of the electron transfer rates of Ru^{II} complexes with (a) Fe^{III} cytochrome <i>c</i> and (b) Fe^{II} cytochrome <i>c</i> , with their respective calculated k_{obs} (solid curve), k_{act} (dashed curve), and diffusion rates | 126 |
| 44 | Stern-Volmer plots of $\text{Ru}(\text{bps})_3^{4-}$ (O), $\text{Ru}(\text{phen})_2(\text{bps})$ (Δ), and $\text{Ru}(\text{phen})_2(\text{CN})_2$ (\square) | 129 |
| 45 | Schematic diagram of cytochrome <i>c</i> viewed from the (a) top and (b) front. The dashed lines indicate regions I, II, and III, with some approximate residue numbers, where proteins, small anions, and cations react with the protein, respectively .. | 131 |
| 46 | Plot of the data points from ref. 52, showing the calculated rates, k_{obs} (solid curve) and k_{act} (dashed curve). The diffusion limit, k_{diff} , is shown at $7.1 \times 10^8 \text{ M}^{-1}\text{s}^{-1}$ | 135 |

INTRODUCTION

The mechanisms of electron transfer reactions have been in question since the earliest studies of ions in solution. The seminal work of Taube in the 1950s led to the distinction between inner- and outer-sphere electron transfer pathways.¹⁻³ Inner sphere refers to those inorganic reactions where an atom is shared between the reagents in the precursor complex prior to electron transfer, and in most instances the bridging ligand is transferred from the electron acceptor to the donor. In outer-sphere electron transfer the reactants diffuse together and an electron is transferred without net bond changes. Parallel reactions are observed in organic chemistry, although the distinction between the two mechanisms is not as evident and has only recently been emphasized.^{4,5}

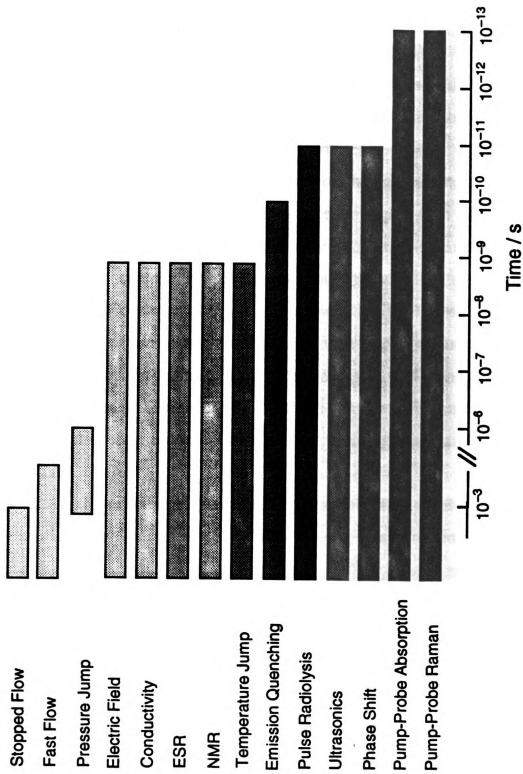
The transfer of one electron is commonly observed throughout organic and inorganic chemistry. In addition to the discrete transfer of an electron from a donor to an acceptor and the formation of charge transfer complexes, many other reactions fall into this category. These include organic radical reactions, group transfers, and heterolytic bond cleavage. In inorganic chemistry, one-electron reactions are those in which the valence of the metal changes by one, as observed in the common addition or elimination of charged ligands. These may be exemplified by halides, cyanide, *carboxylates*, or alkyl oxides.

Another class of electron transfer is the movement of more than one electron during the course of a reaction. Many inorganic reactions proceed with a net two-electron change, such as oxidative-addition and reductive-elimination of X_2 ($X = \text{halide}$), H_2 , and HX , among others.⁶ Similar behavior is observed in organic reactions, with the transfer of hydride, oxygen atom, or halonium ion (X^+). Moreover, typical organic mechanisms propose the movement of many electrons, often in pairs. To distinguish between a concerted transfer of more than one electron and a path composed of several consecutive one-electron steps one must directly observe the intermediates, unless the one-electron reaction is sufficiently slow to afford the observation of products from radical traps. A benchmark example, where a once-thought concerted two-electron transfer was shown to proceed via two consecutive one-electron steps is the Pt^{II}/Pt^{IV} reaction.⁷

The dynamic detection of the one-electron intermediates is difficult in fast reactions. The methods available in the past to determine the rates of formation of intermediates and their identity have included stopped flow, jump methods, electrochemical techniques, and low-temperature spectroscopy. However, with the advent of pulsed lasers and fast electronics it has been possible in the last twenty years to directly measure reaction rates faster than 10^{10} s^{-1} . Some of these methods along with their corresponding range of detection times are shown in Scheme I.⁸ The techniques listed in Scheme I have been previously described in detail and will, therefore, not be discussed here.

It is apparent from Scheme I that optical techniques have surpassed the others in accessing very fast reactions. These advances have rested primarily on the duration of laser pulses, which have become increasingly

Scheme I



shorter, now reaching a few femtoseconds. Since only reaction times longer than the duration of the excitation pulse can be measured, the laser pulse width is a critical parameter. A laser pulse can be utilized to initiate a reaction, and detection techniques, including electronic absorption, Raman, time-resolved emission, or infrared absorption can be used to follow the decay and determine the identity of the intermediates.

These techniques permit measurement of the fastest rates; thus the upper limit of the rates of photoinduced reactions is higher than those found in other methods. Donor/acceptor studies which feature the transfer of one electron from an electronically excited state have taken advantage of these fast techniques. However, these systems usually involve simple one-electron transfer, and are often within the confines of outer-sphere electron transfer.⁹ A detailed description of the work in this area is presented in the Background section of Chapter I. Many atom-transfer reactions in organic systems have also been probed in this manner, although they are generally one-electron in nature.¹⁰

Fast laser techniques, however, can be utilized to elucidate the fundamental mechanistic questions of more diverse reactivity, in addition to simple one-electron outer-sphere electron transfer, if such reactions are photochemically designed. This is the emphasis of the work described herein. Three different electron transfer reaction mechanisms have been elucidated in this thesis. These included 1) the role of hydrogen bonds in the electron transfer pathway on the picosecond time scale (Chapter I); 2) the nature of excited intermediates formed upon light absorption in bimetallic complexes, that are known to lead to two-electron oxidative addition reactions in the presence of substrates (Chapter II); and 3) the photoinitiated bimolecular electron transfer rates at very high driving forces (Chapter III).

Photoinduced electron transfer is predicated on the production of an electronic excited state upon light absorption which is either strongly oxidizing or reducing in nature, and it can therefore undergo facile electron transfer with donors and acceptors. Hydrogen bonds are believed to play an important role in the mediation of long-range electron transfer in biological systems.^{11,12} The effect of hydrogen bonds on the electron transfer pathway has been determined in model systems by monitoring the rates of charge separation and charge recombination in protiated and deuterated systems. In these particular systems an electron is transferred from a Zn-substituted porphyrin, placed in its $^1\pi\pi^*$ excited state by excitation with a laser pulse, to several acceptors. In these systems the donor and acceptor are hydrogen-bonded by a carboxylic acid interface. The results of this study are presented in Chapter I.

The photoexcitation of the reactants is particularly interesting in systems which are known to undergo two-electron oxidative addition when excited with light, such as the Mo and W quadruply-bonded dimers.¹³ It is of interest to follow the mechanism of such transformations, since radical reactions are not observed outside the solvent cage. A concerted two-electron process in this system would implicate a three-atom transition state, whereas two sequential one-electron transformations would afford a two-atom transition state with the concomitant formation of radicals. The initial studies of these systems are presented in Chapter II, where the excited states and reactive intermediates observed in inert solvents are discussed.

The photoinitiated electron transfer rates for the bimolecular reactions between Ru complexes and oxidized or reduced cytochrome *c* have been determined from emission lifetime quenching measurements. An investigation of the driving force dependence of the electron transfer rate

was conducted, and a decrease of the rates in the highly exergonic systems was observed. These results, discussed in Chapter III, are particularly interesting, since inverted region electron transfer has only rarely been observed for bimolecular donor/acceptor pairs.

References

1. Seaborg, G. T. *Chem. Rev.* **1940**, *27*, 199.
2. Symposium on Electron Transfer Processes *J. Phys. Chem.* **1952**, *56*, 801-910.
3. Taube, H. *Electron Transfer Reactions of Complex Ions in Solution*; Academic Press: New York; 1970.
4. Pross, A. *Acc. Chem. Res.* **1985**, *18*, 212.
5. Ebersson, L. *Electron Transfer Reactions in Organic Chemistry*; Springer-Verlag: Berlin; 1987.
6. Jordan, R. B. *Reaction Mechanisms of Inorganic and Organometallic Systems*; Oxford University Press: New York, 1991.
7. Taube, H. In *Mechanistic Aspects of Inorganic Reactions*; Rorabacher, D. B.; Endicott, J. F., Eds.; ACS Symposium Series, vol 198; American Chemical Society: Washington, DC, 1982; p 151.
8. Jonah, C. D. In *Chemical Reactivity in Liquids Fundamental Aspects*; Plenum: New York, 1988; pp 1 – 14 and references therein.
9. For recent reviews on photoinduced electron transfer see *Chem. Rev.* **1992**, *92*, 365-490.
10. Baltrop, J. A.; Coyle, J. D. *Excited States in Organic Chemistry*; John Wiley: Bristol, 1975.

11. Williams, R. J. P. In *Electron Transfer in Biology and the Solid State*; Johnson, M. K.; King, R. B.; Kutz, D. M., Jr.; Kotal, C.; Norton, M. L.; Scott, R. A., Eds.; Advances in Chemistry Series 226; American Chemical Society: Washington DC; 1990, pp 3-26.
12. *Topics in Photosynthesis: The Photosystems*; Barber, J., Ed.; Elsevier: Amsterdam, 1991.
13. Partigianoni, C. Ph.D. Dissertation, Michigan State University, 1991.

CHAPTER I

ELECTRON TRANSFER THROUGH HYDROGEN BONDED INTERFACES

A. BACKGROUND

Proton associated electron transfer reactions are crucial in vital **biological** processes, especially those involving energy storage and **conversion**.^{1,2} Protons play both active and passive roles in electron transfer **events**. The most recognized form of coupling between electrons and **protons** is an active one, where a substrate is protonated or deprotonated **upon** its reduction or oxidation. This behavior leads in some instances to the **vectorial** movement of protons across a membrane, which is typically **concomitant** with the movement of electrons in the opposite direction.^{1,2} Another manner in which protons are moved across a membrane is by the **action** of proton pumps, which are often encountered in biological **transmembrane** assemblies, such as ATP synthase, Na⁺/K⁺ ATPases, Ca²⁺ **ATPases**, and bacteriorhodopsin.³ The pumping mode of action is believed to **involve** changes in protonation of residues of the helical protein structures **that** comprise the enzyme, resulting in some backbone distortions. This **protein** motion is in turn governed by the redox state of the active centers or

the conformation of a chromophore.⁴⁻¹⁰ The passive role of protons in modulating electron transfer rates has only recently been investigated in detail. This type of modulation is believed to take place by the transfer of an electron through one or several hydrogen bonds in long-range electron transfer in proteins. The experimental and theoretical investigations have been limited to small proteins such as cytochrome *c*, cytochrome *b₅*, plastocyanin, and azurin, where it is believed that hydrogen bonds within the protein provide better coupling for electron transfer than longer covalently-bound pathways.¹¹⁻¹³

The movement of protons coupled to electron transfer can take the form of directed but opposite motion of protons and electrons across a membrane. This establishes an electrochemical proton gradient, which is transformed into chemical energy by the production of high energy molecules such as ATP (adenosine triphosphate) from ADP (adenosine diphosphate) and inorganic phosphate by the enzyme ATP synthase, and NADPH from the reduction of NADP⁺ (nicotinamide adenine dinucleotide phosphate) by protonation of the nicotinamide ring. The energy stored in these molecules is then utilized to perform life-sustaining functions in the cell such as the reduction CO₂ to carbohydrates in the dark reactions of photosynthesis and the breakdown of carbohydrates, fats, and sugars following respiration.

Active proton/electron coupling is evident in many systems such as in oxidases and in the photosynthetic cycles. Protonation is concomitant with electron transfer within xanthine oxidase, an enzyme which catalyzes the xanthine hydroxylation to uric acid and dioxygen reduction to peroxide or superoxide.¹⁴ Another example of proton movement coupled to electron transfer events is found in sarcosine oxidase, where the oxidative

der

by

pro

rea

thy

pro

han

a cl

the

acc

and

sp

st

Ra

bel

mas

Ed

P,

ed

ac

ed

pro

in

de

Q

demethylation of sarcosine is accompanied by the reduction of O_2 to hydrogen peroxide.¹⁵ Yet, the most intensively investigated example of proton movement coupled to electron transfer is that of the photosynthetic reaction center and cytochrome *c* oxidase.

Photosystems I and II (PSI and PSII, respectively), lie across the thylakoid membrane and effect a transverse flux of electrons and protons.^{16,17} Their action is predicated on the absorption of photons by light harvesters, which through energy transfer populate the $^1\pi\pi^*$ excited state of a chlorophyll dimer, the special pair (SP). Electron transfer from the excited chromophore to a nearby acceptor is followed by subsequent transfers to acceptors located at increasingly longer distances from the oxidized SP, thus avoiding electron/hole charge recombination.^{16,17} Figure 1 depicts the spatial arrangement of the molecules in PSII, as determined from the crystal structure of the reaction centers of *Rhodospseudomonas viridis* and *Rhodobacter sphaeroides* (the RC's in these photosynthetic bacteria are believed to be very similar to PSII in green plants).^{18,19}

The photophysics of PSII have been extensively investigated, and the rates for the primary electron transfer events are summarized in Figure 1. Following these primary electron transfer events from the SP to pheophytin (P_A), the two quinones, Q_A and Q_B , are reduced in series.²⁰⁻²⁵ The SP cation radical returns to its neutral state by the oxidation of water to O_2 via the action of the oxygen-evolving center (OEC), after four sequential electron transfer events. It has been proposed that the oxidation of water at the OEC proceeds by a series of proton-coupled electron transfer reactions of an oxo-bridged cluster of manganese.²⁶⁻²⁸ On the reduction side of the scheme, absorption of two consecutive photons leads to the two-electron reduction of Q_B , concomitant with the proton uptake from nearby ionizable residues to

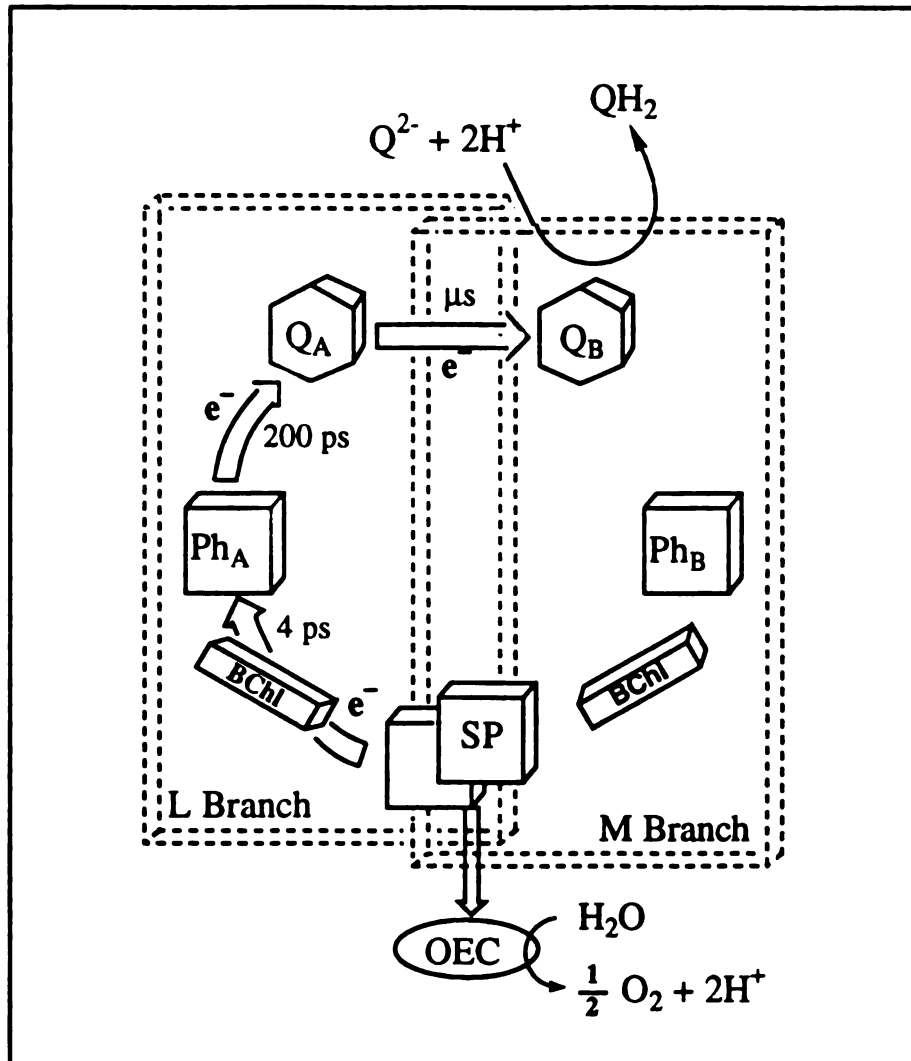


Figure 1. Schematic representation of PSII showing the electron transfer pathway and rates.

produce $Q_B H_2$.²⁹⁻³² The proton sources are believed to be glutamic and aspartic acids of the L subunit which are located near Q_B , although a serine residue may also play an important role in the protonation.²⁹⁻³² It has also been shown that hydrogen bonding to the carbonyl functionalities of both Q_A and Q_B facilitates the electron transfer events to the quinones.³³ Once protonated, $Q_B H_2$ exchanges with a quinone from the quinone pool; this process ultimately leads to the translocation of protons across the membrane thus creating a proton gradient.

The reduction of O_2 to water during respiration can be thought of as the reverse of the photosynthetic oxidation of water by the OEC in photosynthesis. As is the case in the OEC, proton movement is coupled to electron transfer in the enzyme cytochrome *c* oxidase. Reduction of the enzyme by four electrons is accomplished by the sequential electrostatic binding of the reduced protein, *ferrocytochrome c*, which is the last carrier in the electron transport chain.³⁴⁻³⁸ A schematic representation of cytochrome *c* oxidase is shown in Figure 2a, depicting its four redox-active metal centers: heme *a*, heme a_3 , Cu_A , and Cu_B .³⁴⁻³⁸ The primary electron acceptor within the enzyme is either heme *a* or Cu_A ,^{39,40} which are located in the cytoplasmic side of the inner mitochondrial membrane, closest to the cytochrome *c* binding site (Figure 2a). It is believed that the sequence of electron transfer events is initially cytochrome *c* \rightarrow Cu_A followed by $Cu_A \rightarrow$ heme *a* and heme *a* \rightarrow heme a_3/Cu_B .⁴¹⁻⁴⁵ Whereas no pH dependence of the electron transfer rates is observed in the absence of O_2 , in its presence some of the rate constants are affected by the medium's proton concentration, indicating the role of oxygen reduction on the proton pump activity of cytochrome *c* oxidase.^{42,46} The reduction of O_2 takes place at the heme a_3/Cu_B site, where it binds and becomes successively protonated as its

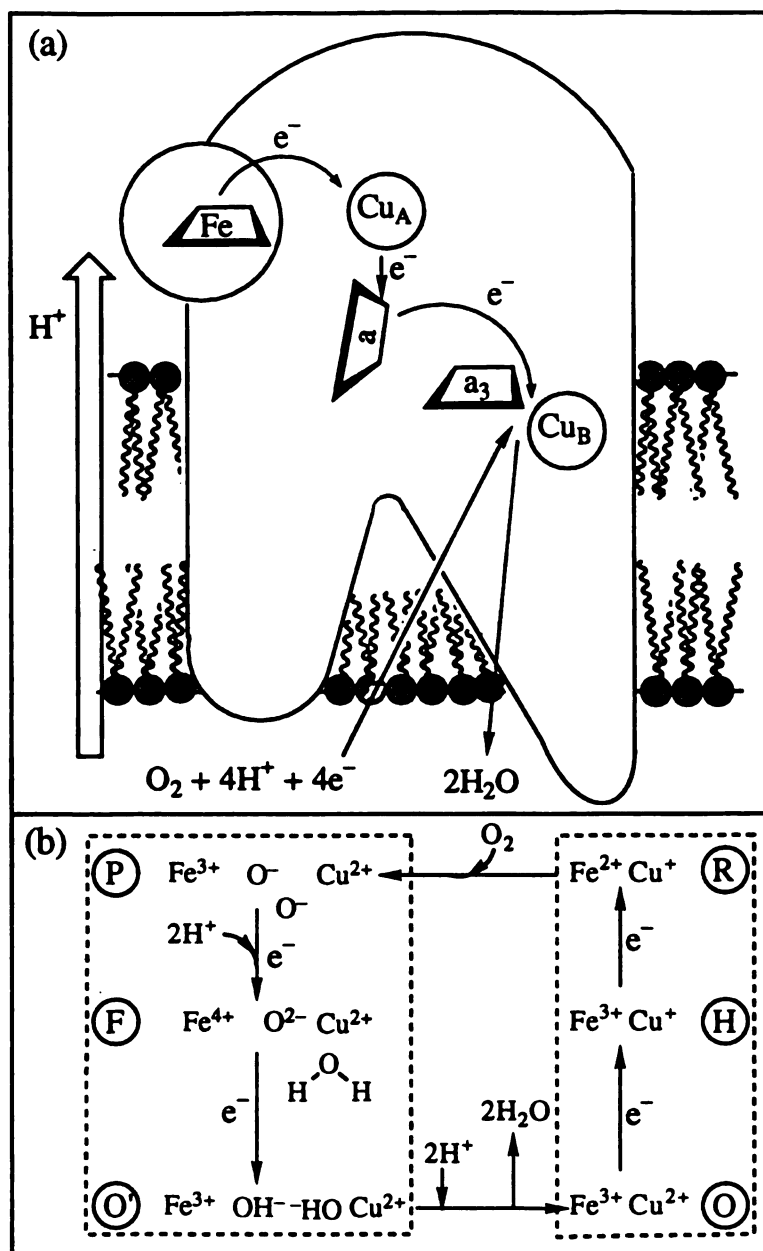


Figure 2. Pictorial representation of (a) cytochrome c oxidase in the inner mitochondrial membrane and (b) the reduction of oxygen at the bimetallic center.

stepwise multielectron reduction is effected.⁴⁶⁻⁴⁹ The mechanism of oxygen reduction proposed by Wikström is shown in Figure 2b, where the interplay between electron transfer and proton uptake can readily be observed.^{46,47} As shown in Figure 2b, a $2\text{H}^+/\text{e}^-$ stoichiometry is necessary to effect the transitions from peroxy (P) to ferryl (F) intermediates and from F to the fully oxidized (O) heme a_3/Cu_B center, where the latter is free of bound O_2 . The protons involved in O_2 reduction are taken up from the matrix side of the inner mitochondrial membrane, thus producing a proton gradient. The number of protons translocated per electron transfer, however, is twice that generated from oxygen reduction alone.³⁴⁻³⁸ The remaining protons are believed to be translocated through the action of a transmembrane proton pump, as described above, although the exact mechanism of action is not yet fully understood.⁴²⁻⁴⁵

Unlike the long standing recognition of proton transfer in protein electron transfer events, the passive role of protons has only recently been recognized. A limited amount of experimental evidence^{12,13} is now available to support the semi-empirical calculations performed on small proteins,¹¹ which predict that the magnitude of the electronic coupling is dictated by the type of pathway between the donor and acceptor in addition to their separation.¹³ The most striking evidence was obtained for Ru-modified cytochrome *c*, where the excited state electron donor $\text{Ru}(\text{bpy})_2(\text{im})(\text{His}^X)^{2+}$ (bpy = 2,2'-bipyridine, im = imidazole, His^X = histidine at position X) is coordinated to several different histidines of the protein.¹² The electron transfer rates from the excited state covalently-bound Ru complex to the protein's heme can be determined, and they can then be correlated to the distance between the modified histidine and the heme and to possible electron tunneling pathways. The different pathways

in

co

co

he

to

fav

Ca

con

de

ran

re.

ran

ran

ran

ran

ran

ix

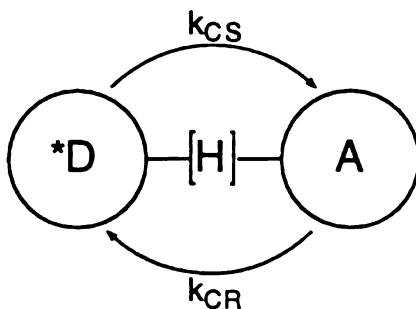
ran

ran

ran

include those which are completely covalently bound and those which contain hydrogen bonds or through-space jumps in conjunction with covalent bonds. Although the electron can take any pathway to reach the heme, only the most favorable ones are expected to contribute significantly to the rate. It was found that pathways containing hydrogen bonds are favored over much longer ones containing only covalent bonds.¹⁴ Calculations were performed which predict that one hydrogen bond corresponds to three covalent linkages, whereas one through-space jump can be correlated to ten covalently bonded atoms.¹³

The passive role of protons on the modulation of electron transfer rates has not been subjected to the rigorous experimental and theoretical treatment that has advanced the knowledge of fixed distance electron transfer in inorganic and organic compounds,⁵⁰⁻⁶² proteins,⁶³⁻⁷⁰ and enzymes.²⁶ Of the active and passive proton involvement in electron transfer rates, we have begun model studies on the latter because it is synthetically more tractable. One approach to assessing the passive role of protons in electron transfer rates is to combine the strategy of photoinduced fixed-distance electron transfer⁴¹⁻⁶¹ with that of photoinduced proton transfer.⁷¹⁻⁷³ The strategy chosen here is to channel the electron as it travels from the photoexcited donor (*D) to an acceptor (A) through a proton interface, as is schematically depicted below



wl

re

sh

by

bo

sy

wh

Za

sta

vs

var

dir

sho

hos

the

pot

fin

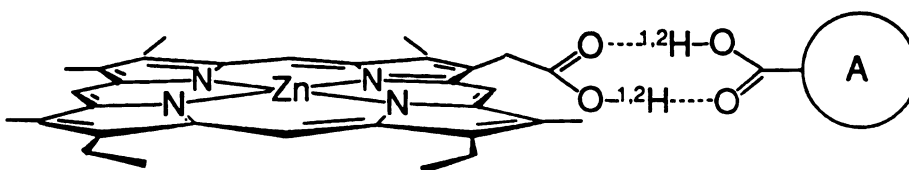
The

and

4-po

where k_{CS} and k_{CR} are the rate constants for charge separation and charge recombination, respectively. Careful design of the donor/acceptor system should preclude the electron from travelling through pathways other than the hydrogen-bonded interface.

The propensity of carboxylic acids to dimerize in non-hydrogen bonding solvents of low polarity⁷⁴⁻⁷⁶ allows us to prepare donor/acceptor systems such as

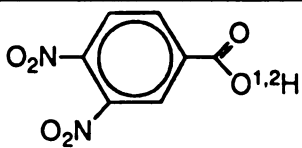
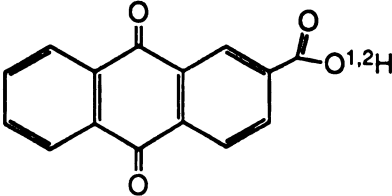
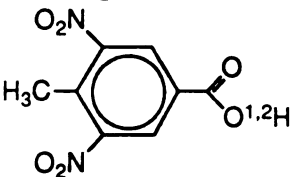


where the photoexcitable donor is a Zn-substituted porphyrin in the protiated ($ZnPCOOH$) or deuterated form ($ZnPCOOD$). The $ZnPCOOH$ $^1\pi\pi^*$ excited state ($E_{0,0} = 2.1$ eV) is a powerful reducing agent, with $E(ZnP^{+/*}) = -1.3$ V vs NHE (since $E_{1/2}(ZnP^{+/0}) = 0.80$ V vs NHE),⁷⁷ such that it can reduce a variety of acceptors including several substituted nitrobenzenes and dinitrobenzenes. The structures of the acceptors utilized in this study are shown in Table I, in addition to their respective reduction potentials.

The reduction potentials of the acceptors presented in Table I are those of their decarboxylated forms. The addition of the $-COOH$ group to the 2-position of 9,10-anthraquinone is known to make the reduction potential more positive by 0.06 V,⁷⁸ whereas the reduction potential of 3,4-dinitrobenzoic acid only differs by 0.02 V from that of 3,4-dinitrobenzene.⁷⁹ These potential changes, however, were determined by different methods, and therefore may not be comparable. The addition of a methyl group at the 4-position in methyl-3,5-dinitrobenzoate, to form the methyl ester of 3,5-

dinitro-*p*-toluic acid, increases the value of the reduction potential by 0.1 V.⁸⁰ Therefore, we chose the reduction potential of 3,5-dinitrotoluic acid to be 0.1 V larger than that of 3,5-dinitrobenzoic acid. Although the reduction potentials of the acids have been measured, the values obtained by different methods are not in good agreement. We have therefore chosen to utilize the values of the decarboxylated compounds, since the reported values are in better agreement.⁸¹

Table I. Structures and Reduction Potentials (vs NHE) of the Acceptors 1 – 3 in their Protiated and Deuterated Forms.

| D/A Systems | Structure | $E_{1/2}(A^{-/0}) / V^a$ |
|-------------|---|--------------------------|
| 1-H and 1-D |  | -0.6 |
| 2-H and 2-D |  | -0.6 |
| 3-H and 3-D |  | -0.8 |

^aValues from Ref. 81.

The rates of charge separation (k_{CS}) and charge recombination (k_{CR}) have been measured in these hydrogen-bonded donor/acceptor pairs using picosecond transient absorption spectroscopy. The effect on the electron transfer rate of deuterium substitution of the carboxy groups of each reactant has been determined by comparison to the protiated analogs.

B. EXPERIMENTAL METHODS

All the acid acceptors, 3,4-dinitrobenzoic acid, 3,5-dinitrobenzoic acid, *p*-nitrobenzoic acid, 2,6-dinitro-*p*-toluic acid, and 9,10-anthraquinone-2-carboxylic acid, as well as their methyl or ethyl esters were purchased from Aldrich. The porphyrin carboxylic acid was obtained from Professor C. K. Chang of the MSU Chemistry Department in the methyl ester form,⁸² and was subsequently treated with 18 M hydrochloric acid (~ 1 ml) in 88% formic acid (~ 10 ml) to obtain the protonated product. Following the removal of solvent with a rotovap, the product was refluxed in dimethylformamide (DMF) with excess $ZnCl_2$ to yield the metallated Porphyrin, $ZnPCOOH$. Deuteration of the porphyrin was performed just prior to metallation; it was accomplished by raising the pD of a D_2O solution to ~ 13 with NaOMe to remove the carboxy proton, followed by addition of D_3PO_4 until a pD of ~ 4 was reached. Deuteration of all the acceptors was also performed in this manner, followed by filtration of the solid. The IR spectra of all deuterated products exhibited a new feature at ~ 2600 cm^{-1} corresponding to the O-D stretch, and lacked the $\nu(OH)$ peak in the 3580 cm^{-1} region.

prep

typi

adja

built

the

belo

tran

sub

pou

spe

for

2 m

subl

dry

and

heat

spe

diab

in a

obta

and

with

laser

The samples to be used in transient absorption experiments were prepared by placing the desired amounts of donor and acceptor solids, typically 0.5 to 9 mg, in a 2 mm pathlength quartz cell equipped with an adjacent bulb. This apparatus has two high vacuum stopcocks, one on the bulb side to seal it from the atmosphere and another between the bulb and the cell. Following evacuation of the cell containing the solid to pressures below 3×10^{-5} torr, dichloromethane, previously dried over 4 Å sieves, was transferred from a storage container to the bulb under vacuum and was subsequently freeze-pump-thawed at least three times. The solvent was poured from the bulb to the cell to attain the desired concentration.

The binding constant studies were performed with a Nicolet-145 FTIR spectrometer, and typically 50 averages at 1 cm^{-1} resolution were collected for each acquisition. The samples utilized in these studies were placed in the 2 mm pathlength, CaF_2 IR cell in a dry box. The solids were either dried or sublimed under vacuum ($\sim 5 \times 10^{-6}$ torr) prior to their introduction into the dry box. The solvent, CH_2Cl_2 , was purchased from Burdick and Jackson and was placed over 4 Å sieves that had been previously been dried by heating under vacuum ($\sim 2 \times 10^{-6}$ torr).

The NMR studies were performed in a Varian Gemini 300 MHz spectrometer. The samples were prepared with 0.5 ml ampules of d_2 -dichloromethane, which were opened just prior to placement of the solvent in a closed NMR tube and subsequent data collection.

The transient absorption signals in the picosecond time regime were obtained using the pump-probe technique. A schematic diagram of the laser and detection systems utilized to date is shown in Figure 3, where transients with lifetimes ranging from ~ 20 ps to ~ 3 ns can be monitored. The master laser in the setup is a Coherent Antares 76-s mode-locked Nd:YAG, whose

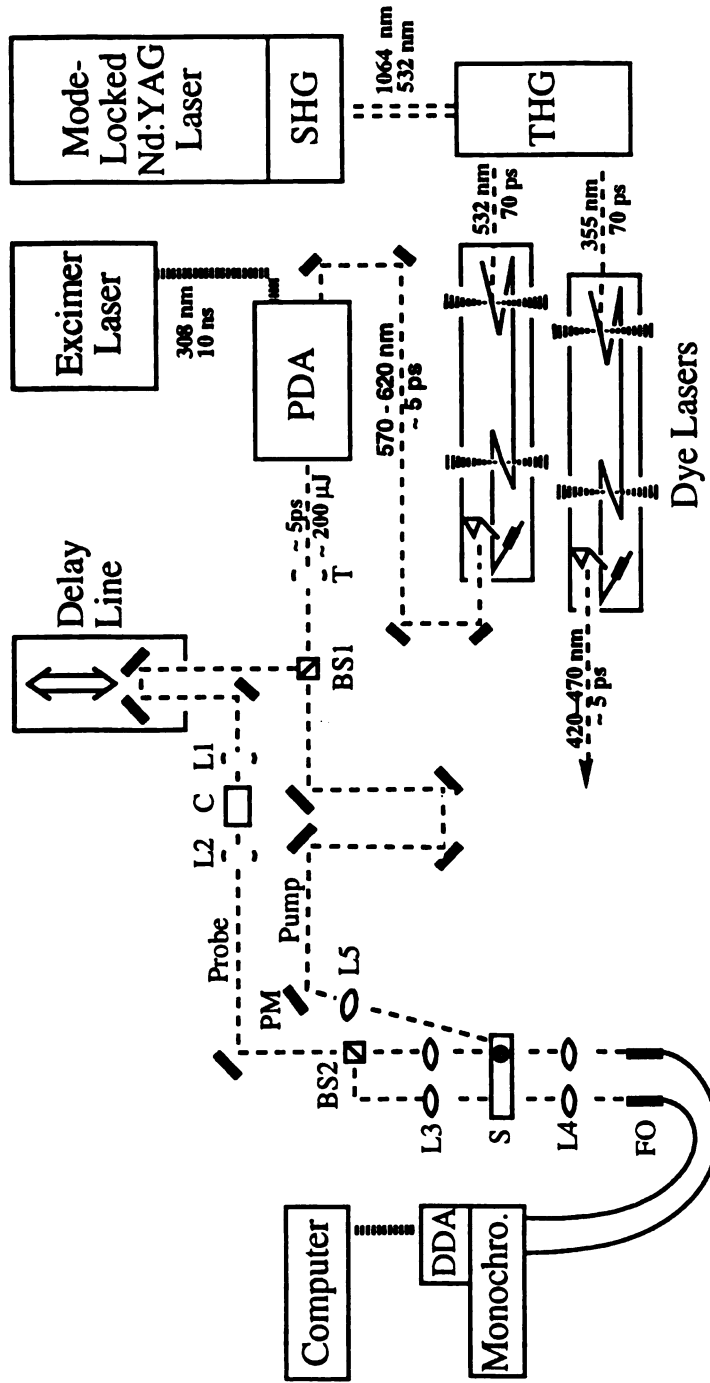


Figure 3. Schematic diagram of the picosecond laser system, pulsed dye amplification, and transient absorption spectrometer.

1064 nm output (FWHM = 70 ps, rep. rate = 76 MHz, $E_p = 400$ nJ/pulse) is frequency doubled with a heated KTP crystal ($\lambda_{out} = 532$ nm, $E_p = 40$ nJ/pulse) and tripled ($\lambda_{out} = 354.7$ nm, $E_p = 13$ nJ/pulse) with a Coherent 7950 THG assembly. The pulse width of the mode-locked IR output is continuously monitored with an Antel Optronics photodiode whose output is viewed on a Tektronix 7904A oscilloscope equipped with sampling and sampling sweep units (Tektronix models 7S11 and 7T11A, respectively). The doubled and tripled outputs provide the excitation for two synchronously-pumped cavity dumped dye lasers (Coherent 702 with model 7950 cavity dumpers) containing Rhodamine 590 ($\lambda_{out} = 570 - 620$ nm, $E_p = 26$ nJ/pulse at 7.6 MHz) and Coumarin 435 ($\lambda_{out} = 420 - 470$ nm, $E_p = 13$ nJ/pulse at 7.6 MHz) as their lasing media, respectively. The 5 ps (FWHM) pulse widths of the two synchronously-pumped dye lasers are monitored with two Inrad Model 5-14 autocorrelators, whose doubled output is viewed on two Tektronix 2225 oscilloscopes.

The low pulse energy output of the synchronously-pumped red dye laser is amplified by a four-stage pulsed dye amplifier (Lamba-Physik FL2003 PDA), pumped by a Lamba-Physik (model EMG 102 MSC) XeCl excimer laser ($\lambda_{out} = 308$ nm, FWHM = 10 ns). The output energies with Rhodamine 590 are ~200 - 400 mJ/pulse at repetition rates of 50 Hz. Amplification of blue pulses is performed with a home-built four-stage PDA, whose output energies are comparable to those in the red when pumped by the XeCl excimer. The excimer laser is externally triggered by an electronic device (Lamba-Physik FL2013) that converts the cavity-dumper's high repetition rate output to trigger pulses at 1 to 100 Hz repetition rates. The FL 2013 utilizes the attenuated SYNC OUT of the cavity dumper as its input, and its circuitry has been slightly modified in-

house.⁸³ The temporal drift of the excimer's thyatron firing with respect to the FL2013 trigger pulses is stabilized by the Lambda-Physik EMG97, which compares the time difference between the trigger pulse and the time the light pulse arrives at a photodiode placed in the 308 nm beam; its electronics collect this information for several shots and attempt to compensate for the drift by introducing a small time delay. When the excimer pump pulses and those from the synchronously-pumped dye laser are overlapped in space and time amplification takes place, since the emission of those dye molecules placed in the excited state by the pump are stimulated by the seed pulses.

Following collimation by a telescope (T), the amplified pulses are split ~ 50/50 by a cube beamsplitter (BS1) to produce pump and probe beams, as shown in Figure 3. The probe beam passes through a digital delay line (Klinger CC1.1), whose motor has step sizes corresponding to a 67 fs time delay and a total travel of ~ 6 ns. These pulses are then focused by a 1 in f/10 lens (L1) into a saturated aqueous solution of ZnCl₂, contained in a 10 cm pathlength cell with quartz windows. This medium is a good source of white light continuum radiation, resulting from the nonlinear refractive index effects caused by the large electric fields of the amplified short light pulses.⁸⁴ The continuum is collected and collimated by a 2 in lens (L2), and the seed pulse is separated from either red or blue light by introducing dielectric filters in the beam (not shown), which respectively transmit only above 600 nm and below 560 nm. The white light is then split by a second cube beamsplitter (BS2), and each of these probe beams is focused onto vertically displaced volumes of a sample cell (S) by two 1 in f/7 achromatic lenses (L3). The two white light beams are then focused by two 1 in f/4 lenses (L4) onto two fiber optics (FO), which are attached to the ISA HR320

single monochromator (300 gr/mm; $\lambda_{\text{blaze}} = 500 \text{ nm}$) by a Princeton Instruments fiber optic attachment. The inputs from the fiber optics remain spatially separated within the monochromator, and each is focused onto one of the two sets of 512 pixels which compose the dual diode array (Princeton Instruments DDA-512).

The pump beam is manipulated by means of several mirrors to match the distance traveled by the probe pulses when the delay line is positioned closest to the sample. This case is referred to as zero-time, where both probe and pump pulses arrive at the sample simultaneously. The pump beam is focused onto the sample by a 1 in f/10 lens (L5) such that it spatially overlaps with the bottom probe beam within the sample cell in a nearly-collinear manner (angle of incidence $\sim 13^\circ$). Temporal overlap of the pump and probe pulses leads to transient signals, absorption or bleaching, arising from the photogenerated species or from the disappearance of molecules in their initial state, respectively. Whereas signal is observed when the pump pulses are positioned to arrive at the sample before those of the probe, no signal is present when the probe pulses precede those of the pump.

The optical density, OD, or absorbance at a given wavelength is a function of the transmitted light given by⁸⁵

$$\text{OD} = -\log(I/I_0) \quad (2)$$

where I is the intensity of light through the sample and I_0 is the reference intensity when no sample is present. In a transient absorption experiment one measures the difference in absorbance (ΔOD) of the sample in the presence and absence of the excitation pulse; thus I and I_0 represent the probe light intensity passing through the two separate sample volumes with (bottom) and without (top) the pump, respectively. However, the cube

beamsplitter (BS2) is not exactly 50/50 (reflectance/transmittance), and therefore inherent differences in the light intensities passing through the two sample volumes are corrected by multiplication of I/I_0 in eq 2 by the ratio of the light intensities collected when no pump radiation is allowed to reach the sample, (I_t/I_b) . Each light intensity measurement is corrected by subtracting the dark background of each diode array (B_t and B_b) collected with no light present. Therefore six measurements are necessary to correctly calculate ΔOD at a given time delay and spectral window, collected with the same number of array scans and exposure time (typically 400 scans, 0.33 sec). The corrected ΔOD can be expressed by⁸⁶

$$\Delta OD = -\log \left\{ \frac{(I - B_b)}{(I_0 - B_t)} \frac{(I_t - B_t)}{(I_b - B_b)} \right\} \quad (3)$$

The ΔOD calculation is performed by a computer program at several pump/probe time delays, achieved by moving the delay line mirrors a selected number of steps, which determine the time the probe is delayed with respect to the static pump (0.067 ps/step). In this manner the rise and decay of transients can be mapped in time at a given spectral window. Each window covers approximately 130 nm, and the same procedure can then be followed to collect the time dependence of the absorbance at a different spectral window by moving the monochromator grating. Each spectral window was calibrated by allowing the atomic emission of Zn and Hg hollow cathode lamps to pass through the fiber optics and reach the detector. The positions of peaks from the hollow cathode lamps were experimentally determined using a scanning emission spectrometer equipped with a 1200 gr/mm grating.⁸⁷

The general alignment and experimental procedures utilized during the setup and data acquisition in a typical picosecond transient absorption experiment will be described assuming that 575 – 620 nm, 100 – 300 mJ (FWHM ~ 5 ps) pulses are obtained after PDA alignment. The beam exiting the PDA should have the best possible spatial profile to provide best continuum generation, although output energy may have to be sacrificed for beam quality. The spherical beam should not be larger than 4 mm in diameter after collimation by the telescope (T). The position of the beam exiting the PDA can be manipulated with the last two optics in the PDA (a polarizing beam splitter and a mirror), and should in this manner be aligned with several irises that have been setup before and after the delay line, as well as near the sample. The delay line should be positioned such that the beam travels the shortest distance, and then it should be moved to the furthest point from the PDA while monitoring the position of the laser beam at the irises. If the initial alignment was satisfactory, the beam should only move slightly, which can again be corrected with the PDA optics. While moving the delay line back to its original position the position of beam on the irises should again be monitored, such that it remains aligned throughout the procedure. It is important for the beam to be collimated by the telescope, since only a collimated beam will focus properly to generate continuum in the ZnCl_2 cell (C). At this point there should be a visible amount of continuum exiting the ZnCl_2 cell, which should be easily seen at the sample after filtering the pump with either the low or high bandpass dielectric filters discussed above. The lenses, L3, should focus the continuum at the sample; once aligned it is not necessary to adjust them daily. Similarly the two lenses positioned after the sample, which focus the signal tightly into the fiber optics (FO), should not be adjusted on a daily basis. These lenses

remain in good alignment as long as the PDA beam passes through all the irises. The position of the pump beam at the sample should be adjusted utilizing the pump mirror, PM, to spatially overlap it with the continuum beam at the sample. This spatial overlap is approximate, and should be maximized once the sample is in place and signal is observed.

Once the pump and probe beams are passing through the sample, zero-time must be found. Although zero-time only drifts slightly on a daily basis, it is good practice to re-define it before each session. The stimulated emission of a $10^{-2} - 10^{-3}$ M methanol solution of DODCI laser dye (3,3'-deithyloxadicarbocyanine iodide; Kodak) placed in a 1 mm pathlength cell provides a simple means to obtain a "rough" zero-time (± 10 ps). The DODCI solution should be placed at the sample, S, with the low pass dielectric filter placed after the continuum generation cell. The monochromator grating should be set at a window to the red of the excitation (setting 167.5 or 172), and a slit width of 20 μm . The white light reaching the detector from each fiber optic should be monitored when the pump beam is blocked utilizing the PI software in the free-running mode with, for example, a 0.33 s exposure time. The signal from either array should not saturate the detectors, and their profiles should be similar in shape and intensity. If the signal from one or both diode arrays is too high, then the monochromator slit should be closed until the signal no longer saturates the detectors. The slit widths suggested herein should be utilized as guidelines and adjusted as needed as described, since the amount of continuum reaching the detectors is likely to vary on a daily basis depending on the PDA power and beam profile. In cases where one signal is larger than the other, the fiber optic mounts should be moved to maximize the signal of the diode array with low light intensity. At this point the pump beam should be

allowed to excite the sample. If the delay line is set at time prior to zero (negative times), then no change in signal intensities should be observed. However, at positive times (from 0 – 200 ps) a very large signal increase will be observed due to stimulated emission from the DODCI solution; the slits will have to be closed to $\sim 2 \mu\text{m}$ to avoid detector saturation. If this signal is not present, the delay line should be moved until it is observed (lack of stimulated emission may also be due of poor pump/probe overlap). Once the stimulated emission from DODCI is located in time, the delay line should be slowly moved toward shorter beam travel distances (towards zero) until the signal disappears. One should move it back to the maximum of the signal, and this is a “rough” zero-time.

An accurate zero-time can be obtained utilizing any highly absorbent sample, such as DODCI or a Zn-substituted porphyrin, and should be found prior to each experimental session. Both compounds have large absorption cross sections in the blue (420 – 460 nm), thus it is necessary to move the monochromator grating to a blue spectral window (setting of 110 or 120), to open the slit to $50 \mu\text{m}$, and to place the short bandpass dielectric filter after the ZnCl_2 cell. The sample should be in place and the intensity of the continuum at the detectors should be adjusted as described above. When the pump beam is allowed to excite the sample, a distinct absorption should be observed at $\sim 450 \text{ nm}$ in real time. The spatial overlap between pump and probe can be maximized by adjusting the position of the pump beam with the pump mirror (PM) while monitoring the largest white light absorption. The spectra at several delay times about the “rough” zero-time should be collected at $\sim 2 \text{ ps}$ steps. Collection of spectra is performed typically by adding 400 exposures each of 0.33 s, with and without the pump beam as described above. A background spectrum should also be collected prior to

each experimental session, with the same number of scans and exposure time with both pump and probe beams blocked. Once the transient absorption spectra are calculated as described above (eq 3), the profiles at each delay time should be compared. Due to spectral chirp, the blue end of the continuum reaches the sample before the red, with a time lag comparable to the pulse width. At zero-time only part of the spectrum, the blue half, is observed. As one moves towards positive times, 2 ps, the full spectrum is observed, whereas moving 2 ps toward negative times the signal becomes zero. This “half spectrum” is characteristic of zero-time and should be observed daily. This method of obtaining zero-time is convenient in that the “half spectrum” is observed in both the red and blue windows with any sample. However, due to the time-lag between red and blue light, the zero-time determined in the red spectral windows corresponds to 5 ps in the blue. Once zero-time is determined, spectra can be collected as described above at different pump-probe delay times by moving the delay line between spectra.

C. RESULTS AND DISCUSSION

1. Electron Transfer in 1-H and 1-D

The ability of the donor to transfer an electron to the acceptor through the proton interface is predicated on their propensity to form donor/acceptor hydrogen-bonded heterodimers. Evidence of this interaction is observed in the ^1H NMR spectrum, where the carboxy resonances broaden and shift downfield as the acid concentration is increased. This behavior is expected for faster proton exchange at higher concentration, which is accompanied by

a greater dimer/monomer ratio.⁸⁸⁻⁹² The observed carboxy proton shifts with concentration for both ZnPCOOH and 3,4-dinitrobenzoic acid (DNBCOOH) are listed in Table II, along with the corresponding full-width at half-maximum (FWHM). Exemplary NMR spectra of ZnPCOOH, DNBCOOH, and their mixture at the same total acid concentration are shown in Figure 4; it is evident from the spectrum of the mixture that the ZnPCOOH and DNBCOOH acid functionalities are interacting, since only one carboxy peak is observed. The carboxy proton shifts with their corresponding FWHM for the mixed solutions are listed in Table III; they are clearly different from those of each individual component at the same total acid concentration. Binding constants may be derived from the shift in the NMR signal when the position of the monomer and dimer resonances are extracted from the low and high concentration limits, respectively. However, as is often the case for dimerizations of moderate binding constants, very high acid concentrations are necessary to reach the limiting condition.⁹³ Unfortunately the acids utilized in our donor/acceptor pairs are not sufficiently soluble in low polarity solvents such as CD_2Cl_2 to approach the high concentration limit, and therefore binding constants cannot be deduced.

The IR spectra of carboxylic acids typically exhibit resolved monomer and dimer bands in the CO and OH stretching regions, and the dimer/monomer relative intensities change with concentration. From this acid concentration dependence the homo- and heterodimerization binding constants can be derived.^{88,89,94} Table IV lists the vibrational frequencies of DNBCOOH and ZnPCOOH in the CO and OH stretching regions. The IR spectra of both acids separately and their mixtures are shown in Figure 5 at three representative concentrations. In all cases, the relative absorbance of

Table II. Observed ^1H NMR Shifts and FWHM of Carboxy Proton Resonances of CD_2Cl_2 Solutions of DNBCOOH and ZnPCOOH at Selected Concentrations of the Acid.

| [Acid]/M | DNBCOOH | | ZnPCOOH | |
|--------------------|----------------------------------|----------|----------------------------------|----------|
| | $\delta_{\text{obs}}/\text{ppm}$ | FWHM/ppm | $\delta_{\text{obs}}/\text{ppm}$ | FWHM/ppm |
| 8×10^{-4} | 1.60 | 0.37 | 1.52 | 0.07 |
| 2×10^{-3} | 2.09 | 1.0 | 1.53 | 0.07 |
| 6×10^{-3} | 3.00 | 1.6 | 1.54 | 0.27 |

Table III. Observed ^1H NMR Shifts and FWHM of Carboxy Proton Resonances of CD_2Cl_2 Solutions of DNBCOOH/ZnPCOOH at Selected Concentrations of the Acid Mixture.

| [DNBCOOH]/M | [ZnPCOOH]/M | [Acid]/M | DNBCOOH/ZnPCOOH | |
|--------------------|--------------------|--------------------|----------------------------------|----------|
| | | | $\delta_{\text{obs}}/\text{ppm}$ | FWHM/ppm |
| 4×10^{-4} | 4×10^{-4} | 8×10^{-4} | 1.59 | 0.17 |
| 1×10^{-3} | 1×10^{-3} | 2×10^{-3} | 1.75 | 0.35 |
| 3×10^{-3} | 3×10^{-3} | 6×10^{-3} | 2.26 | 0.50 |

Table IV. Monomer and Dimer Vibrational Frequencies of DNBCOOH and ZnPCOOH in the OH and CO Stretching Regions.

| Acid | $\nu(\text{OH})_{\text{M}}/\text{cm}^{-1}$ | $\nu(\text{CO})_{\text{M}}/\text{cm}^{-1}$ | $\nu(\text{CO})_{\text{D}}/\text{cm}^{-1}$ |
|---------|--|--|--|
| DNBA | 3478 | 1751 | 1715 |
| ZnPCOOH | 3489 | 1744 | 1713 |

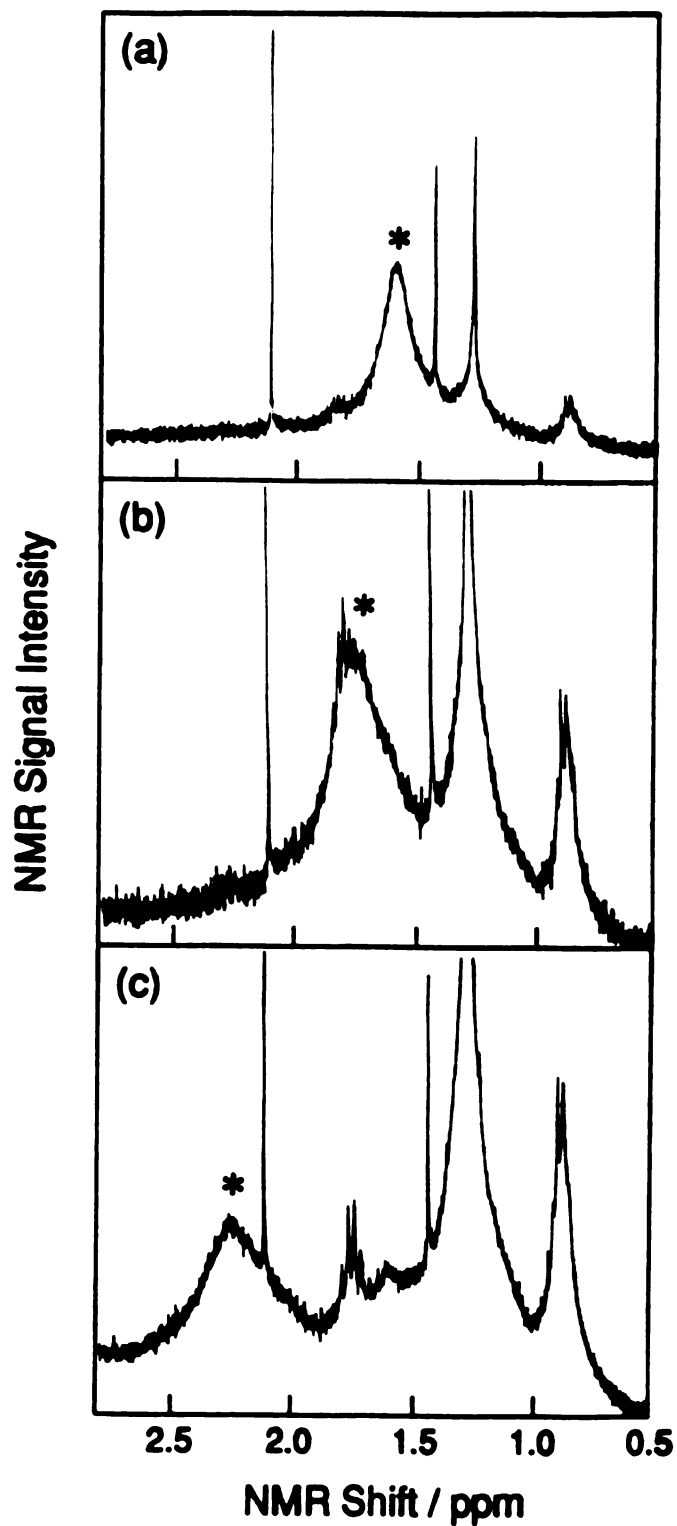


Figure 4. ^1H NMR spectra of CD_2Cl_2 solutions containing DNBCOOH and ZnPCOOH where the concentration of each component is 4×10^{-4} M (top), 1×10^{-3} M (middle), and 3×10^{-3} M (bottom). The carboxy proton is denoted by (*) in all spectra.

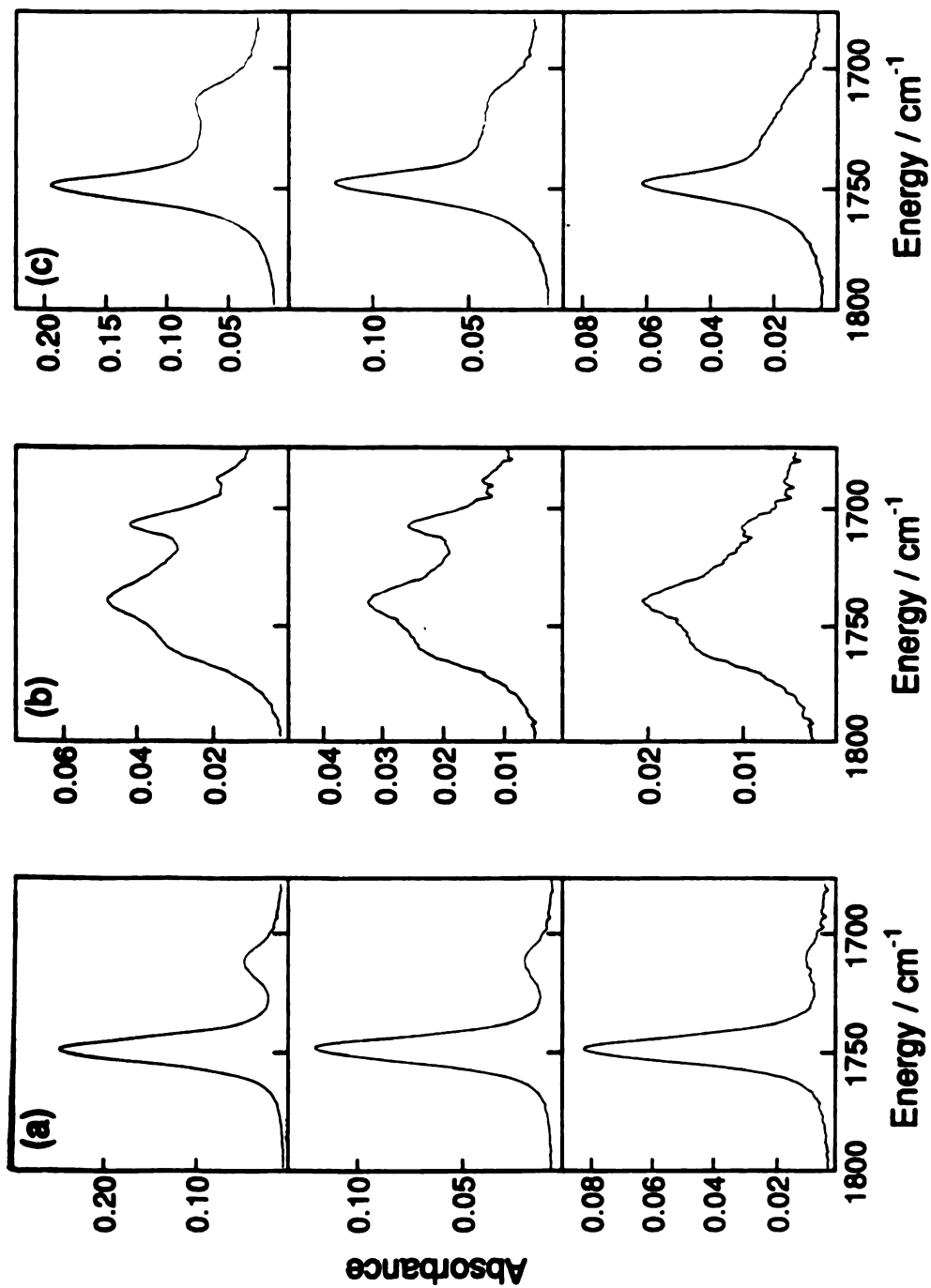


Figure 5. FTIR spectra in the CO stretching region of CH_2Cl_2 solutions of (a) DNBA, (b) ZnPCOOH , and (c) DNBA and ZnPCOOH . The concentrations of each component for (a), (b), and (c) are 1.6×10^{-3} M (top), 1.0×10^{-3} M (middle), 4.0×10^{-4} M (bottom).

the CO stretch of the monomer to that of the dimer, A_M/A_D , decreases with increasing acid concentration; this observation is consistent with an increased formation of dimer. The dimer band in the OH region was not observed since it is very broad and lies under the solvent $\nu(\text{CH})$ bands.

The binding constant for self-association of each acid can be calculated from the dependence of the monomer absorption on concentration, as derived by Affsprung⁹⁵ and others.^{88,89} The absorbance of the monomer, A_M , at $\nu(\text{OH})_M$ or $\nu(\text{CO})_M$, with molar absorptivity ϵ_M and path length b , can be related to the initial acid concentration, $[\text{C}]_0$, by the equation

$$\frac{[\text{C}]_0}{A_M} = \frac{1}{\epsilon_M b} + \frac{2K_{CC}}{(\epsilon_M b)^2} A_M \quad (4)$$

The value of ϵ_M can be obtained from the intercept of a plot of $[\text{C}]_0/A_M$ vs. A_M ; then from the slope the self-association binding constant, K_{CC} , can be calculated. Table V lists the values of ϵ_M and K_{CC} for solutions of containing only DNBCOOH or ZnPCOOH.

The hetero-association binding constant between DNBCOOH and ZnPCOOH can be obtained using the equation below derived by Affsprung⁹⁵

$$\frac{[\text{ZnPCOOH}]_0}{[\text{ZnPCOOH}]_M} - 2K_{DD}[\text{ZnPCOOH}]_M = 1 + K_{DZ}[\text{DNBCOOH}]_M \quad (5)$$

where $[\text{ZnPCOOH}]_0$ represents the initial concentration of ZnPCOOH, $[\text{DNBCOOH}]_M$ and $[\text{ZnPCOOH}]_M$ are the monomer concentrations of each acid, K_{DD} is the ZnPCOOH self-association binding constant, and K_{DZ} is the hetero-association binding constant. The monomer concentrations are calculated from the absorbance of the monomer peaks and the ϵ_M values

Table V. Calculated Self-Association Binding Constants for DNBCOOH and ZnPCOOH in CH₂Cl₂ at Room Temperature.^a

| Acid | ν(CO) region | | | ν(OH) region | |
|------|-------------------|--|--------------------------------|--|-------------------|
| | K/M ⁻¹ | ε _M /M ⁻¹ cm ⁻¹ | K/M ⁻¹ ^b | ε _M /M ⁻¹ cm ⁻¹ | K/M ⁻¹ |
| DNB | 220±90 | 1080±90 | 320±60 | 170±20 | 210±110 |
| ZnP | 1000±600 | 360±110 | 2600±900 | 120±60 | <i>c</i> |

^aData listed in Tables AI – AIII in the Appendix. ^bDetermined from the ratio of A_M/A_D. ^cCould not be determined due to large measurement error.

obtained from the intercept of eq 4 at each frequency (Table III). In our case at the maximum of the each monomer ν(CO) band there is considerable absorption from the other acid, and therefore the monomer concentrations were calculated from the two-equation two-unknown problem:

$$A_{1751} = \epsilon_{1751}^{\text{DNB}} b [\text{DNBCOOH}]_{\text{M}} + \epsilon_{1751}^{\text{ZnP}} b [\text{ZnPCOOH}]_{\text{M}} \quad (6)$$

$$A_{1744} = \epsilon_{1744}^{\text{DNB}} b [\text{DNBCOOH}]_{\text{M}} + \epsilon_{1744}^{\text{ZnP}} b [\text{ZnPCOOH}]_{\text{M}}$$

A plot of the left side of eq 5 vs [ZnPCOOH]_M should yield an intercept of unity and a slope = K_{DZ}. From the absorbance vs concentration data, analyzed according to eq 5, the linear plot shown in Figure 6 was constructed; it has an intercept of 1.09 and a slope (= heteroassociation binding constant) of 600 ± 250 M⁻¹.

Evidence of electron transfer after heterodimer formation is obtained from static quenching experiments in which the intensity of the ZnPCOOH

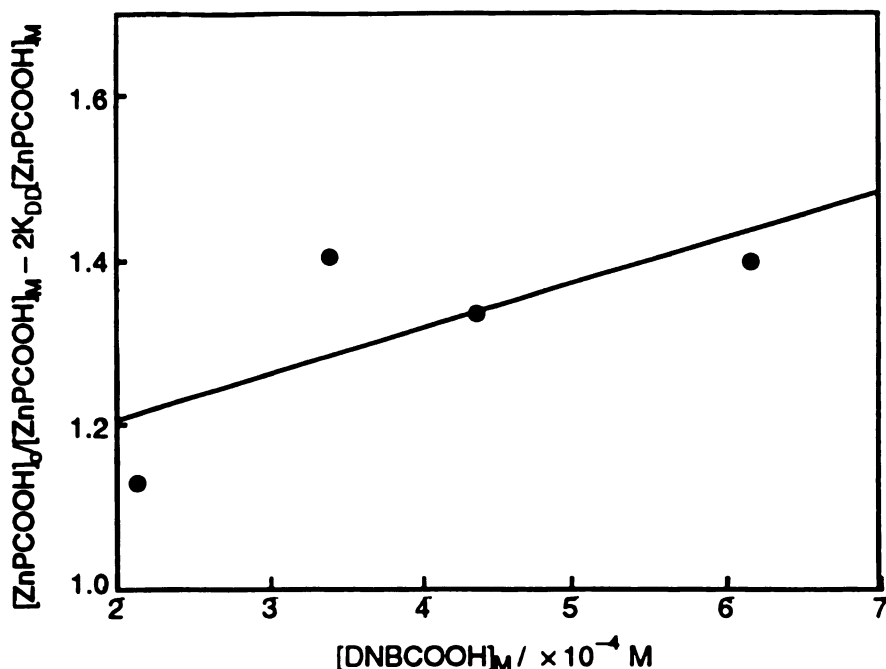


Figure 6. Plot of the left side of eq 5 vs [DNBCOOH].

fluorescence and the its emissive lifetime are monitored as a function of DNBCOOH concentration. Because the electron transfer rate for a donor/acceptor bound pair is expected to be much faster than the lifetime of the $^1\pi\pi^*$ excited state, emission from ZnPCOOH which is bound to an acceptor will not be observed. Since the donor/acceptor pair does not emit, its lifetime cannot be monitored, and only the decay of unbound species will be observed.⁹⁶ Therefore as the quencher concentration is increased the total emission of the sample decreases, while the fluorescence lifetime remains constant. Experiments involving static quenching of the ZnPCOOD emission by DNBCOOD are in agreement with this interpretation, inasmuch as the fluorescence decay remains constant (Figure 7). If the self-association

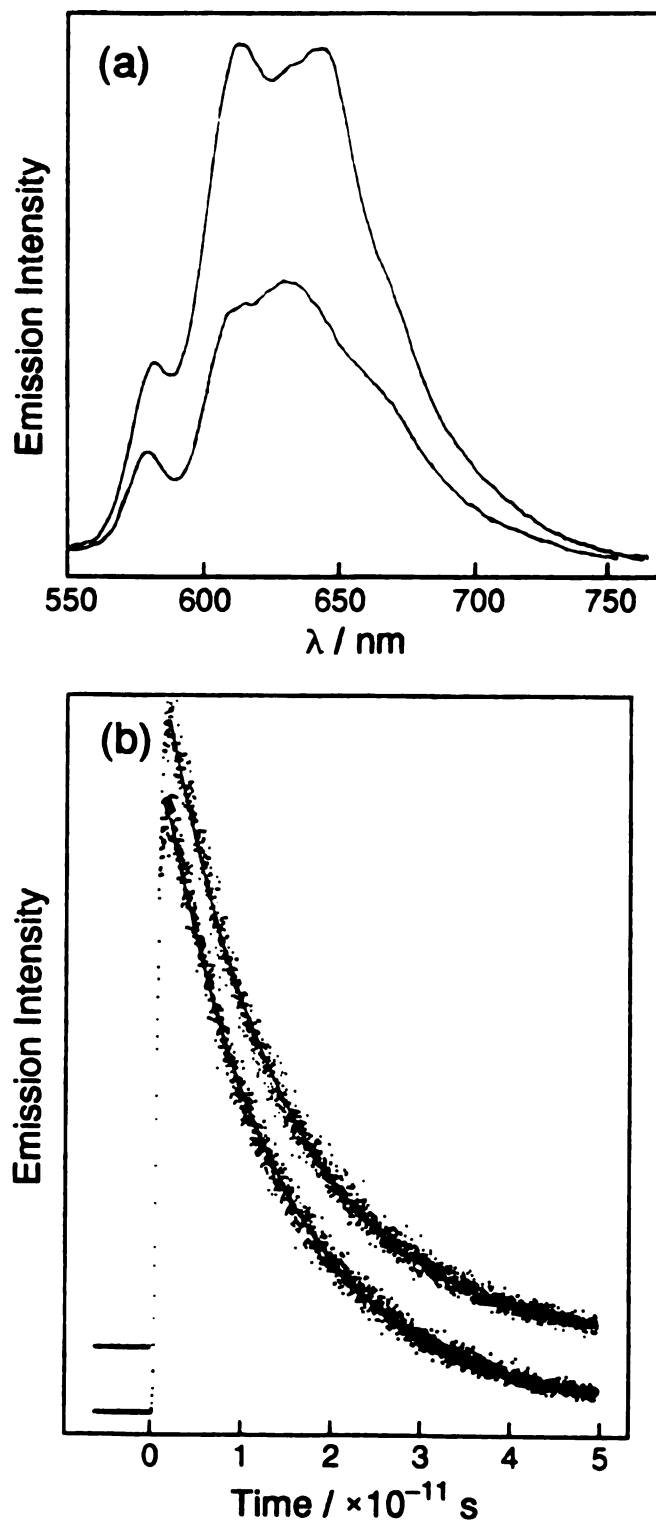


Figure 7. (a) Emission spectra and (b) luminescence decays of CH_2Cl_2 solutions of ZnPCOOD in the absence (top trace) and presence (bottom trace) of 10^{-2} M DNBCOOD.

binding constants obtained from IR spectroscopy are employed, analysis of the emission quenching yields a hetero-association binding constant of 316 M^{-1} for the deuterated acids in dichloromethane and 698 M^{-1} for the ZnPCOOH/DNBCOOH pair in *o*-dichlorobenzene.⁹⁷

The absorption spectrum of the ZnPCOOCH_3^+ was obtained by collecting a transient absorption spectrum of a CH_2Cl_2 solution of ZnPCOOCH_3 ($\lambda_{\text{ex}} = 532 \text{ nm}$, FWHM = 10 ns) in the presence of the electron acceptor tetracyanoethylene (TCNE) in the nanosecond timescale.⁹⁸ The bimolecular electron transfer takes place from the porphyrin's $^3\pi\pi^*$ excited state which has a strong absorption feature at 460 nm ($E_{00} = 1.7 \text{ eV}$)⁶⁸ to TCNE, whose radical anion spectrum has a characteristic vibronic progression in the 400 - 500 nm region with a maximum at 435 nm ($\epsilon = 7100 \text{ M}^{-1}\text{cm}^{-1}$).⁹⁹ Addition of TCNE results in quenching of the porphyrin's $^3\pi\pi^*$ excited state lifetime, with concomitant growth of the TCNE⁻ and ZnPCOOCH_3^+ features (Figure 8). The ZnPCOOCH_3^+ absorption spectrum has a maximum at 675 nm with a shoulder at 640 nm, as shown in Figure 8, in agreement with spectral profiles previously reported for other Zn-substituted porphyrins.^{100,101} Attempts to obtain ZnPCOOH^+ spectra in the presence of TCNE or methylviologen were unsuccessful; presumably there was irreversible protonation of the acceptor following the electron transfer, since charge recombination is slow (μs - ms) in these bimolecular systems. Bulk electrolysis of ZnP lead to demetallation of the porphyrin within minutes following cation formation. Oxidation with agents such as silver nitrate yield an absorption spectrum with a maximum at 640 nm,¹⁰² which is shifted from that observed in the transient absorption experiments. The absorption spectra of a number of reduced substituted nitrobenzenes and

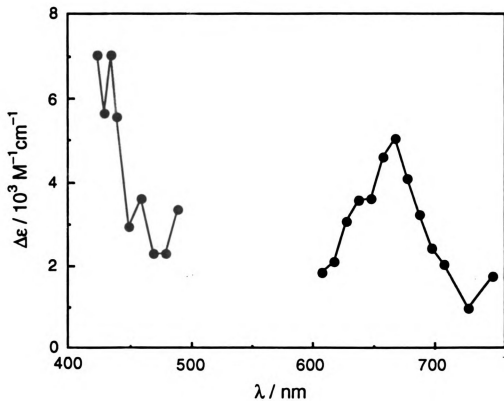


Figure 8. Transient absorption spectrum of a CH_2Cl_2 solution of TCNE and ZnPCOOCH_3 collected 1 μs after the laser pulse (10 ns, 532 nm)

dinitrobenzenes have been reported, and their spectra show absorption maxima at approximately 300 and 830 nm.⁷⁹

The transient absorption spectra of the of CH_2Cl_2 solutions of ZnPCOOH (Figure 9) and ZnPCOOD (Figure 10), collected 15 ps and 1.5 ns after excitation with 580 nm amplified pulses, respectively, correspond to the $^1\pi\pi^*$ and $^3\pi\pi^*$ excited states. These spectra are in excellent agreement with those obtained for other Zn-substituted porphyrins.^{51c,103} The $^3\pi\pi^*$ absorption exhibits a blue shift of the large positive feature at 455 nm compared to the $^1\pi\pi^*$ absorption, possibly due to decreased bleaching in the Soret region. The singlet spectra, both in the red and blue regions, have an apparent 10 ps risetime and subsequently decay slowly over hundreds of picoseconds. The emissive lifetimes of the $^1\pi\pi^*$ excited states are 1.4 and 1.5 ns for ZnPCOOH and ZnPCOOD , respectively, measured by time-correlated single photon counting (see insets in Figures 9 and 10).¹⁰⁴ Figure 11 shows the excited state spectrum of ZnPCOOD in the red, where the $^1\pi\pi^*$ exhibits a peak at 660 nm; while absorption due to the $^3\pi\pi^*$ state is significant, yet does not exhibit marked features in the 630 - 750 nm region.

Addition of DNBCOOH to CH_2Cl_2 solutions of ZnPCOOH results in the growth of a new absorption feature with a maximum at 685 nm, as shown in Figure 12, which is attributable to the ZnPCOOH^+ . The decay rates at 600 nm, where the $^1\pi\pi^*$ excited state absorbs, and at 685 nm are biphasic and concentration independent in the range $[\text{ZnPCOOH}] = 1.0$ to 1.6×10^{-3} M and $[\text{DNBCOOH}] = 5.0$ to 40×10^{-3} M.¹⁰⁵ Table VI lists the decays of 1-H obtained at several donor and acceptor concentrations followed at 660 and 685 nm. The 20 ps decay is attributed to the disappearance of the $^1\pi\pi^*$ excited state, quenched by fast electron transfer to DNBCOOH . Since k_{CS} is fast compared to the rate constant for excited state

Table VI. Concentration Dependence of the Charge Separation and Charge Recombination Rates of 1-H in CH₂Cl₂.

| [ZnPCOOH] / M | [DNBCOOH] / M | $k_{CS} / 10^{10} \text{ s}^{-1}$ | $k_{CR} / 10^{10} \text{ s}^{-1}$ |
|----------------------|----------------------|-----------------------------------|-----------------------------------|
| 1.0×10^{-3} | 5.0×10^{-3} | 3.7 | <i>a</i> |
| 1.0×10^{-3} | 1.4×10^{-2} | 4.2 | <i>a</i> |
| 1.6×10^{-3} | 1.4×10^{-2} | 4.8 | <i>a</i> |
| 1.6×10^{-3} | 1.9×10^{-2} | 7.7 | 1.0 |
| 1.6×10^{-3} | 4.0×10^{-2} | 5.0^b | 1.0^b |

^aSignal too weak to measure rates. ^bSignal at these concentrations is the most reliable and was measured at least ten times.

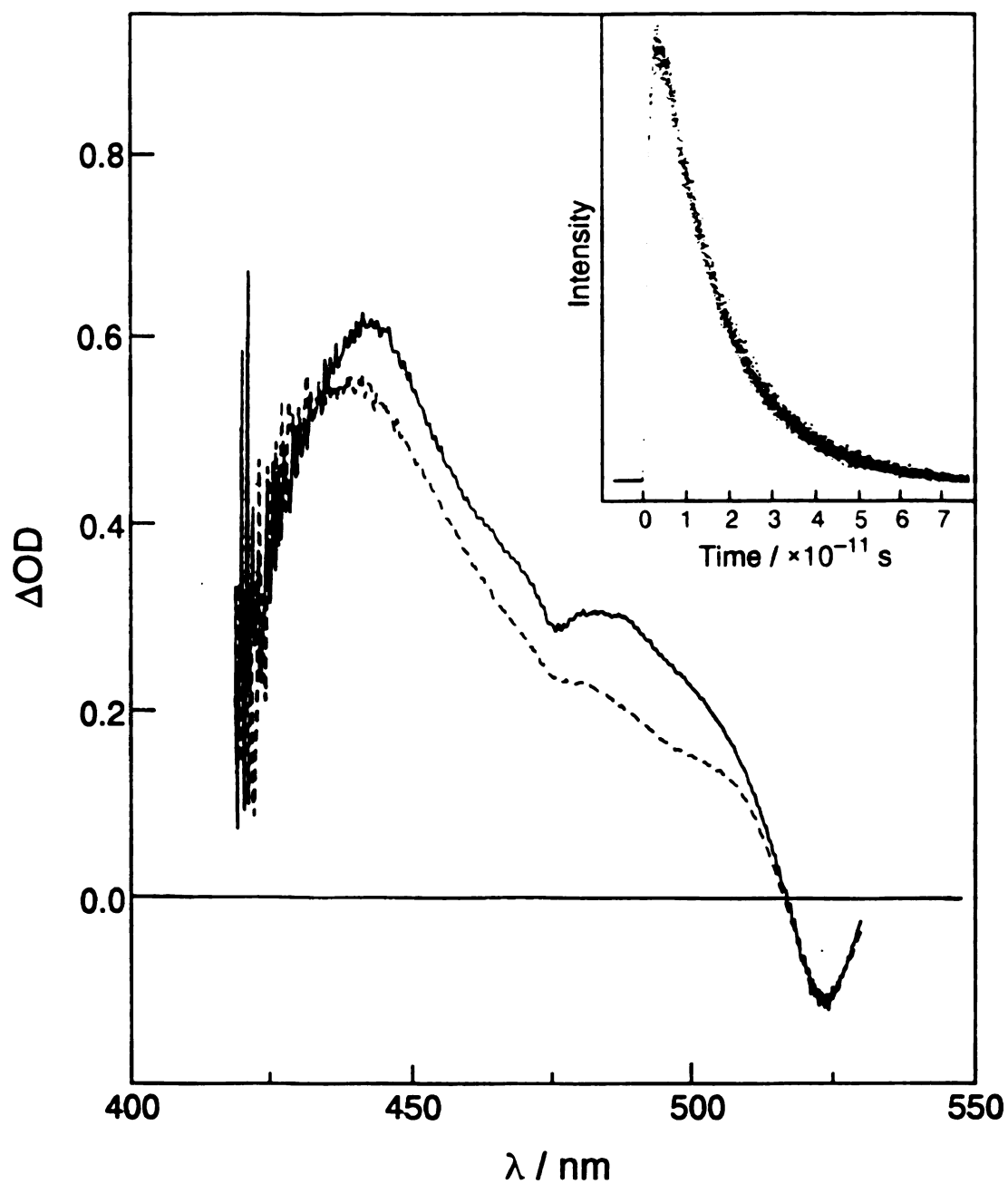


Figure 9. Transient absorption spectra of ZnPCOOH collected 15 ps (—) and 1.5 ns (---) after the excitation pulse.

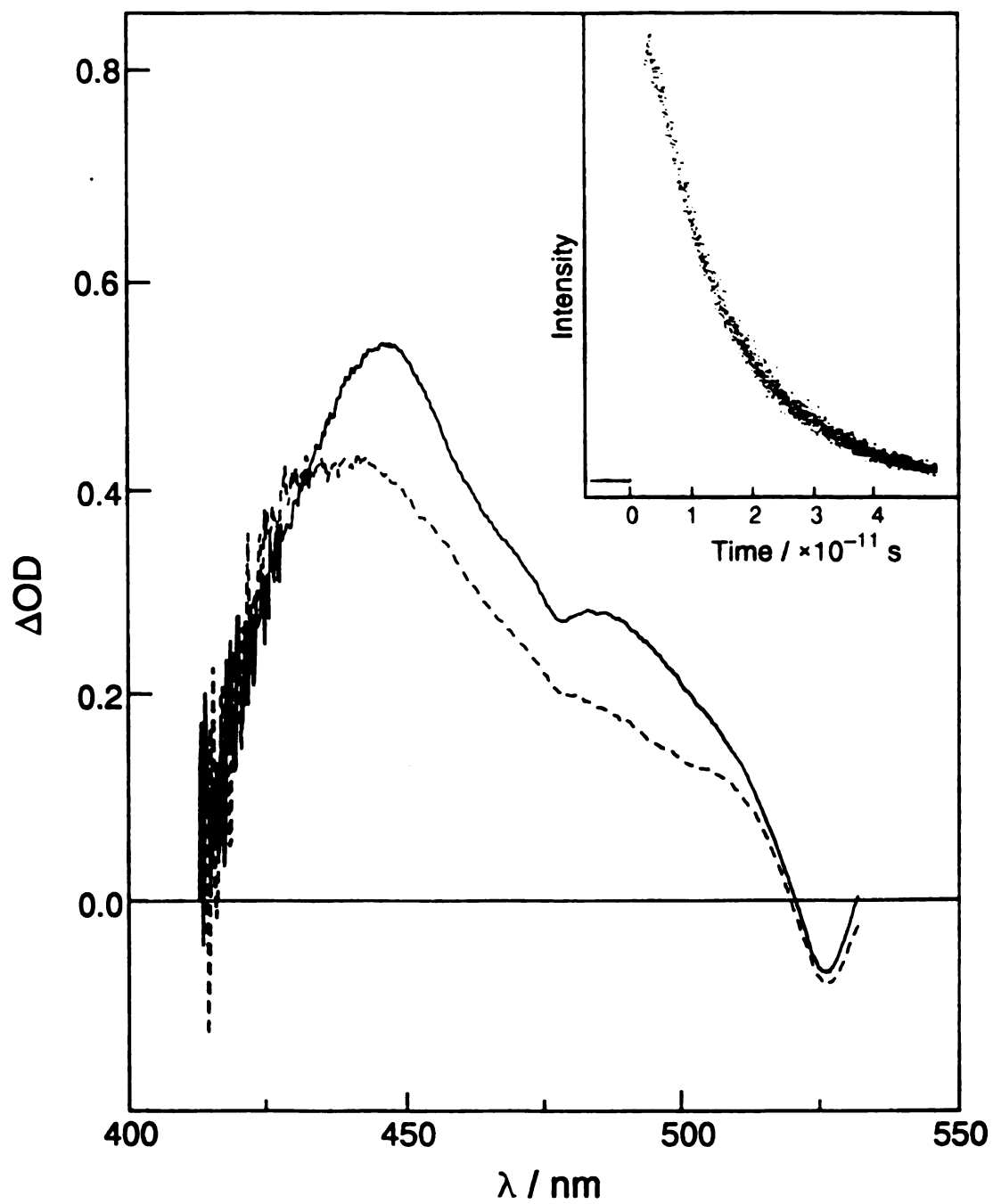


Figure 10. Transient absorption spectra of ZnPCOOD collected 15 ps (—) and 1.5 ns (---) after the excitation pulse.

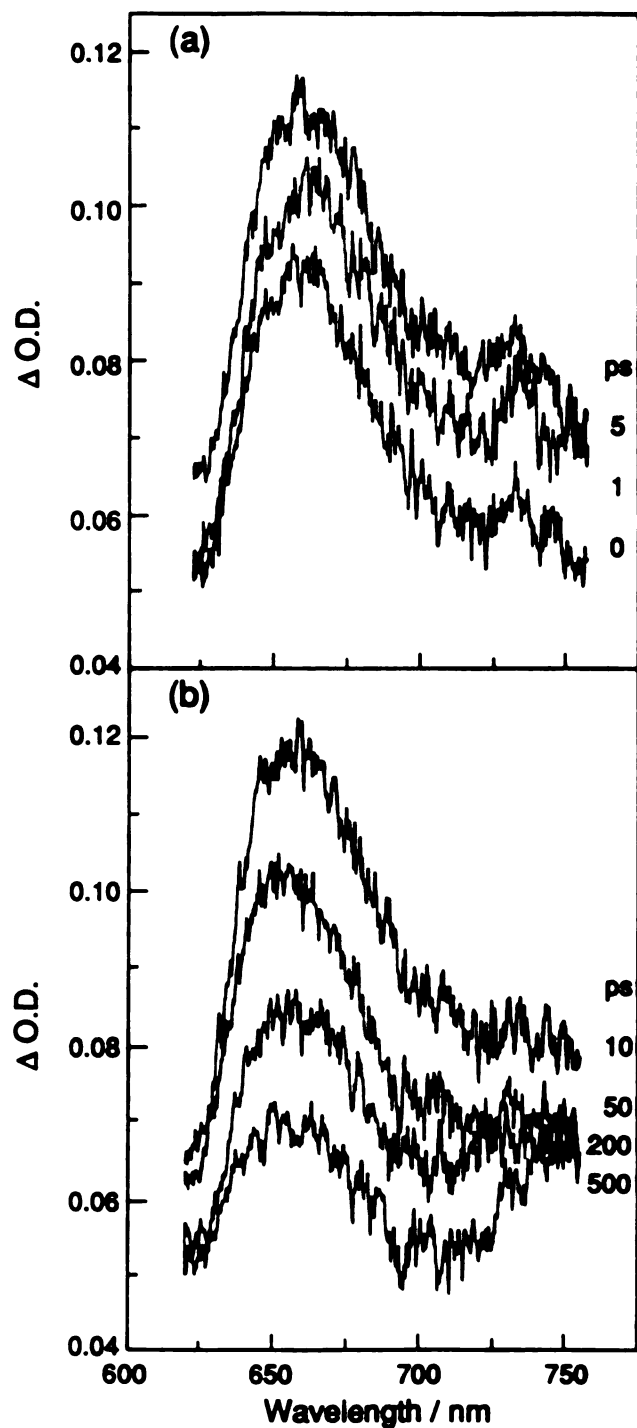


Figure 11. Transient (a) rise and (b) decay of the $1\pi\pi^*$ excited state of a 10^{-3} M CH_2Cl_2 solution of $ZnPCOOH$ in the 625 – 760 nm region.

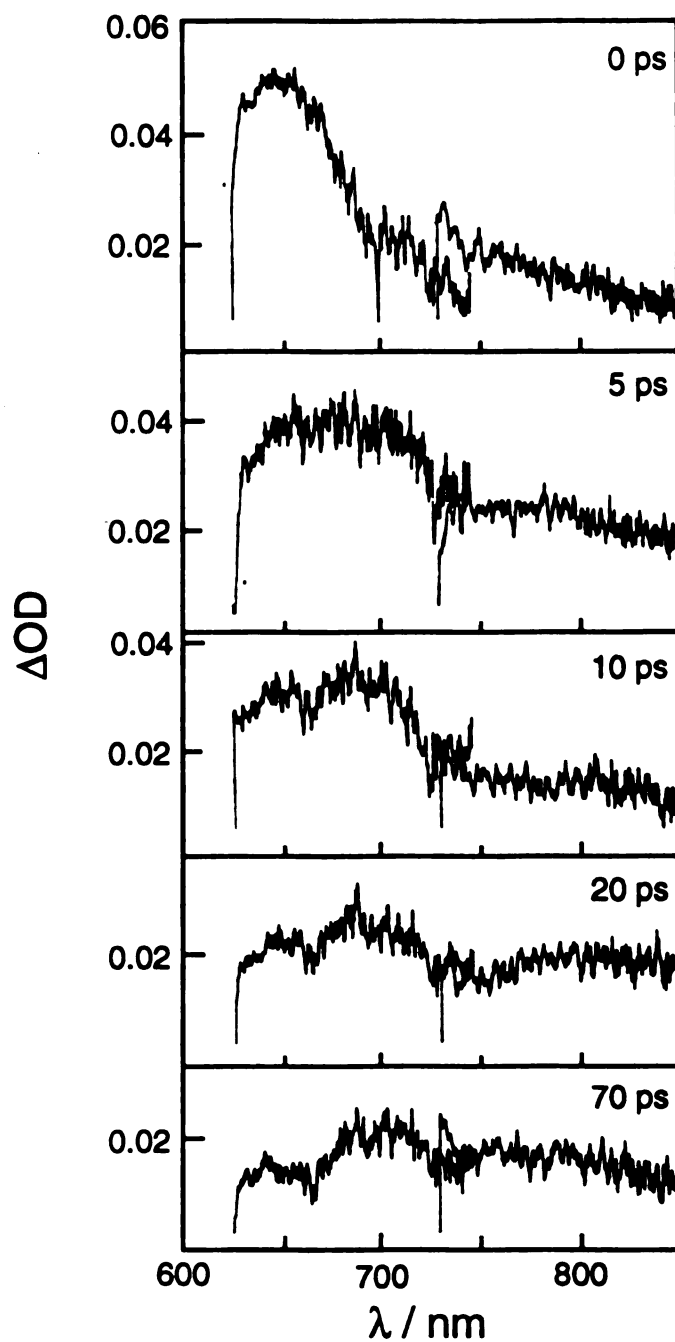


Figure 12. Transient absorption spectra at various delay times after the 580 nm, 3 ps excitation pulse of ZnPCOOH (1.4×10^{-3} M) and DNBCOOH (4×10^{-2} M) in CH_2Cl_2 .

decay, it represents the forward electron transfer rate, $k_{CS} = 5.0(5) \times 10^{10} \text{ s}^{-1}$. The rate of charge recombination, k_{CR} , is attributed to the longer decay, which corresponds to a rate constant of $1.0(2) \times 10^{10} \text{ s}^{-1}$. Figure 13 shows the transient absorption spectra obtained with the deuterated pair, 1-D, where the electron transfer rates were found to be $k_{CS} = 3.0(3) \times 10^{10} \text{ s}^{-1}$ and $k_{CR} = 6.2(3) \times 10^9 \text{ s}^{-1}$.

Esterification of the donor to the methyl ester, ZnPCOOCH₃, and acceptor to the ethyl ester, DNBCOOEt,¹⁰⁶ results only in bimolecular quenching of the porphyrin's $^1\pi\pi^*$ excited state. The transient absorption spectra of ZnPCOOCH₃ at various delay times in the presence of $5 \times 10^{-2} \text{ M}$ DNBCOOEt are shown in Figure 14. The singlet peak at 660 nm decays monotonically with a lifetime of 500 ps. Owing to the short lifetime of the porphyrin $^1\pi\pi^*$ excited state, quenching by a diffusion controlled electron transfer ($k_q = 1.8 \times 10^{10} \text{ M}^{-1}\text{s}^{-1}$) is inefficient; thus the singlet is only slightly quenched even with a large concentration of DNBCOOEt. Therefore the quantum yield for the production of charge separated product is low, and features due to the porphyrin cation features are not observed.

The ET process in the hydrogen-bonded pre-associated pair (1) shows a pronounced deuterium isotope effect, k_H/k_D . The ratio for the rates of charge separation and recombination are 1.7(3) and 1.6(4), respectively. The magnitudes are consistent with the 1.7 – 2.0 deuterium isotope effects measured for the oxidation of a soluble analog of Vitamin E by organochloro peroxides.¹⁰⁷ In this latter system, the rate determining step has been proposed to involve the transfer of an electron from substrate to the peroxy radical via a hydrogen bonding network formed by the incipient hydroperoxide and solvent.

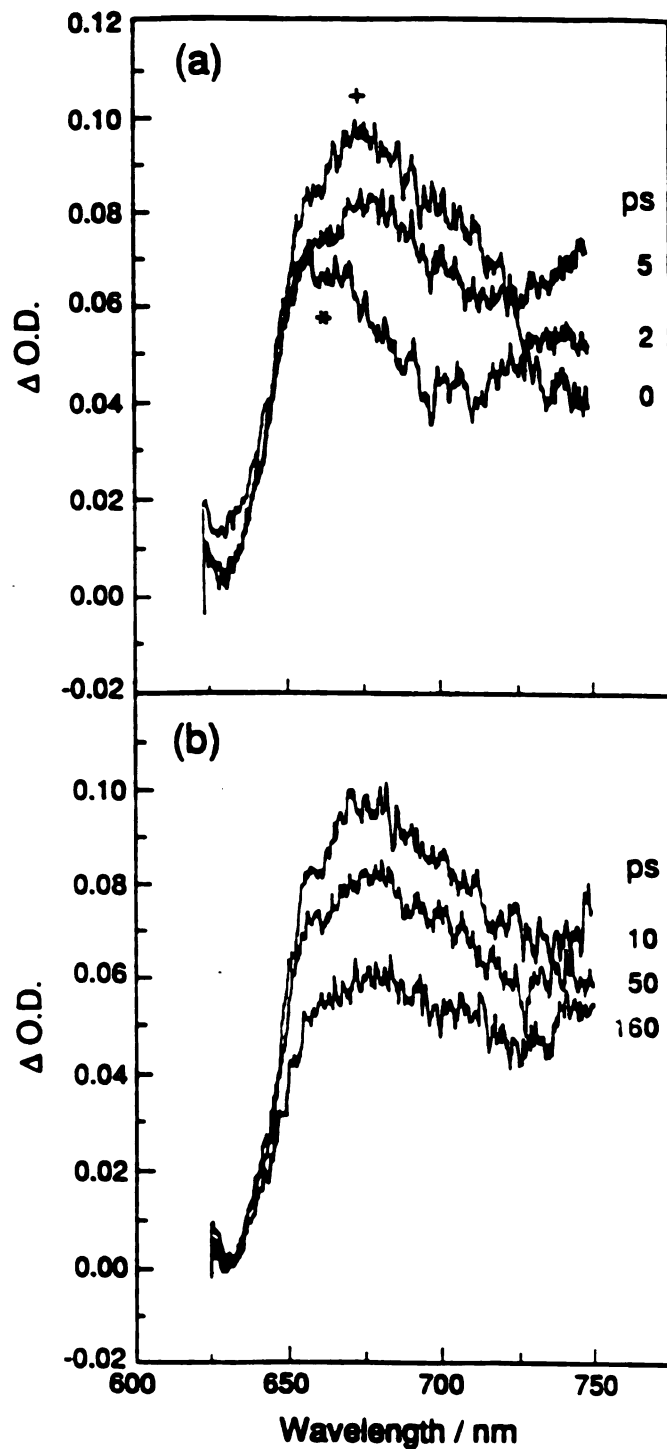


Figure 13. Transient (a) rise and (b) decay of a CH_2Cl_2 solution containing $[ZnPCOOH] = 1.6 \times 10^{-3} M$ and $[DNBCOOH] = 4.0 \times 10^{-3} M$ in the 625 – 760 nm region.

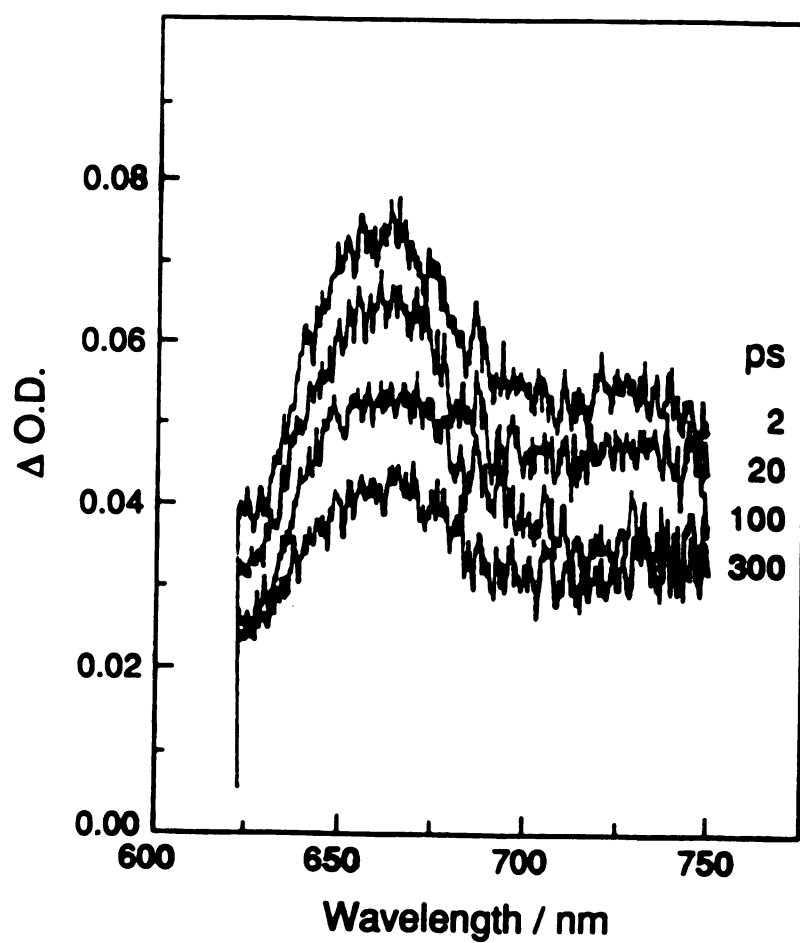


Figure 14. Transient decay of the ${}^1\pi\pi^*$ excited state of a 10^{-3} M CH_2Cl_2 solution of ZnPCOOCH_3 containing 5×10^{-2} M $\text{DNBCOOCH}_2\text{CH}_3$ in the 625 – 760 nm region.

2. Electron Transfer in Systems 2 and 3

Preliminary studies have been conducted with two other acceptors, 3,5-dinitro-*p*-toluic acid (DNTCOOH) and 9,10-anthraquinone-2-carboxylic acid (AQCOOH). The driving forces for forward and back ET are 0.8 V and 1.4 V, respectively, for **3**, which are nearly identical to those for system **1** of Section 1. DNTCOOH is more difficult to reduce than DNBCOOH, thus making the driving force for the ZnPCOOH excited state ET and subsequent charge recombination 0.6 V and 1.6 V, respectively. Therefore the electron transfer rates in the latter system are expected to be slower than those for the two other acceptors.

When DNTCOOH is added to solutions of ZnPCOOH, a new absorption feature with maximum at 460 nm is observed upon excitation, which can be attributed to ZnPCOOH⁺. The spectral profiles at selected delay times are shown in Figure 15, where a slight decrease in intensity is observed from 0 to 300 ps (Figure 15a). This initial decay is followed by the disappearance of the transient in the 1.0 to 2.5 ns timescale (Figure 15b). As is evident from the plot of $-\ln(\Delta OD_{460})$ vs time shown in Figure 16, the full decay is triphasic, with a short, 81 ps component, and two longer ones of 1.46 and 2.81 ns. The fast decay is assigned to the disappearance of the quenched ¹ππ* excited state, which is due only to ZnPCOOH hydrogen bonded to a DNTCOOH molecule. The 1.46 ns decay is consistent with that of the unquenched ¹ππ* due to unbound ZnPCOOH, whose ¹ππ* excited state in the absence of quencher is 1.45 ns (see Figure 9). At times longer than 1 ns the decay of the ZnPCOOH⁺ occurs over 2.81 ns and is attributed to charge recombination.

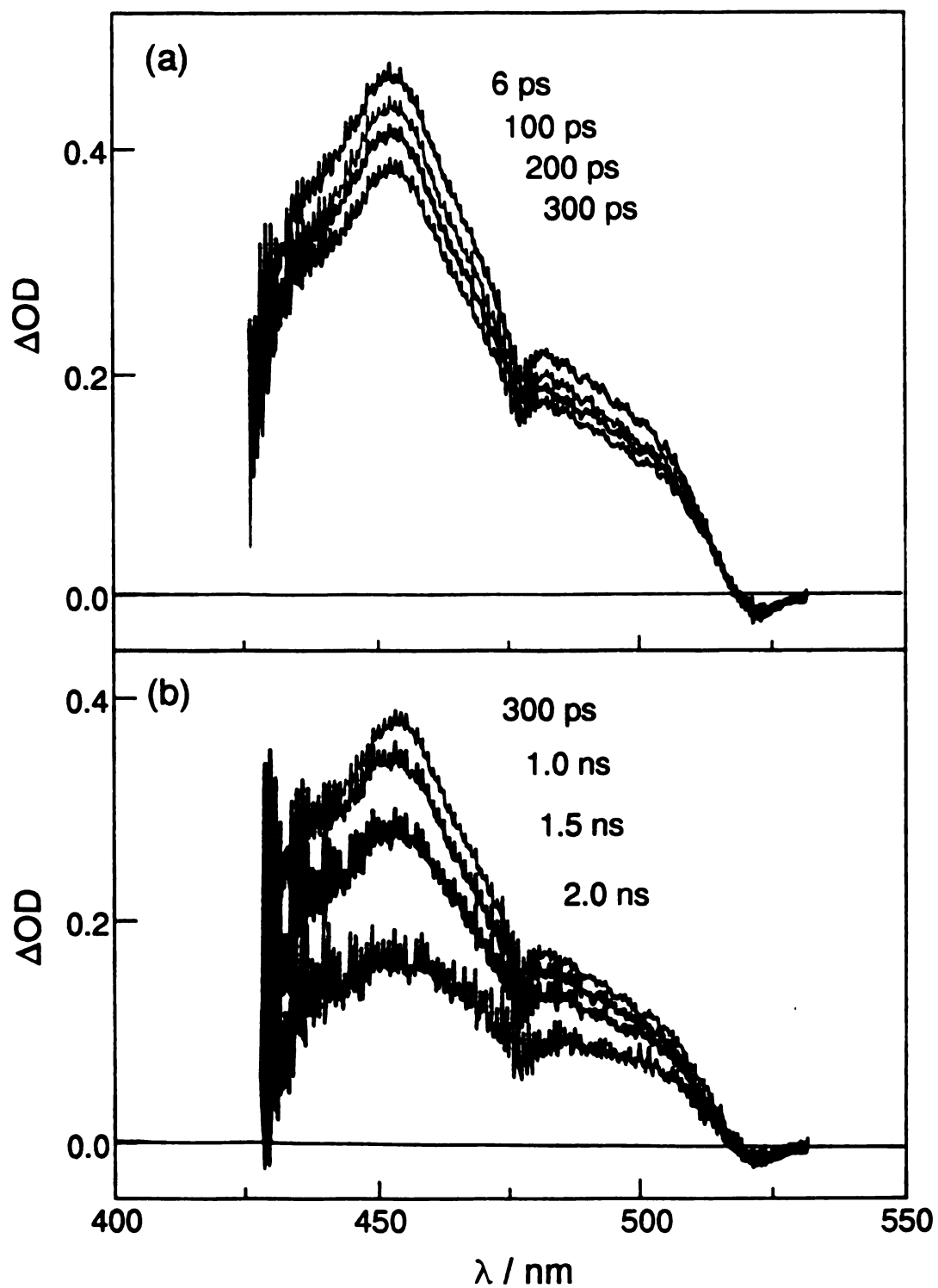


Figure 15. Transient absorption spectra at selected delay following the pump pulse of CH_2Cl_2 solutions of $[\text{ZnPCOOH}] = 10^{-3} \text{ M}$ and $[\text{DNTCOOH}] = 10^{-2} \text{ M}$ showing the decays (a) prior to and (b) after 300 ps.

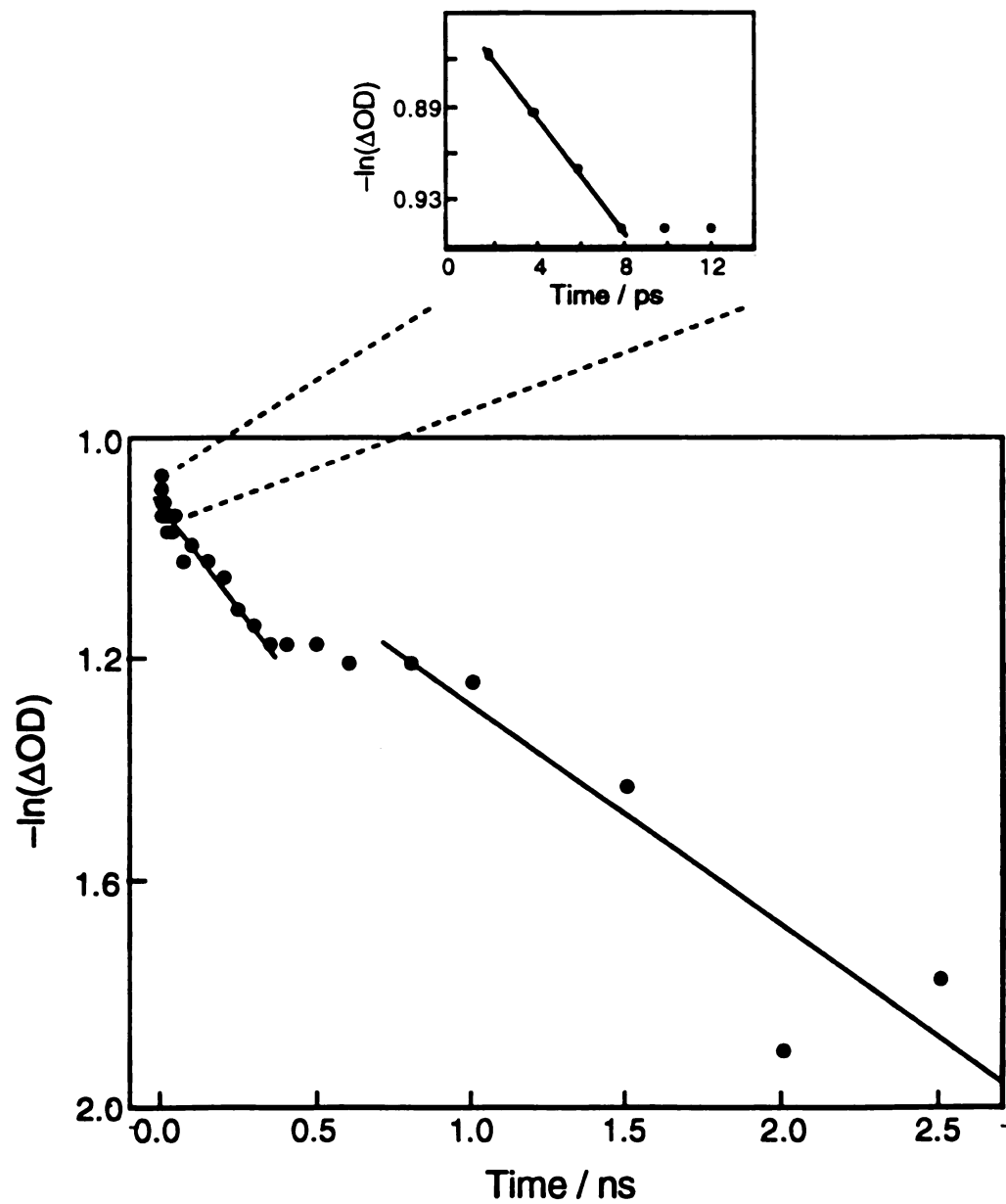


Figure 16. Plot of $-\ln(\Delta OD)$ vs time showing the triphasic decay of the ZnPCOOH/DNTCOOH pair.

The contribution of ZnPCOOH^+ to the transient spectrum can be enhanced by subtraction of the signal from the $^1\pi\pi^*$ excited state of unbound ZnPCOOH . This signal should in principle decay with the same lifetime as that in the absence of acceptor, since in conjunction with the short lifetime of the porphyrin's $^1\pi\pi^*$ excited state (1.45 ns), bimolecular quenching is not expected to play a prominent role in our concentration range ($\text{ZnPCOOH} \sim 10^{-3}$ M; $\text{DNTCOOH} \sim 10^{-2}$ M). This allows subtraction of a certain fraction of the ZnPCOOH spectrum at each corresponding delay time. However, determination of the correct fraction to be subtracted is difficult; therefore these subtracted spectra have been utilized only to aid in the assignment of the transients in a qualitative manner. Once all the spectral contributions of the $^1\pi\pi^*$ of bound ZnPCOOH molecules, which was quenched by electron transfer, have decayed, the only $^1\pi\pi^*$ excited state signal should be from unbound ZnPCOOH . Thus at 800 ps, for example, one can begin subtracting fractional components of the ZnPCOOH $^1\pi\pi^*$ spectrum until the region where only the singlet absorbs (420 – 440 nm) becomes zero. In our case this occurs when half of the ZnPCOOH spectra shown in Figure 9 is subtracted from those presented in Figure 15; the resulting spectra are shown in Figure 17. If one now subtracts this amount of the ZnPCOOH $^1\pi\pi^*$ excited state spectrum from those obtained in the presence of acceptor at short times (0 to 100 ps), the decay of the singlet in the 420 – 440 nm region is observed. Owing to the slower time scale for charge recombination, the signal from ZnPCOOH^+ at 460 nm remains of constant intensity over short times, after which it decays dramatically over 2.5 ns.. This observation is in agreement with the assignment of the short decay to the disappearance of the quenched ZnPCOOH $^1\pi\pi^*$ excited state.

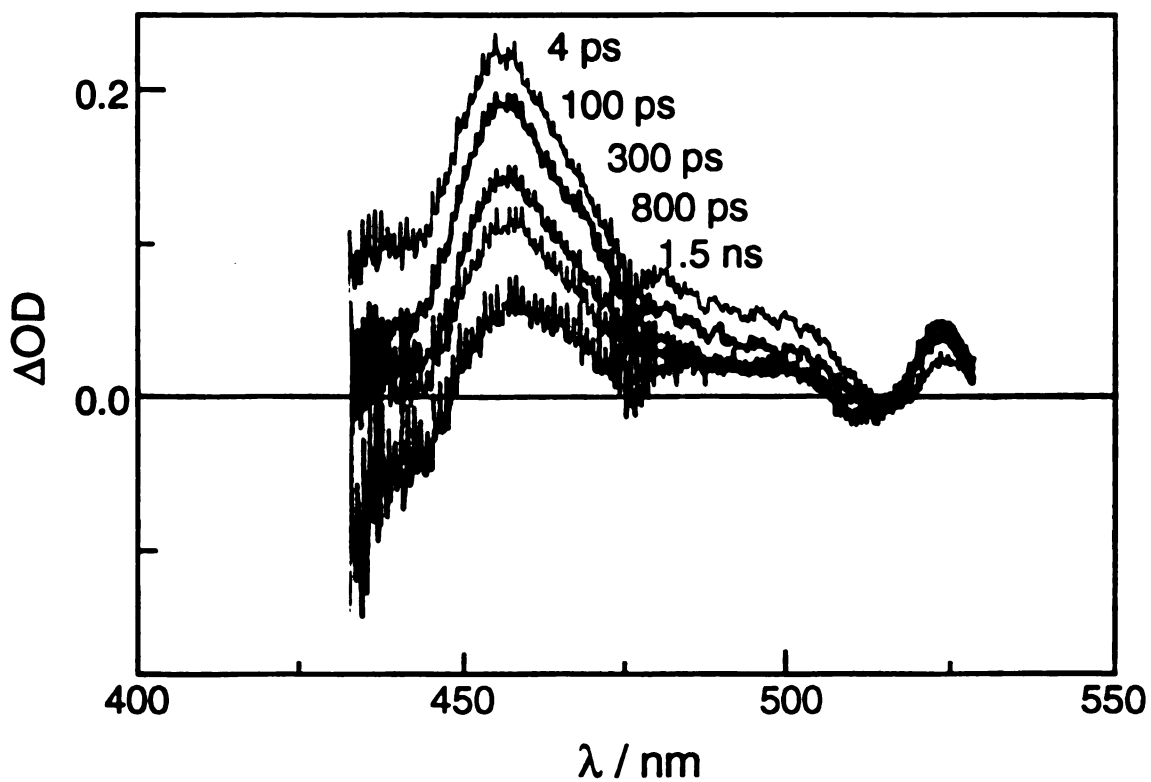


Figure 17. Transient absorption spectra at selected delay following the pump pulse of CH_2Cl_2 solutions of $[\text{ZnPCOOH}] = 10^{-3} \text{ M}$ and $[\text{DNTCOOH}] = 10^{-2} \text{ M}$ after subtraction of $^1\pi\pi^*$ signal.

The spectral profiles obtained by the subtraction of a fraction of the ZnPCOOH spectrum (0.7) from those obtained in the presence of AQCOOH are shown in Figure 18 (system 3–H). The multiplication constant is larger in this case because the acceptor concentration was smaller due to solubility problems; thus more unbound ZnPCOOH is expected to be present in solution. For this reason a concentration dependence was not followed and the exact concentration of quencher is unknown, although is likely to be in the 10^{-3} to 10^{-2} M range. However, qualitatively two distinct absorption features are observed, one at 460 nm due to the ZnPCOOH⁺ and the other with maximum at 490 nm, which is typical of reduced quinones.¹⁰⁸ The decay profile ($-\ln(\Delta OD_{460})$ vs time) of the unsubtracted spectra at 485 nm is shown in Figure 19, where two decays of 22 and 465 ps are observed.

No charge transfer was observed in 2–D, even at high concentrations. Spectra of solutions containing $[DNTCOOD] = 5 \times 10^{-2}$ M, obtained 20 ps and 2 ns after the pump pulse, show no absorption due to the ZnPCOOD⁺, and only the $^1\pi\pi^*$ and $^3\pi\pi^*$ spectral profiles are evident from these data (Figure 20). This observation is puzzling, since it implies that either the donor and acceptor are not binding or that the binding constants are faster or comparable to the forward ET rate. If one assumes the previously determined deuterium isotope effect of 1.7 and utilizes $k_{CS} = 1.2 \times 10^{10} \text{ s}^{-1}$ for the protiated pair, then in the deuterated system k_{CS} would be expected to be $7 \times 10^9 \text{ s}^{-1}$. If the rate constant for the dissociation of the donor/acceptor pair is of the order of $10^{10} \text{ s}^{-1} \text{ M}^{-1}$, then charge separation would be impeded. Alternatively, the system may have a small enough binding constant such that the number of donor/acceptor pairs in solution is not sufficiently high to be detected by transient absorption. To this end, the binding constant must be determined by IR spectroscopy and the static quenching experiment

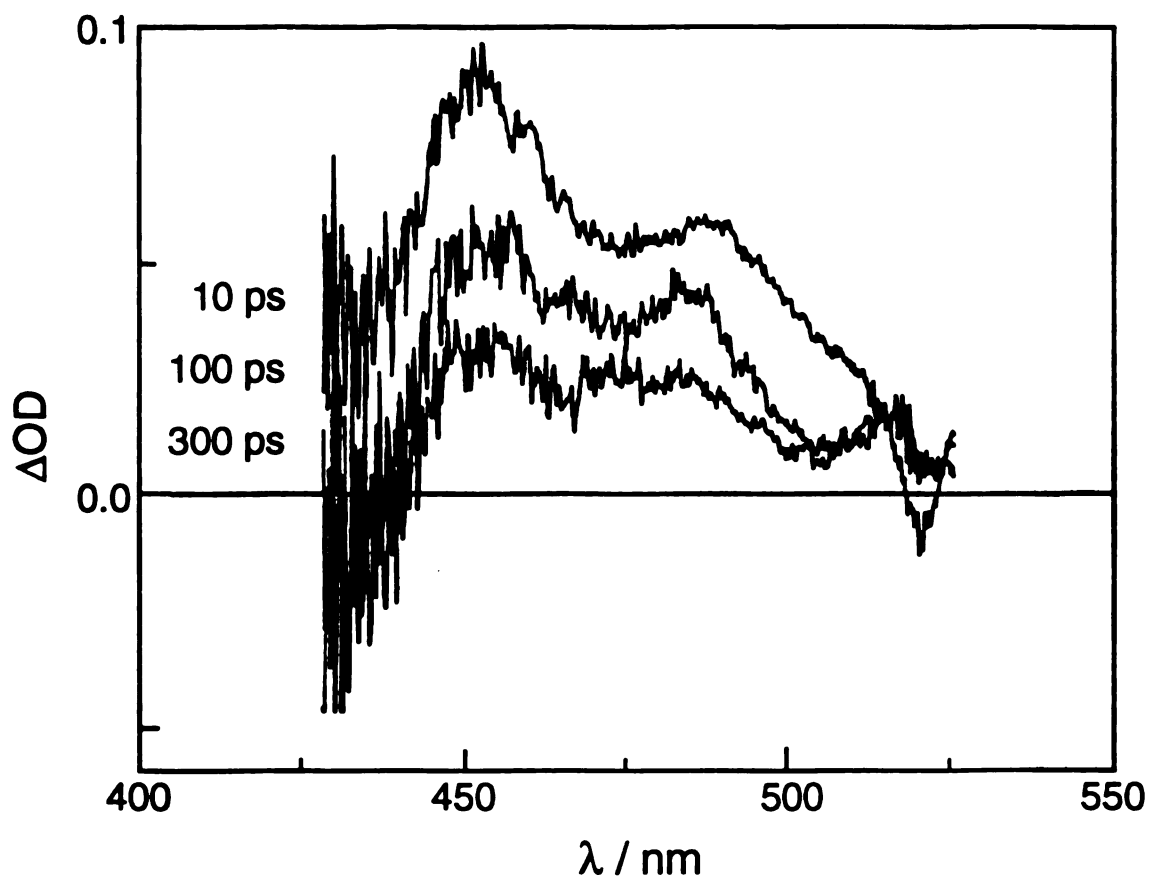


Figure 18. Transient absorption spectra collected at selected delay times after the pump pulse of CH₂Cl₂ solutions containing ZnPCOOH and AQCOOH, after subtraction of ¹ππ* signal.

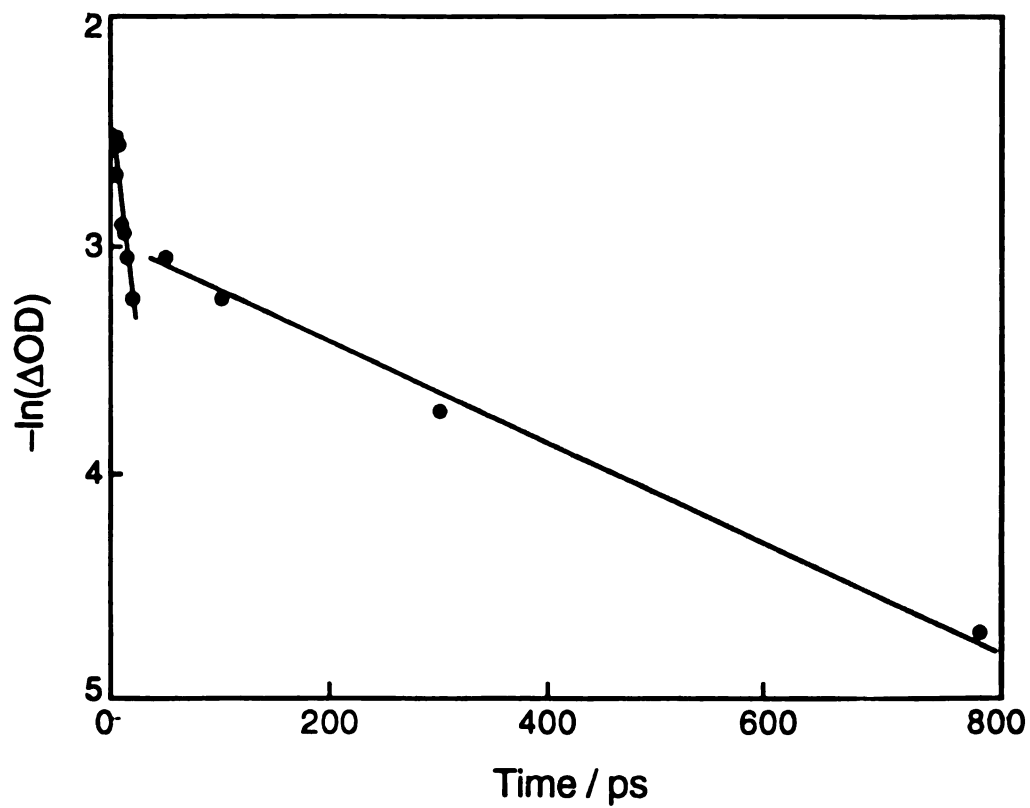


Figure 19. Plot of $-\ln(\Delta OD)$ vs time showing the biphasic decay of the ZnPCOOH/AQCOOH pair.

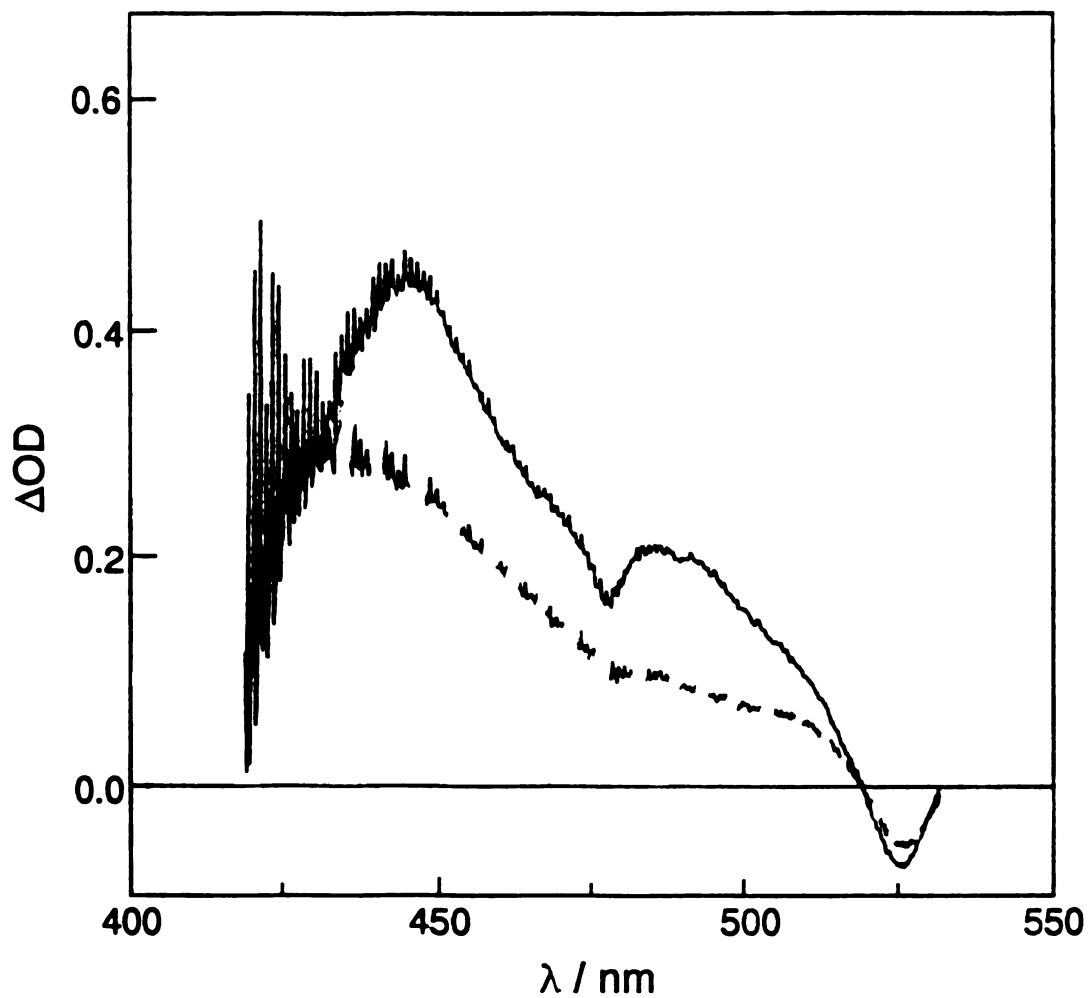


Figure 20. Transient absorption spectra of a CH_2Cl_2 solution containing $[\text{ZnPCOOD}] = 10^{-3} \text{ M}$ and $[\text{DNTCOOH}] = 10^{-2} \text{ M}$ collected 20 ps (—) and 2 ns (---) after the excitation pulse.

should be performed on this system to begin addressing the questions posed by these preliminary results.

3. Comparison of the Three Protiated Systems

Three different protiated acceptors were utilized to form donor/acceptor pairs of type n-H ($n = 1 - 3$). The rates of charge separation, k_{CS} , and charge recombination, k_{CR} , measured for the three systems are listed in Table VII, along with their respective driving forces. Systems 1 and 2 have similar forward and back driving forces; accordingly their forward ET rates are equal. However, the charge recombination rate of 2 is a factor of 4.6 slower than that of 1. It is not yet clear why these rates are so different.

Although the driving forces for 1 – 3 are only approximate (Table VII), speculations stemming from their approximate values can be made. From classical transition state theory the electron transfer rate can be

Table VII. Comparison of charge separation and recombination ET rates for the three acceptors with ZnPCOOH with their respective driving forces.

| Acceptor | $-\Delta G_{CS}$ (eV) ^a | k_{CS} (s ⁻¹) | $-\Delta G_{CR}$ (eV) ^a | k_{CR} (s ⁻¹) |
|----------|------------------------------------|-----------------------------|------------------------------------|-----------------------------|
| DNBCOOH | 0.7 | 5.0×10^{10} | 1.4 | 1.0×10^{10} |
| AQCOOH | 0.7 | 5.0×10^{10} | 1.4 | 2.1×10^9 |
| DNTCOOH | 0.5 | 1.2×10^{10} | 1.6 | 3.6×10^8 |

^aThe values of ΔG were calculated from the reduction potentials listed in Table I.

expressed as¹⁰⁹

$$k_{\text{et}} = A |V_0 \exp(-\beta(d-d_0))|^2 \exp\left\{\frac{-(\Delta G + \lambda)^2}{4\lambda k_B T}\right\} \quad (7)$$

where A is a pre-exponential factor, d and d_0 the edge-to-edge distance between donor and acceptor and the closest distance, respectively, β is the damping factor which determines the decay of the electronic coupling with distance, ΔG is the driving force, λ the reorganization energy (assumed to be 1 V), k_B is Boltzmann's constant, and T is the temperature (298 K). From to eq 7, the charge separation in **3-H** should be approximately four times slower than those in **1-H** and **2-H**, whereas the charge recombination is expected to be attenuated by a factor of ~ 6 . The value of k_{CS} is in agreement with this prediction. This relation for the charge recombination rate of **3-H** is in agreement with that for **2-H**, where a six-fold attenuation on the $2.15 \times 10^9 \text{ s}^{-1}$ value for k_{CR} is $3.58 \times 10^8 \text{ s}^{-1}$, in excellent agreement with the value obtained experimentally. These values, however are not in agreement with the charge recombination rate measured for **1-H**.

One possibility is proton abstraction in the reduced DNTCOOH. It has been shown that nitrobenzenes reduced by one electron readily abstract protons from neighboring methyl or methylene groups.¹¹⁰ In cases where this abstraction takes place following laser excitation, the system returns to the ground state with a lifetime of $\sim 1 \text{ ns}$.^{111,112} From our observed charge recombination rate, $k_{\text{CR}} = 3.6 \times 10^8 \text{ s}^{-1}$, it is not unreasonable to postulate that proton abstraction governs the back electron transfer rate. However, this explanation does not address the slow charge recombination rate observed in **2-H**, where AQCOOH is the acceptor.

Comparison of the ET rates through hydrogen bonds with those reported for porphyrin/quinone systems at similar donor/acceptor separation reveals that the proton interface attenuates the rate by approximately one order of magnitude.¹¹³ These results are in agreement with recent calculations, which predict that the electronic coupling through one hydrogen bond corresponds to three covalently-bonded atoms.¹¹⁴

Our data show that although electron transfer is not as efficient as through covalent bonds, hydrogen bonded pathways for ET may play prominent roles where covalently-bound alternatives are very long or absent. Utilizing eq 7 for the ET rates in 1-H and in Wasielewski's systems,¹¹³ where through-bond $\beta = 0.84$ and A is constant in both cases,¹¹⁴ one obtains a value of $\beta = 1.0 - 1.2$ for the ET through our hydrogen-bonded interface. This value of the damping factor is not unreasonable, since in proteins, where hydrogen bonds are prominent, β ranges from 1 to 2.^{12,115}

D. REFERENCES

1. Stryer, L. *Biochemistry* 3rd Ed.; W. H. Freeman and Co: New York, 1988.
2. Zubay, G. *Biochemistry* 2nd Ed.; MacMillan Publishing Company: New York, 1988.
3. Williams, R. J. P. *Nature* **1989**, *338*, 709.
4. Wikström, M.; Krab, K.; Saraste, M. In *Cytochrome Oxidase: A Synthesis*; Academic Press: New York, 1981.
5. Williams, R. J. P. In *Electron Transfer in Biology and the Solid State*; Johnson, M. K.; King, R. B.; Kutz, D. M., Jr.; Kutal, C.; Norton, M. L;

- Scott, R. A., Eds.; *Advances in Chemistry Series 226*; American Chemical Society: Washington DC; 1990, pp 3-26.
6. Scott, R. A. *Annu. Rev. Biophys. Chem.* **1989**, *18*, 137.
 7. Naqui, A.; Chance. B.; Cardenas, E. *Annu. Rev. Biochem.* **1986**, *55*, 137.
 8. Chan, S. I.; Li, P. M. *Biochemistry* **1990**, *29*, 1.
 9. Malmström, B. G. *Chim. Scripta* **1987**, *27B*, 67.
 10. Capaldi, R. A. *Chemica Scripta* **1987**, *27B*, 39.
 11. (a) Beratan, D. N.; Betts, J. N.; Onuchic, J. N. *Science* **1991**, *252*, 1285.
(b) Betts, J. N.; Beratan, D. N.; Onuchic, J. N. *J. Am. Chem. Soc.* **1992**, *114*, 4043.
 12. Wuttke, D. S.; Bjerrum, M. J.; Winkler, J. R.; Gray, H. B. *Science* **1992**, *256*, 1007.
 13. Therien, M. J.; Selman, M.; Gray, H. B.; Chang, I-J.; Winkler, J. R. *J. Am. Chem. Soc.* **1990**, *112*, 2420.
 14. Hille, R. *Biochemistry* **1991**, *30*, 8522.
 15. Ali, S. N.; Zeller, H.-D.; Calisto, M. K.; Jorns, M. S. *Biochemistry* **1991**, *30*, 10980.
 16. Hansson, Ö.; Wydrzynski, T. *Photosynth. Res.* **1990**, *23*, 131.
 17. *Topics in Photosynthesis: The Photosystems*; Barber, J., Ed.; Elsevier: Amsterdam, 1991.
 18. (a) Deisenhofer, J.; Epp, O.; Miki, K.; Huber, R.; Michel, H. *J. Mol. Biol.* **1984**, *180*, 385. (b) Deisenhofer, J.; Epp, O.; Miki, K.; Huber, R.; Michel, H. *Nature (London)* **1985**, *318*, 618. (c) Allen, J. P.; Feher, G.; Yeates, T. O.; Rees, D.; Deisenhofer, H.; Huber, R. *Proc. Natl. Acad. Sci. U.S.A.* **1986**, *83*, 8593.

19. (a) Chang, C.-H.; Tiede, D.; Tang, J.; Smith, U.; Norris, J.; Schiffer, M. *J. Mol. Biol.* **1985**, *186*, 201. (b) El-Kabbani, O.; Chang, C.-H.; Tiede, D.; Norris, J.; Schiffer, M. *Biochemistry* **1991**, *30*, 5361.
20. (a) Fleming, G. R.; Martin, J.-L.; Breton, J. *Nature (London)* **1988**, *333*, 190. (b) Breton, J.; Martin, J.-L.; Fleming, G. R.; Lambry, J. C. *Biochemistry* **1988**, *27*, 8276.
21. (a) Kirmaier, C.; Holten, D. *FEBS Lett.* **1988**, *239*, 211. (b) Kirmaier, C.; Holten, D. *Proc. Natl. Acad. Sci. U.S.A.* **1990**, *87*, 3552.
22. (a) Holzapfel, W.; Finkle, U.; Kaiser, W.; Oesterhelt, D.; Scheer, H.; Stilz, H. U.; Zinth, W. *Chem. Phys. Lett.* **1989**, *160*, 1. (b) Dressler, K.; Finkle, U.; Lauterwasser, C.; Hamm, P.; Holzapfel, W.; Buchanan, S.; Kaiser, W.; Michel, H.; Oesterhelt, D.; Scheer, H.; Stilz, H. U.; Zinth, W. In *Structure and Function of Bacterial Reaction Centers*; Michel-Beyerle, M. E., Ed.; Springer-Verlag: Berlin, 1990; pp 135-140.
23. Woodbury, N. W.; Becker, M.; Middendorf, D.; Parson, W. W. *Biochemistry* **1985**, *24*, 7516.
24. Carithers, R. P.; Parson, W. W. *Biochim. Biophys. Acta* **1975**, *387*, 194.
25. Vermeglio, A.; Clayton, R. K. *Biochim. Biophys. Acta* **1977**, *461*, 159.
26. Vincent, J. B.; Christou, G. *Adv. Inorg. Chem.* **1989**, *33*, 197.
27. Brudvig, G. W.; Crabtree, R. H. *Prog. Inorg. Chem.* **1989**, *37*, 99.
28. Chan, M. K.; Armstrong, W. H. *J. Am. Chem. Soc.* **1990**, *112*, 4985.
29. Paddock, M. L.; Rongey, S. H.; Feher, G.; Okamura, M. Y. *Proc. Natl. Acad. Sci. U.S.A.* **1989**, *86*, 6602.
30. Takahashi, E.; Wraight, C. A. *Biochim. Biophys. Acta* **1990**, *1020*, 107.
31. Takahashi, E.; Wraight, C. A. *Biochemistry* **1992**, *31*, 855.
32. Paddock, M. L.; McPherson, P. H.; Feher, G.; Okamura, M. Y. *Proc. Natl. Acad. Sci. U.S.A.* **1990**, *87*, 6803.

33. Buchanan, S.; Michel, H.; Gerwert, K. *Biochemistry* **1992**, *31*, 1314.
34. Wikström, M.; Krab, K.; Saraste, M. In *Cytochrome Oxidase: A Synthesis*; Academic Press: New York, 1981.
35. Williams, R. J. P. In *Electron Transfer in Biology and the Solid State*; Johnson, M. K.; King, R. B.; Kutz, D. M., Jr.; Kotal, C.; Norton, M. L.; Scott, R. A., Eds.; Advances in Chemistry Series 226; American Chemical Society: Washington DC, 1990; pp 3-26.
36. Scott, R. A. *Annu. Rev. Biophys. Chem.* **1989**, *18*, 137.
37. Naqui, A.; Chance, B.; Cardenas, E. *Annu. Rev. Biochem.* **1986**, *55*, 137.
38. Chan, S. I.; Li, P. M. *Biochemistry* **1990**, *29*, 1.
39. Pan, L.-P.; Hazzard, J. T.; Lin, J.; Tollin, G.; Chan, S. I. *J. Am. Chem. Soc.* **1991**, *113*, 5908.
40. Hill, B. C. *J. Biol. Chem.* **1991**, *266*, 2219.
41. Morgan, J. E.; Wikström, M. *Biochemistry* **1991**, *30*, 948.
42. Oliveberg, M.; Malmström, B. G. *Biochemistry* **1991**, *30*, 7053.
43. Morgan, J. E.; Li, P. J.; Jang, D.-J.; El-Sayed, M. A.; Chan, S. I. *Biochemistry* **1989**, *28*, 6975.
44. Brzezinski, P.; Malmström, B. G. *Biochim. Biophys. Acta* **1987**, *894*, 29.
45. Boelens, R.; Wever, R.; Van Gelder, B. F. *Biochim. Biophys. Acta* **1982**, *682*, 264.
46. (a) Wikström, M. *Chemica Scripta* **1987**, *27B*, 53. (b) Wikström, M. *Nature* **1989**, *338*, 776.
47. Malmström, B. G. *Chim. Scripta* **1987**, *27B*, 67.
48. Williams, R. J. P. *Nature* **1989**, *338*, 709.

49. (a) Malmström, B. G. *Chem. Rev.* **1990**, *90*, 1247. (b) Malmström, B. G. *Arch. Biochem. Biophys.* **1990**, *280*, 233.
50. (a) Wasielewski, M. R.; Johnson, D. G.; Svec, W. A.; Kersey, K. M.; Minsek, D. W. *J. Am. Chem. Soc.* **1988**, *110*, 7219. (b) Wasielewski, M. R.; Johnson, D. G.; Niemczyk, M. P.; Gaines, III, G. L.; O'Neil, M. P.; Svec, W. A. *J. Am. Chem. Soc.* **1990**, *112*, 6482. (c) Gaines, III, G. L.; O'Neil, M. P.; Svec, W. A.; Niemczyk, M. P.; Wasielewski, M. R. *J. Am. Chem. Soc.* **1991**, *113*, 719.
51. (a) Bilsel, O.; Rodriguez, J.; Holten, D.; Girolami, G. S.; Milam, S. N.; Suslick, K. S. *J. Am. Chem. Soc.* **1990**, *112*, 4075. (b) Knapp, S.; Dhar, T. G. M.; Albaneze, J.; Gentemann, S.; Potenza, J. A.; Holten, D.; Schugar, H. J. *J. Am. Chem. Soc.* **1991**, *113*, 4010. (c) Rodriguez, J.; Kirmaier, C.; Johnson, M. R.; Friesner, R. A.; Holten, D.; Sessler, J. L. *J. Am. Chem. Soc.* **1991**, *113*, 1652.
52. (a) Heiler, D.; McLendon, G.; Rogalskyj, P. *J. Am. Chem. Soc.* **1987**, *109*, 604. (b) Helms, A.; Heiler, D.; McLendon, G. *J. Am. Chem. Soc.* **1991**, *113*, 4325.
53. (a) Closs, G. L.; Calcaterra, L. T.; Green, N. J.; Penfield, K. W.; Miller, J. R. *J. Phys. Chem.* **1986**, *90*, 3673. (b) Closs, G. L.; Miller, J. R. *Science (Washington, DC)* **1988**, *240*, 440. (c) Closs, G. L.; Johnson, M. D.; Miller, J. R.; Piotrowiak, P. *J. Am. Chem. Soc.* **1989**, *111*, 3551.
54. (a) Siemiarczuk, A.; McIntosh, A. R.; Ho, T.-F.; Stillman, M. J.; Roach, K. J.; Weedon, A. C.; Bolton, J. R.; Connolly, J. S. *J. Am. Chem. Soc.* **1983**, *105*, 7224. (b) Schmidt, J. A.; McIntosh, A. R.; Weedon, A. C.; Bolton, J. R.; Connolly, J. S.; Hurley, J. K.; Wasielewski, M. R. *J. Am. Chem. Soc.* **1988**, *110*, 1733.

55. Leland, B. A.; Joran, A. D.; Felker, P. M.; Hopfield, J. J.; Zewail, A. H.; Dervan, P. B. *J. Phys. Chem.* **1985**, *89*, 5571.
56. (a) Harrison, R. J.; Pearce, B.; Beddard, G. S.; Cowan, J. A.; Sanders, J. K. M. *Chem. Phys.* **1987**, *116*, 429. (b) Hunter, C. A.; Meah, M. N.; Sanders, J. K. M. *J. Am. Chem. Soc.* **1990**, *112*, 5773.
57. (a) Batteas, J. D.; Harriman, A.; Kanda, Y.; Mataga, N.; Nowak, A. K. *J. Am. Chem. Soc.* **1990**, *112*, 126. (b) Osuka, A.; Maruyama, K.; Mataga, N.; Asahi, T.; Yamazaki, I.; Tamai, N. *J. Am. Chem. Soc.* **1990**, *112*, 4958.
58. Hermant, R. M.; Bakker, N. A. C.; Scherer, T.; Krijnen, B.; Verhoeven, J. W. *J. Am. Chem. Soc.* **1990**, *112*, 1214. (b) Antolovich, M.; Keyte, P. J.; Oliver, A. M.; Paddon-Row, M. N.; Kroon, J.; Verhoever, J. W.; Jonker, S. S.; Warman, J. M. *J. Phys. Chem.* **1991**, *95*, 1933.
59. Gust, D.; Moore, T. A. *Science (Washington, DC)* **1989**, *244*, 35. (b) Gust, D.; Moore, T. A.; Moore, A. L.; Gao, F.; Luttrull, D.; DeGraziano, J. J.; Ma, X. C.; Makings, L. R.; Lee, S.-J.; Trier, T. T.; Bittersman, E.; Seely, G. R.; Woodward, S.; Bensasson, R. V.; Rougee, M.; De Schryver, F. C.; Van der Auweraer, M. *J. Am. Chem. Soc.* **1991**, *113*, 3638.
60. Meyer, T. J. *Acc. Chem. Res.* **1989**, *22*, 164.
61. Perkins, T. A.; Humer, W.; Netzel, T. L.; Schanze, K. S. *J. Phys. Chem.* **1990**, *94*, 2229.
62. Vassilian, A.; Wishart, J. F.; van Hemelryck, B.; Schwarz, H.; Idied, S. *J. Am. Chem. Soc.* **1990**, *112*, 7278.
63. Chang, I.-J.; Gray, H. B.; Winkler, J. R. *J. Am. Chem. Soc.* **1991**, *113*, 7056.

64. (a) McLendon, G. *Acc. Chem. Res.* **1988**, *21*, 160. (b) Conklin, K. T.; McLendon, G. *J. Am. Chem. Soc.* **1988**, *110*, 3345.
65. (a) Wallin, S. A.; Stemp, E. D. A.; Everest, A. M.; Nocek, J. M.; Netzel, T. L.; Hoffman, B. M. *J. Am. Chem. Soc.* **1991**, *113*, 1842. (b) Kuila, D.; Baxter, W. W.; Natan, M. J.; Hoffman, B. M. *J. Phys. Chem.* **1991**, *95*, 1. (c) Nocek, J. M.; Stemp, E. D. A.; Finnegan, M. G.; Koshy, T. I.; Johnson, M. K.; Margoliash, E.; Mauk, A. G.; Smith, M.; Hoffman, B. M. *J. Am. Chem. Soc.* **1991**, *113*, 6822.
66. Dixon, D. W.; Hong, X.; Woehler, S. E.; Mauk, A. G.; Sishta, B. P. *J. Am. Chem. Soc.* **1990**, *112*, 1082.
67. Concar, D. W.; Whitford, D.; Pielak, G. J.; Williams, R. J. P. *J. Am. Chem. Soc.* **1991**, *113*, 2401.
68. Sigel, H.; Sigel, A., Eds. *Metals in Biological Systems*; Marcel Dekker: New York, 1991; Vol. 27.
69. Johnson, M. K.; King, R. B.; Kurtz, D. M.; Kutal, C.; Norton, M. L.; Scott, R. A., Eds.; *Electron Transfer in Biology and the Solid State*; American Chemical Society: Washington, DC, 1990; Vol. 226, Section 2.
70. De Felippis, M. R.; Faraggi, M.; Kapper, M. H. *J. Am. Chem. Soc.* **1990**, *112*, 5640.
71. (a) Barbara, P. F.; Jarzeka, W. *Acc. Chem. Res.* **1988**, *21*, 195. (b) Smith, T. P.; Zaklika, K. A.; Takur, K.; Barbara, P. F. *J. Am. Chem. Soc.* **1991**, *113*, 4035.
72. Swinney, T. C.; Kelley, D. F. *J. Phys. Chem.* **1991**, *95*, 2430.
73. Held, A.; Plusquellic, D. F.; Tomer, J. L.; Pratt, D. W. *J. Phys. Chem.* **1991**, *95*, 2877.

74. (a) Millikan, R. C.; Pitzer, K. S. *J. Am. Chem. Soc.* **1958**, *80*, 3515. (b) Davis, Jr., J. C.; Pitzer, K. S. *J. Phys. Chem.* **1960**, *64*, 886.
75. Chang, T.-T.; Yamaguchi, Y.; Miller, W. H.; Schaefer, III, H. F. *J. Am. Chem. Soc.* **1987**, *109*, 7245.
76. Wenograd, J.; Spur, R. A. *J. Am. Chem. Soc.* **1957**, *79*, 5844.
77. Kalyasundaram, K.; Newman-Spallart, M. *J. Phys. Chem.* **1982**, *86*, 5163.
78. Clark, W. M. *Oxidation-Reduction Potentials of Organic Systems*; Krieger: Huntington, N.Y.; 1972.
79. Neta, P.; Simic, M. G.; Hoffman, M. Z. *J. Phys. Chem.* **1976**, *80*, 2018.
80. Kazakova, V. M.; Minina, N. E.; Piskov, V. B. *Zh. Obs. Khim.* **1982**, *52*, 836.
81. Mann, C. K.; Barnes, K. K. *Electrochemical Reactions in Non-Aqueous Systems*; Marcel Dekker: New York, 1970
82. This porphyrin was synthesized from condensation of 5,5'-dibromo-3,3'-diethyl-4,4'-dimethyl-2,2'-dipyrrylmethene hydrobromide and 4-carboxymethyl-3,3',4',5,5'-pentamethyl-2,2'-dipyrrylmethene hydrobromide in formic acid.
83. Marty Raab, the MSU Chemistry Department electronic designer, modified the electronics to allow the device to operate at cavity dumper rates slower than 8 MHz.
84. *Ultrafast Light Pulses*; Shapiro, S. L., Ed.; Springer-Verlag: Berlin; 1977.
85. Skoog, D. A. *Principles of Instrumental Analysis* 3rd Ed.; Saunders College: Philadelphia, 1985.
86. Declémy, A.; Rullière, C. *Rev. Sci. Instrum.* **1986**, *57*, 2733.
87. Mussel, R. D.; Nocera, D. G. *J. Am. Chem. Soc.* **1986**, *110*, 2764.

88. Joensten, M. D.; Schaad, L. J. *Hydrogen Bonding*; Marcel Dekker: New York, 1974.
89. Tucker, E. E.; Lippert, E. In *The Hydrogen Bond*; Schuster, P; Zundel, G.; Sandorfy, C., Eds.; North-Holland Pub. Co.: New York, 1976.
90. Huggins, C. M.; Pimentel, G. C.; Shoolery, J. N. *J. Phys. Chem.* **1956**, *60*, 1311.
91. Davis, Jr., J. C.; Pitzer, K. S. *J. Phys. Chem.* **1960**, *64*, 886.
92. Muller, N.; Hughes, O. R. *J. Phys. Chem.* **1966**, *70*, 3975.
93. Murthy, A. S. N.; Rao, C. N. R. *Appl. Spectros. Rev.* **1968**, *2*, 69.
94. Bellamy, L. J. *The Infrared Spectra of Complex Molecules*; Wiley: New York, 1975.
95. Affsprung, H. E.; Christian, S. D.; Melnick, A. M. *Spectrochim. Acta* **1963**, *20*, 285
96. Balzani, V.; Moggi, L.; Manfrin, M. F.; Bolletta, F. *Coord. Chem. Rev.* **1975**, *15*, 321.
97. The ratio of I_0/I , where I_0 and I represent the integrated emission intensities in the absence and presence of a known quencher concentration, respectively, was utilized to calculate the number of ZnPCOOH molecules bound to DNBCOOH.
98. The nanosecond transient absorption instrument has been previously described (Jackson, J. A.; Turró, C.; Newsham, M. D.; Nocera, D. G. *J. Phys. Chem.* **1990**, *94*, 4500) and is explained in more detail in Chapter II.B.
99. Webster, O. W.; Mahler, W.; Benson, R. E. *J. Am. Chem. Soc.* **1962**, *84*, 3678.
100. Nosaka, Y.; Kuwabara, A.; Miyama, H. *J. Phys. Chem.* **1986**, *90*, 1465.

101. Fajer, J.; Borg, D. C.; Forman, A.; Dolphin, D.; Felton, R. H. *J. Am. Chem. Soc.* **1970**, *92*, 3451.
102. Oertling, W. A.; Salehi, A.; Chung, Y. C.; Leroi, G. E.; Chang, C. K.; Babcock, G. T. *J. Phys. Chem.* **1987**, *91*, 5887.
103. Rodriguez, J.; Kirmaier, C.; Holten, D. *J. Am. Chem. Soc.* **1989**, *111*, 6500.
104. $\lambda_{\text{exc}} = 575$ nm, FWHM = 5 ps, $\lambda_{\text{em}} = 630$ nm; instrument described in detail by Lawrence E. Bowman, Ph.D. Dissertation, Michigan State University, 1991.
105. A larger range of concentrations could not be probed owing to the low signal intensities and insufficient solubility at low and higher concentrations, respectively.
106. Because of synthetic inavailability, ethyl-3,5-dinitrobenzoate was utilized instead of the 3,4-substitued analog.
107. Neta, P.; Huie, R. E.; Maruthamuthu, P.; Steenken, S. *J. Phys. Chem.* **1989**, *93*, 7654.
108. Umemoto, K. *Chem. Lett.* **1985**, 1415.
109. (a) Marcus, R. A. *J. Chem. Phys.* **1956**, *24*, 966. (b) Marcus, R. A. *Ann. Rev. Phys. Chem.* **1964**, *15*, 155.
110. Fine, D. A.; Miles, M. H. *Anal. Chim. Acta* **1983**, *153*, 141.
111. McClelland, R. A.; Steenken, S. *Can. J. Chem.* **1987**, *65*, 353.
112. Gravel, D.; Giasson, R.; Blanchet, D.; Yip, R. W.; Sharma, D. K. *Can. J. Chem.* **1991**, *69*, 1193.
113. Wasielewski, M. R.; Niemczyk, M. P.; Svec, W. A.; Pewitt, E. B. *J. Am. Chem. Soc.* **1985**, *107*, 1080.
114. Beratan, D. N.; Betts, J. N.; Onuchic, J. N. *Science* **1991**, *252*, 1285.
115. Winkler, J. R.; Gray, H. B. *Chem. Rev.* **1992**, *92*, 369.

CHAPTER II

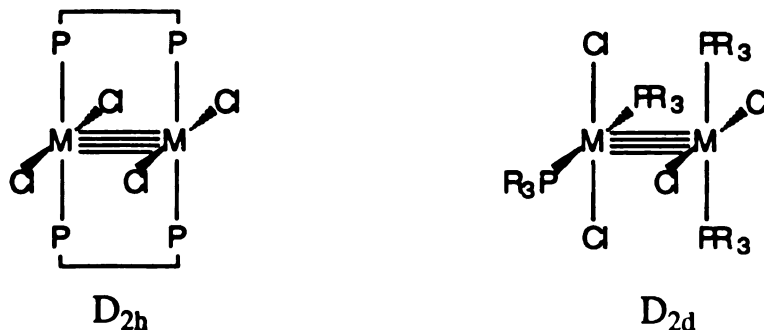
TRANSIENT ABSORPTION SPECTROSCOPY OF Mo AND W QUADRUPLY-BONDED DIMERS

A. BACKGROUND

Multielectron transformations are at the essence of energy conversion and storage schemes. Their importance in biology is manifested in the catalytic reduction of oxygen in respiration and the oxidation of water in photosynthesis.¹⁻¹³ A crucial issue in the mechanism of multielectron reactions has been the determination of whether they proceed via two consecutive one-electron transfers or one concerted two-electron step.¹⁴⁻¹⁷ Although many reactions were believed to proceed in a concerted manner, as the detection timescales became faster they were shown to be composed of two one-electron steps.¹⁴⁻¹⁷ Early kinetic methods included techniques such as stopped-flow and temperature-jump, which permit measurement of events in the 10^{-4} s and 10^{-6} s regimes, respectively. However, in systems where photons initiate the two-electron reactions, dynamic measurements can be conducted following excitation of the sample by a light pulse of short duration (10^{-8} to 10^{-12} s). The excited states, or intermediates, prepared in this manner should provide an insight into the requirements necessary to

effect photoinduced two-electron transformations. Following the excitation pulse their physical properties, including their electronic absorption spectrum, can be probed in the absence of substrate.

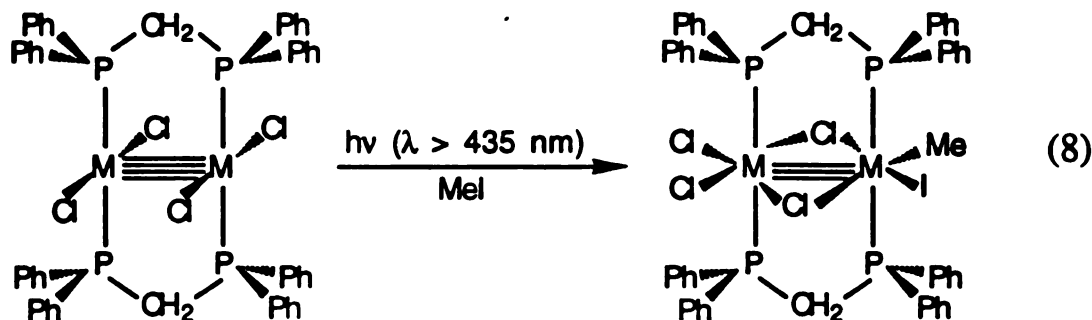
Quadruply-bonded molybdenum complexes, containing a $\text{Mo}^{\text{II}}\text{Mo}^{\text{II}}$ core and four bidentate bridging ligands, are known to undergo two-electron photochemistry to yield an oxidized $\text{Mo}^{\text{III}}\text{Mo}^{\text{III}}$ product.¹⁸⁻²⁰ However, these reactions were shown to proceed via radical mechanisms, rather than a concerted two-electron reaction. It was postulated that the rigid bridging ligands about the metal core precluded addition of the substrate to one of the metals, thus leading to the formation of radicals. To remove this constraint, complexes of the type $\text{M}_2\text{Cl}_4(\overline{\text{P}}\text{P})_2$ and $\text{M}_2\text{Cl}_4(\text{PR}_3)_4$ ($\text{M} = \text{Mo}, \text{W}$; $\overline{\text{P}}\text{P}$ = bidentate phosphines; PR_3 = trialkyl phosphines) were utilized, which contain flexible halides. The two types of complexes have different symmetries, $\text{D}_{2\text{h}}$ and $\text{D}_{2\text{d}}$, as illustrated below,



The $\text{M}_2\text{Cl}_4(\text{PR}_3)_4$ complexes have an eclipsed conformation about metal core to preserve the metal-metal δ bond; however, due to steric effects, each phosphine is eclipsed with a chloride on the adjacent metal, rather than another PR_3 group.

These complexes have been shown to undergo photoinduced two-electron oxidative addition in the presence of methyl iodide (MeI), and

unlike the reactivity observed with the rigid ligands, one electron intermediates outside the solvent cage were not produced.²¹⁻²⁴ The observed reaction of $\text{Mo}_2\text{Cl}_4(\text{dppm})_2$ (dppm = bis(diphenylphosphino)methane) with MeI is shown in eq 8,



which yields an edge-sharing bioctahedral structure with the addition of both Me and I to the same metal center.²³ This feature and the absence of ethane are indicative of the lack of radicals outside the solvent cage. Similar products have been observed in the thermal two-electron addition reactions of quadruply-bonded complexes, which yield products containing bridging ligands, oftentimes halides. A rearrangement of the ligation sphere about the $\text{M}^4\text{-M}$ core in the transition from reactants to products is therefore expected.²⁵

The different reactivity between the flexible and rigid complexes is intriguing since their excited states are similar in nature. A general MO diagram for $\text{M}^4\text{-M}$ complexes is shown in Figure 21, where two ML_4 fragments are brought together to create the metal-metal bonds. The d_{z^2} orbitals form the metal-metal σ bond, while d_{xz} and d_{yz} orbitals give rise to two metal-metal π bonds. The fourth bond is δ in nature, and is formed by the weak interaction of the d_{xy} orbitals on each metal. For two d^4 metals, as is the case with Mo^{II} and W^{II} , the highest occupied molecular orbital (HOMO) is the δ orbital, while the lowest unoccupied molecular orbital

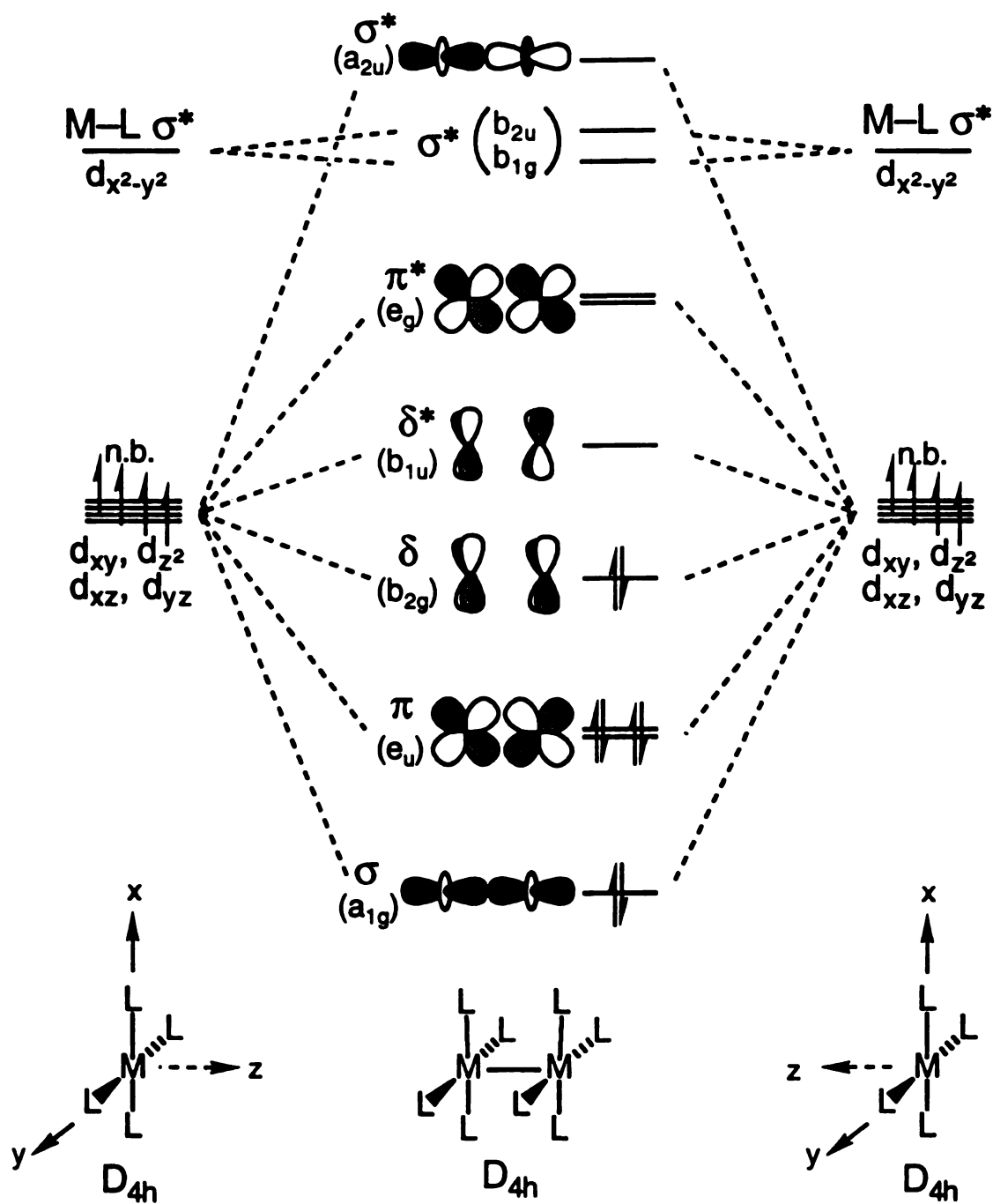


Figure 21. Molecular orbital diagram derived by uniting two d^4 ML_4 fragments to form the bimetallic M_2L_8 quadruply-bonded complex.

(LUMO) is formed from the corresponding antibonding interaction, δ^* . Many spectroscopic studies have been conducted with these molecules and it is well-established that the lowest electronic transition is the dipole allowed $\delta^2 \rightarrow {}^1\delta\delta^*$, as evidenced from inspection of the general MO diagram.²⁶⁻²⁹ Owing to the small overlap of the d_{xy} orbitals valence bond theory provides a better description of the transitions involving the δ and δ^* molecular orbitals, as shown in Figure 22. In the ground ${}^1A_{1g}$ state each electron is localized on the d_{xy} orbital of each metal, whereas in the first allowed excited state, ${}^1A_{2u}$, both electrons reside on the same metal center. In this model the triplet excited state lies just above the ground state rather than near the excited singlet, since electron pairing is necessary in the transition to the ${}^1A_{2u}$ state.

The spectroscopic properties of the D_{2h} and D_{2d} complexes must be understood before transient absorption studies are undertaken. The correlation diagram for the D_{2h} and D_{2d} geometries is shown in Figure 23, where the effect of a C_4 rotation of one ML_2X_2 fragment about the M–M axis on the relative position of the molecular orbitals is followed through the staggered conformation, D_2 .²⁹ The most significant difference between the two MO diagrams is the degeneracy of the π and π^* orbitals in the D_{2d} complex, whereas in the D_{2h} case the degeneracy is lifted. Representative ground state electronic absorption spectra for Mo and W homonuclear dimers are shown in Figure 24 (D_{2h} geometry) and Figure 25 (D_{2d} geometry). The visible transitions in the tungsten complex are red-shifted from those in the molybdenum analog, consistent with their metal-localized origins. The $\delta\delta^*$ transitions in $Mo_2Cl_4(dppm)_2$ and $W_2Cl_2(dppm)_2$ appear at 634 and 710 nm, respectively, and the high energy absorption in the 350 – 400 nm region have been assigned as $\pi \rightarrow \delta^*$ in nature.²⁹ The complete

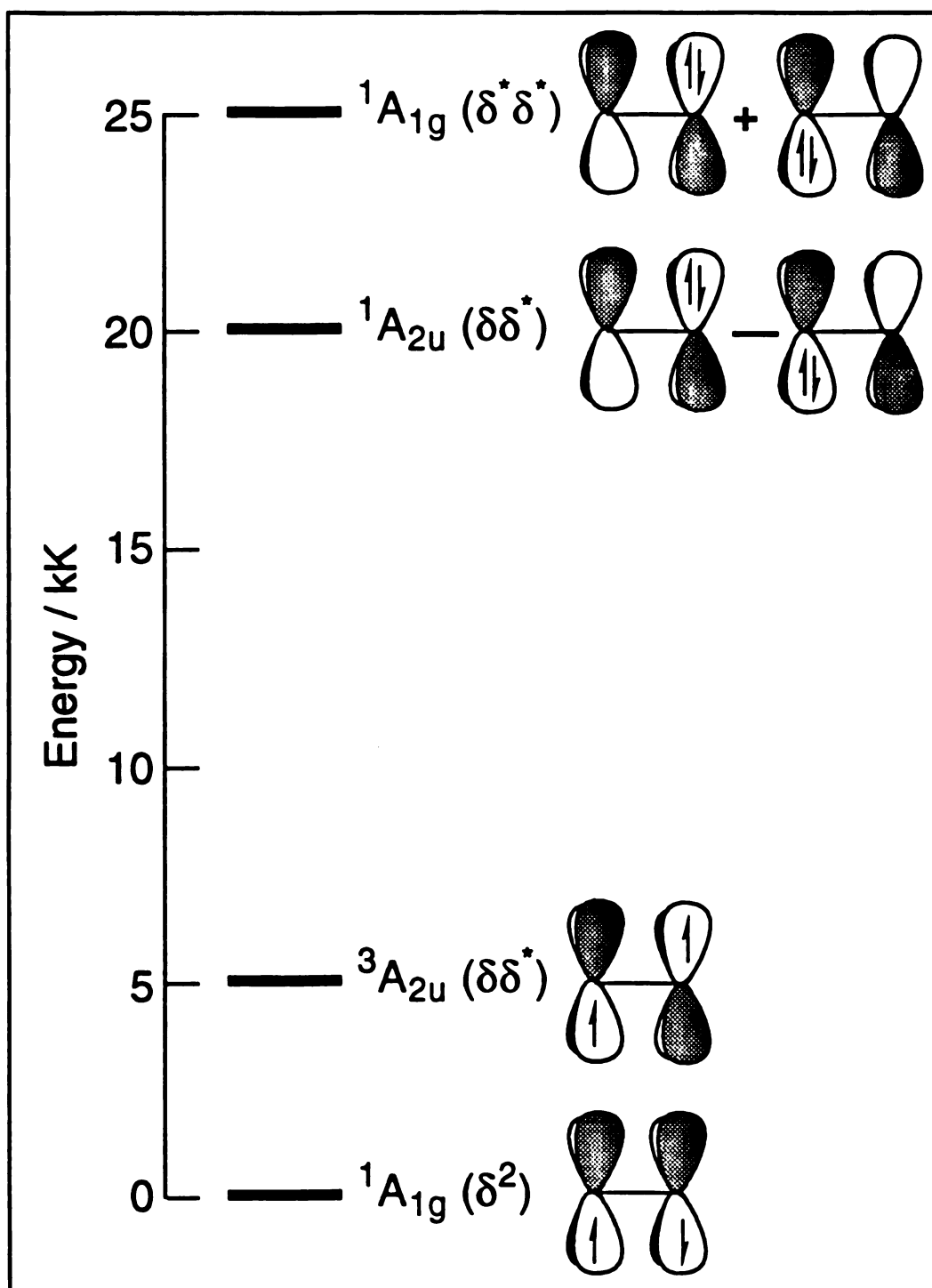


Figure 22. Valence bond description of the electronic states formed by the d_{xy} orbitals, as well as the corresponding MO formalism

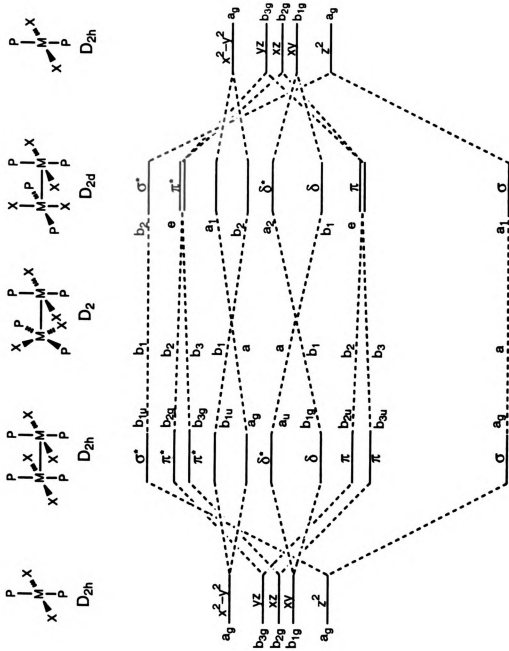


Figure 23. Qualitative MO diagram showing correlation between D_{2h} and D_{2d} geometries.

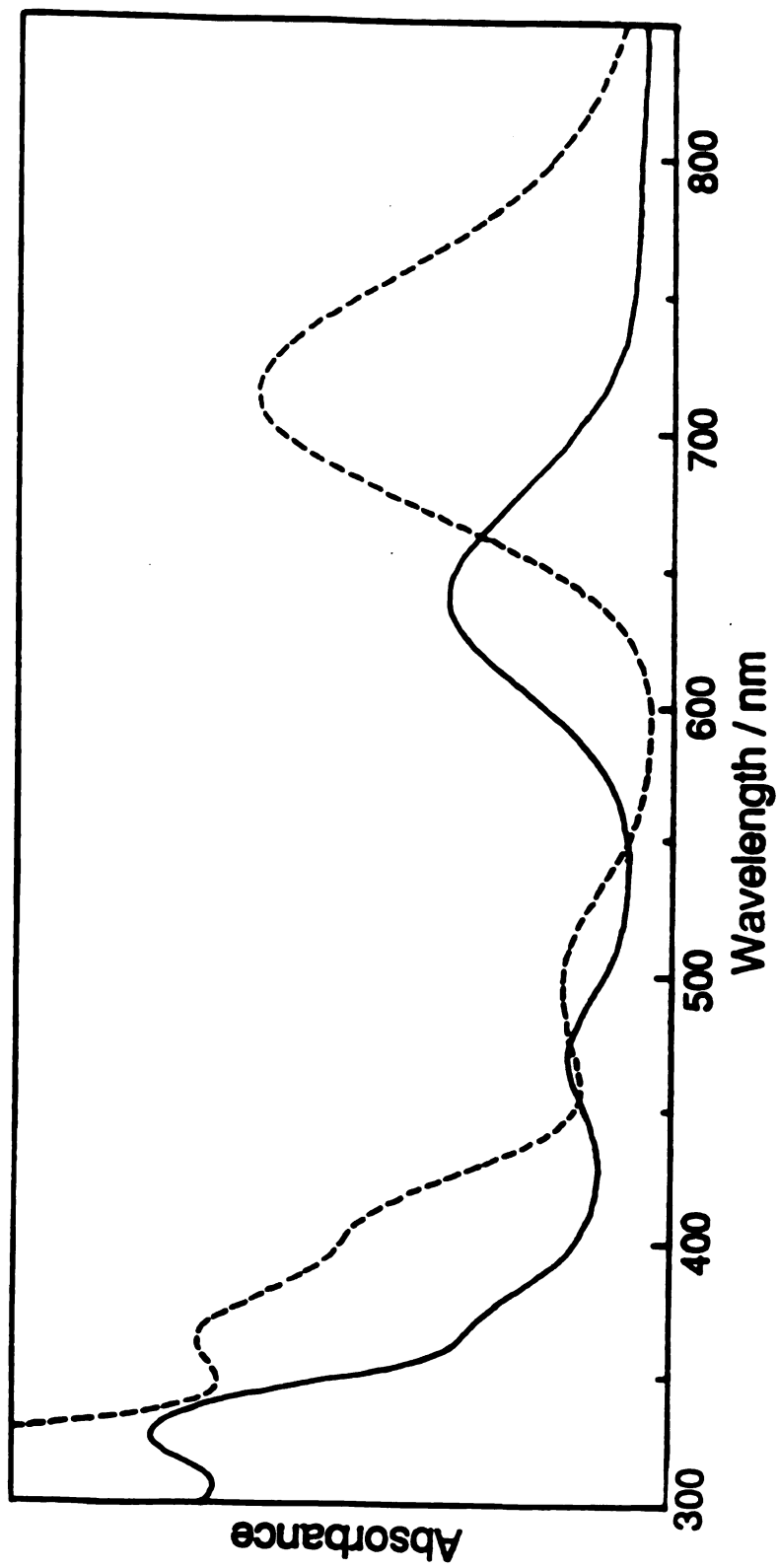


Figure 24. Electronic absorption spectra of (—) $\text{Mo}_2\text{Cl}_4(\text{dppm})_2$ and (---) $\text{W}_2\text{Cl}_4(\text{dppm})_2$ in CH_2Cl_2 .

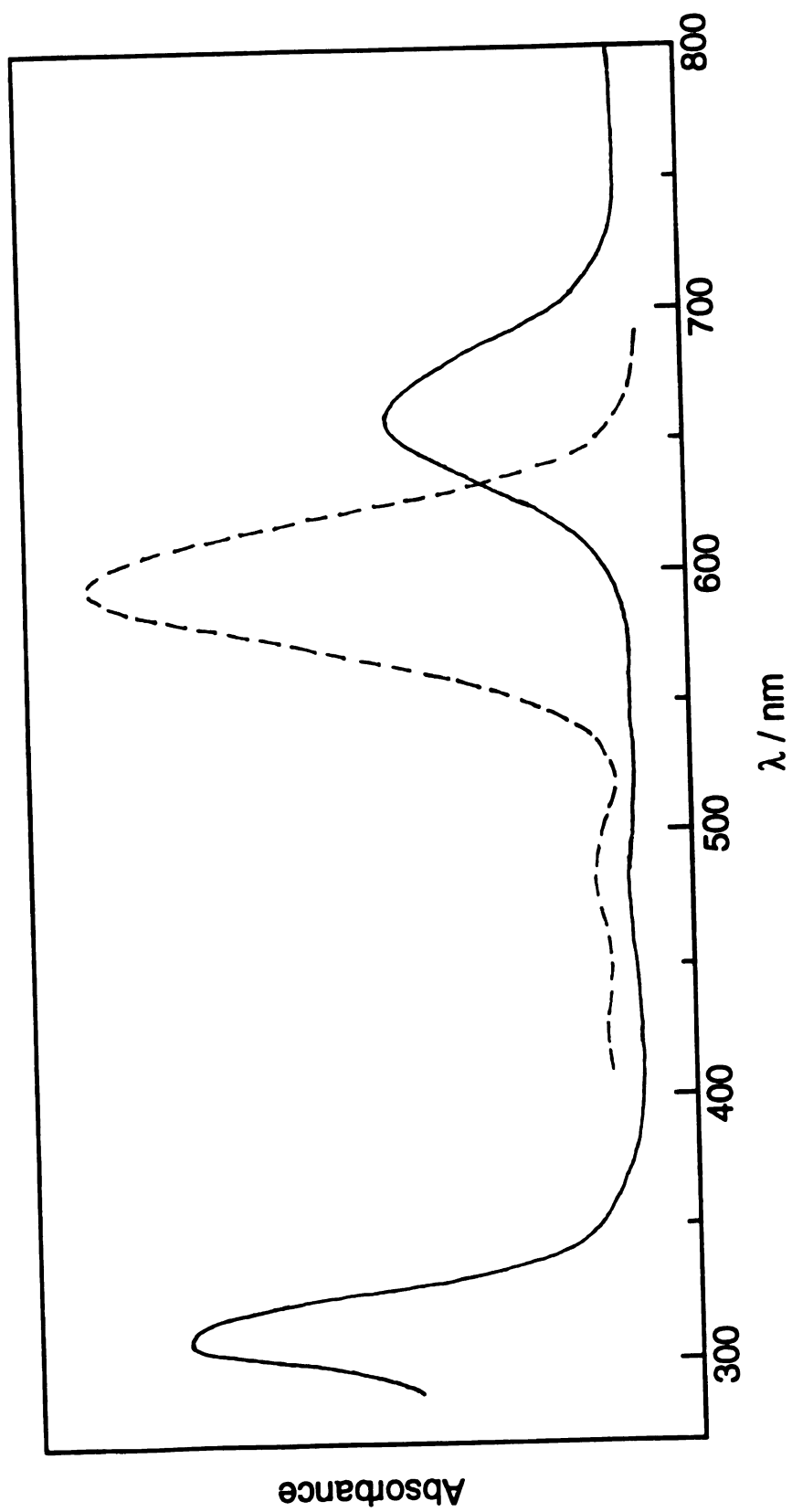


Figure 25. Electronic absorption spectra of (—) $\text{W}_2\text{Cl}_4(\text{PBu}_3)_4$ and (---) $\text{Mo}_2\text{Cl}_4(\text{PBu}_3)_4$ in CH_2Cl_2 .

assignment of the D_{2d} complexes in the visible and ultraviolet regions has been conducted for $M_2X_4(PMe_3)_4$ ($M = Mo, W$; $X = Cl, Br, I$; $PMe_3 =$ trimethylphosphine). In $Mo_2Cl_4(PMe_3)_4$ and $W_2Cl_4(PMe_3)_4$ the $\delta \delta^*$ transitions reach their respective maxima at 584 and 655 nm. The small band at 440 nm in the Mo complex has been assigned to be $\pi \rightarrow \delta^*$, and the strong absorption at 330 nm has been correlated with a $\sigma(MP) \rightarrow \delta^*$ transition.²⁸ A similar assignment has been provided for the tungsten analog for the absorptions at 490 ($\pi \rightarrow \delta^*$) and 296 nm ($\sigma(MP) \rightarrow \delta^*$), where the metal-localized transitions red-shift with respect to those in the molybdenum complex with the concomitant blue-shift of the ligand-to-metal charge transfer (LMCT) band.²⁸

The metal-localized transitions lead to the movement of some electron density from one metal to the other, and can therefore be represented formally by



The ${}^1\delta\delta^*$ excited state possesses a dipole moment of 4.0 D with respect to the non-polar ground state, suggesting a transfer of 0.4 electrons from one metal to the other.³⁰ The two-electron photochemical reactions are believed to stem from the MMCT mixed valence states, where the oxidative addition takes place at the low-valent center to yield the oxidized ${}^{\text{III}}M-M^{\text{III}}$ product. Transient absorption studies have been undertaken to distinguish the excited state properties which permit the two-electron reactivity of the flexible complexes, while precluding that of the rigid analogs. Comparative transient absorption studies of $Mo_2Cl_4(PMe_3)_4$ and $Mo_2Cl_4(PBu_3)_4$ ($PBu_3 =$ tributylphosphine) have shown that the former decays monoexponentially to the ground state with the lifetime corresponding to that of the ${}^1\delta\delta^*$ emission,

whereas the $^1\delta\delta^*$ state of the latter decays to a long-lived, non-emissive transient.³¹ Several possible explanations have been provided for the nature of this long-lived transient, such as population of the low-lying $^3\delta\delta^*$ or some other state that does not couple effectively with the ground state.³¹ A more plausible alternative is a conformational distortion, which can be accomplished by a ligation core rearrangement. Similar differences have been observed for complexes of the type $\text{Mo}_2\text{Cl}_4(\overline{\text{P}}\text{P})_2$; when the bridging ligands, $\overline{\text{P}}\text{P}$, are dimethylphosphines the excited state decay takes place directly from the $^1\delta\delta^*$ excited state, whereas when $\overline{\text{P}}\text{P}$ = diphenylphosphines the long-lived non-emissive intermediate is observed.³¹ The difference in excited state properties between these complexes has been correlated to the differences in their cone angles.³² Recently, it has also been observed that two-electron oxidative-addition proceeds only with those complexes which exhibit the long-lived, non-emissive transient.²² In this Chapter the results of transient absorption spectroscopy of the $\text{M}_2\text{Cl}_4(\overline{\text{P}}\text{P})_2$ and $\text{M}_2\text{Cl}_4(\text{PR}_3)_4$ bimetallic complexes (D_{2h} and D_{2d} symmetries, respectively) will be presented, and correlations between structure and reactivity will be made. These studies have elucidated some of the properties required to effect two-electron photochemistry.

B. EXPERIMENTAL METHODS

The complexes were synthesized by Dr. Partigianoni; the synthesis and sample preparation procedures have been previously described.²¹ The transient absorption spectroscopy was either conducted on the picosecond

timescale with the instrument described in Chapter I.B or with nanosecond resolution. The nanosecond transient absorption measurements were made with the pulse-probe technique. The excitation source was a Quanta Ray DCR1 Nd:YAG laser whose fundamental frequency was doubled or tripled with a Quanta Ray HG-1 harmonic generator and the emanating beams separated with a Quanta Ray PHS-1 prism harmonic separator. For experiments where the excitation was 683 nm, the second harmonic of a Quanta Ray DCR2-A, prepared by the Quanta Ray HG-2 and separated from the fundamental by an ESCO dichroic mirror, was sent through a 1 m long Raman shifter filled to 60 psi with H₂ to obtain the first Stokes line.

The laser excitation beam intercepted a white light probe beam generated from a 150-W pulsed OSRAM Xe arc lamp (XBO150/S) mounted in a Photon Technology International (PTI) A1000 lamp housing and driven with a PTI LPS1000 power supply. The probe beam was collimated and refocused onto the sample (0.2 cm path length) by two 2 in, f/7.0 fused silica lenses. The excitation and probe beams were nearly collinear, with an incidence angle of 11°. The lamp was pulsed (5 Hz repetition rate) to ~12 A for a duration of 5 ms, and the white light was passed through a Uniblitz 23X mechanical shutter. The triggering of the Nd:YAG laser, pulsing of the lamp, and opening and closing of the shutter were orchestrated by synchronization electronics designed and built by Martin Rabb, Electronics Design Engineer, Chemistry Department, Michigan State University. The light transmitted by the sample was collimated by an f/7.0 lens and focused by a second lens (f/4.0) through an appropriate Schott cutoff filter (KV- or WG-series) onto the entrance slit of a SPEX 1680A monochromator. The signal obtained from a Hamamatsu R928 photomultiplier tube was amplified using a LeCroy 6103 dual amplifier/trigger. The amplifier output was

passed into a LeCroy TR8828D transient recorder, and the digitized signal was stored in two MM8104 memory modules arranged in a series configuration. The amplifier, digitizer, memory modules, and a LeCroy 6010 GPIB interface were housed in a LeCroy 8013A minicrate. Data, acquired and processed by a Compaq 386 computer equipped with a 40 megabyte hard disk, were typically averaged over 1000 pulses. A Tektronix DSA602A digitizing oscilloscope with a Tektronix 11A72 amplifier was also utilized to average the signal from the photomultiplier tube.

C. RESULTS AND DISCUSSION

1. D_{2h} Complexes: $M_2Cl_4(\overline{PP})_2$

Excitation of $Mo_2Cl_4(dppm)_2$, $Mo_2Cl_4(dmpm)_2$, $Mo_2Cl_4(dppe)_2$, and $Mo_2Cl_4(dmpe)_2$ ($dmpm$ = bis(dimethylphosphino)methane; $dppe$ = bis(diphenylphosphino)ethane; $dmpe$ = bis(dimethylphosphino)ethane) with wavelengths coincident with the $\delta\delta^*$ transition leads to the production of short-lived transients (40 ps - 2.4 ns). As reported by Dr. I-J. Chang, all complexes exhibit transients corresponding to the $\delta\delta^*$ excited state with lifetimes of 40 - 100 ps, although the complexes containing $dppm$ and $dppe$ ligands were observed to decay biexponentially, with lifetimes of the longer component of $\sim 2ns$.³² The origin of the second transient was unknown.

The transient absorption profiles of $Mo_2Cl_4(dmpm)_2$ at several times following 3 ps excitation (600 nm) are shown in Figure 26. The prominent feature at 460 nm is typical of $\delta\delta^*$ excited states; its intensity decays monoexponentially to the ground state with a lifetime of 40 ps. The lifetime

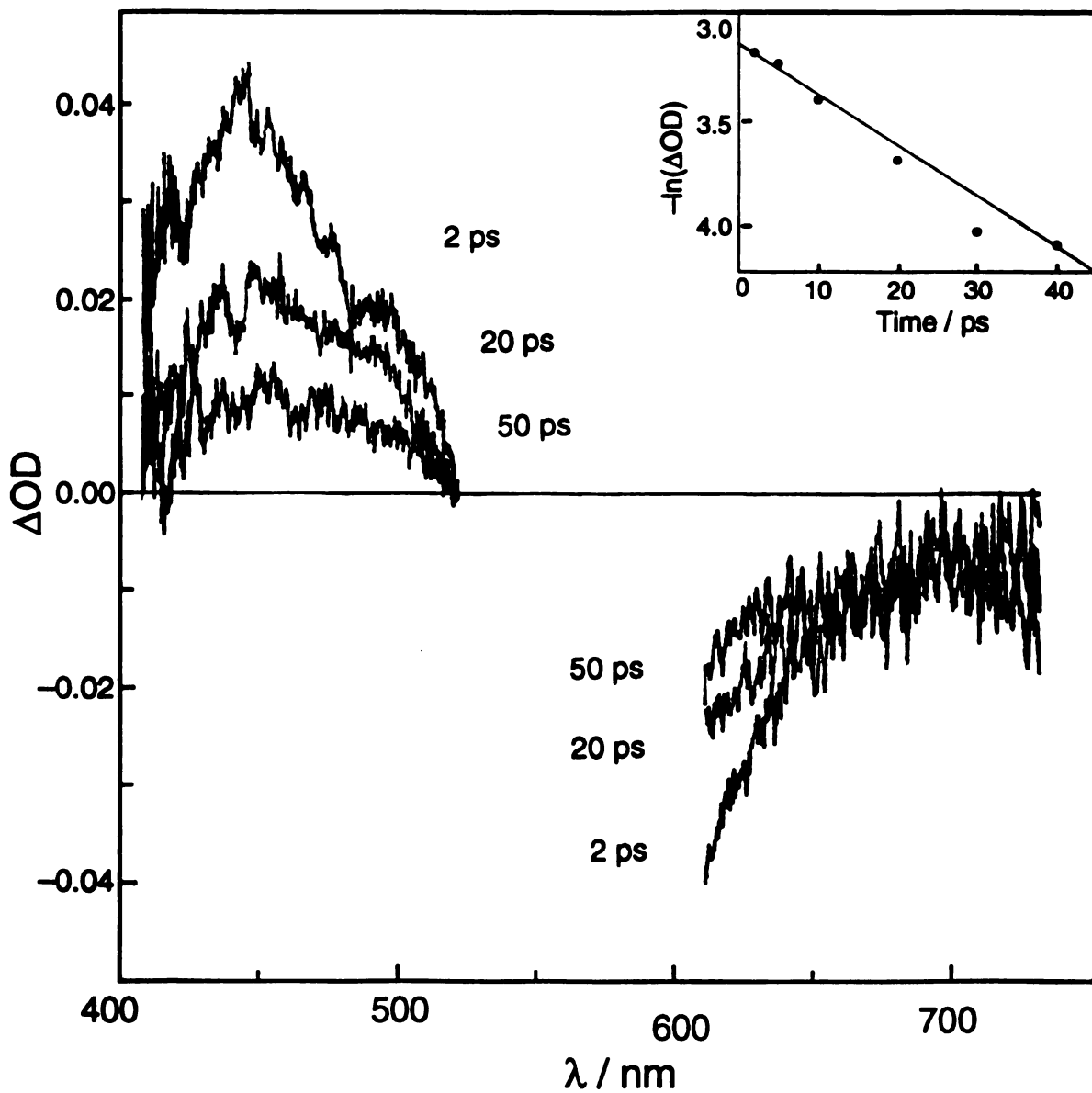


Figure 26. Transient absorption spectra of $\text{Mo}_2\text{Cl}_4(\text{dmpm})_2$ in CH_2Cl_2 collected 2, 20, and 50 ps following the 600 nm, 3 ps excitation pulse. The decay of the bleaching at 630 nm is shown in the inset.

of this decay parallels that for the ground state bleaching at 630 nm, corresponding to the $\delta\delta^*$ transition (Figure 26, inset). In these complexes long-lived transients are not observed upon $\delta\delta^*$ excitation. The lack of photochemical activity of these complexes in the presence of substrates upon $\delta\delta^*$ excitation is in agreement with this observation.²²

A long-lived transient is observed when benzene solutions of $\text{Mo}_2\text{Cl}_4(\text{dmpm})_2$ are excited at a higher energy ($\lambda_{\text{exc}} = 355 \text{ nm}$) than the $\delta\delta^*$ transition. This long-lived transient decays back to the ground state with a lifetime of 5 μs . The spectrum obtained 1 μs after the 10 ns pump pulse (Figure 27a) exhibits an absorption feature with a maximum at 520 nm. Because of an emissive impurity in the ligand, the spectrum could not be collected in the wavelength region below 450 nm.

Owing to the strong ligand emission from dppm ($\lambda_{\text{max}} = 460 \text{ nm}$, $\tau \sim 2 \text{ ns}$) similar transient spectroscopy experiments of $\text{Mo}_2\text{Cl}_4(\text{dppm})_2$ with high energy excitation ($\lambda_{\text{exc}} = 355 \text{ nm}$) could not be conducted. However, in the tungsten analog, $\text{W}_2\text{Cl}_4(\text{dppm})_2$, the electronic absorption spectrum is red-shifted, thus allowing excitation at energies higher than $\delta\delta^*$ without populating the emissive state of the ligand. The transient absorption spectra of $\text{W}_2\text{Cl}_4(\text{dppm})_2$ in benzene, collected 100 ns and 4 μs after the laser pulse, are shown in Figure 28a. The initial spectrum shows an intense absorption into the ultraviolet ($\lambda < 430 \text{ nm}$) and a peak with a maximum at 480 nm. However, the decay of the intensity with time is not monotonic. The decay of the transient at 440 nm is shown in the inset of Figure 28a, where there is a depopulation of the initially prepared state followed by a rise in intensity with subsequent decay to the ground state over 100 μs . The long-lived transients are not observed for $\delta\delta^*$ excitation of $\text{W}_2\text{Cl}_4(\text{dppm})_2$ ($\lambda_{\text{exc}} = 683 \text{ nm}$).

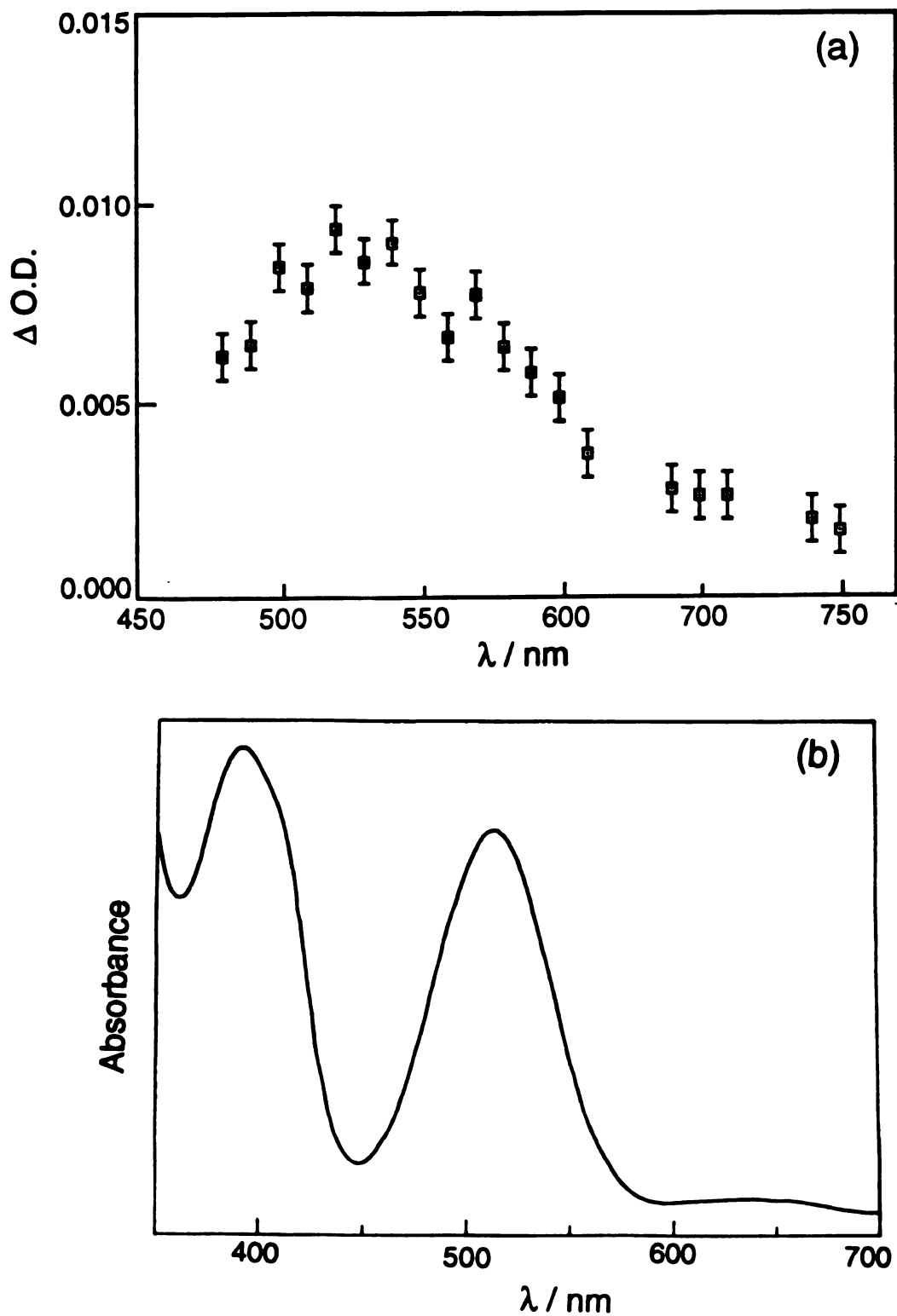


Figure 27. (a) Transient absorption spectrum of $\text{Mo}_2\text{Cl}_4(\text{dmpm})_2$ in CH_2Cl_2 recorded 1 μs after 355 nm, 10 ns excitation and (b) electronic absorption spectrum of independently-prepared $\text{Mo}_2\text{Cl}_6(\text{dppm})_2$.

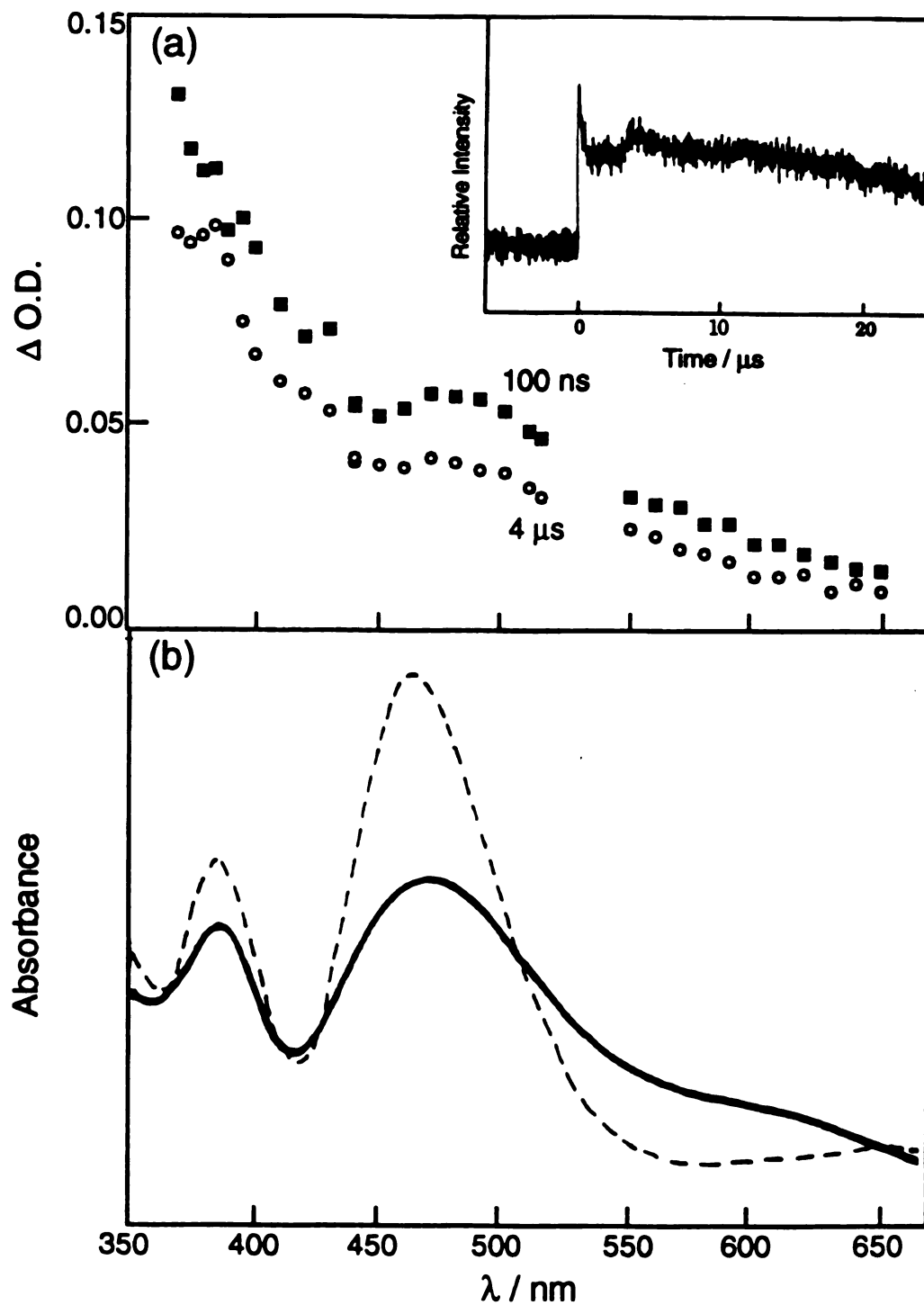
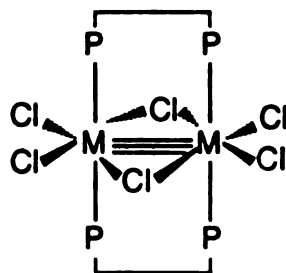


Figure 28. (a) Transient absorption spectra of $W_2Cl_4(dppm)_2$ in benzene recorded 100 ns and 4 μs after 532 nm, 10 ns excitation. (b) Absorption spectra of $W_2Cl_6(PEt_3)_4$ (---) and $W_2Cl_6(dppm)_2$ (—) in toluene and CH_2Cl_2 , respectively.

The transient absorption spectra are similar to the electronic absorption spectra of $\text{Mo}^{\text{III}}\text{Mo}^{\text{III}}$ edge-sharing bioctahedra, 4. The structure of these complexes is dictated by the two bridging chlorides, which are shared by the two octahedral metal centers to form an edge-sharing bioctahedron as shown below,



4

Two of these complexes, $\text{Mo}_2\text{Cl}_6(\text{dppm})_2$ and $\text{W}_2\text{Cl}_6(\text{dppm})_2$, have been independently prepared by Dr. Partigianoni in our laboratory and their electronic absorption spectra are shown in Figures 27b and 28b.²¹ The spectrum of $\text{Mo}_2\text{Cl}_6(\text{dppm})_2$ exhibits a peaks at 390 and 500 nm in the visible region whereas the absorptions are blue-shifted in the tungsten analog, with maxima at 468 and 387 nm.²² The absorption maxima of several Mo and W edge-sharing bioctahedral complexes are listed in Table VIII. The spectral profiles of the electronically excited Mo and W quadruply-bonded complexes are similar to those of their corresponding edge-sharing bioctahedral complexes, although the electron count of the chemically distorted transients ($\text{M}^{\text{I}}\text{M}^{\text{III}} = \text{d}^5\text{d}^3$) is different than that of the $\text{M}_2\text{Cl}_6(\overline{\text{P}}\text{P})_2$ complexes ($\text{M}^{\text{III}}\text{M}^{\text{III}} = \text{d}^3\text{d}^3$). Such similarities may be accounted for by the prediction of a small gap in the HOMO-LUMO manifold.^{25,38-40} Inasmuch as the lowest energy transitions would be predicted to lie in the near-ir, higher energy visible absorptions for these

Table VIII. Ground State Electronic Absorption Maxima of Several Edge-Sharing Bioctahedral Complexes in the Visible Region.

| Complex | $\lambda_{\text{abs}} / \text{nm}$ | Reference |
|---|------------------------------------|-----------|
| $\text{Mo}_2\text{Cl}_6(\text{dppm})_2$ | 530 | 33 |
| $\text{Mo}_2\text{Cl}_4(\text{dppm})_2\text{Br}_2$ | 540 | 33 |
| $\text{Mo}_2\text{Cl}_4(\text{dppm})_2\text{I}_2$ | 580 | 33 |
| $\text{Mo}_2\text{Cl}_6(\text{dppe})_2$ | 507 | 34 |
| $\text{Mo}_2\text{Cl}_5(\text{dppm})_2(\text{SPh})$ | 540 | 35 |
| $\text{W}_2\text{Cl}_4(\text{dppm})_2\text{I}_2$ | 500 | 21 |
| $\text{W}_2\text{Cl}_4(\text{dppm})_2(\mu\text{-SPh})_2$ | 504 | 36 |
| $\text{W}_2\text{Cl}_4(\text{dppm})_2(\mu\text{-Cl})(\mu\text{-SPh})$ | 435 | 36 |
| $\text{W}_2\text{Cl}_4(\text{dppm})_2(\mu\text{-Cl})(\mu\text{-H})$ | 464 | 37 |

systems may have similar transitions that are not of HOMO-LUMO parentage. Notwithstanding, the similarities between $W_2Cl_4(\overline{P}P)_2$ transients and edge-sharing bioctahedral complexes are striking and have led us to suggest that the chemically distorted intermediate responsible for the long-lived non-luminescent transient spectra of $M_2X_4(\overline{P}P)_2$ species is an edge-sharing bioctahedron.

The manner in which such a geometry may be attained in the excited state is by a foldover of the two axial chlorides on the reduced metal to bridging positions (Figure 29). As discussed above, however, excitation of the $\delta\delta^*$ transition is not sufficient to promote the foldover. Higher energy excitation weakens the π bonding, thus allowing the d_{xz} and d_{yz} orbitals to bond to bridging chlorides. The proposed foldover mechanism is shown in Figure 29, where high energy excitation ($\pi \rightarrow \delta^*$) leads to the formation of the two-electron mixed-valence excited state. The foldover to edge-sharing bioctahedral geometry has a two-fold purpose: it stabilizes the charge on both metals by shifting it from the reduced to the oxidized center, and it induces the desired octahedral geometry about the high-valent metal. As shown in Figure 29 this foldover mechanism opens two coordination sites at the low-valent center, which makes it susceptible to two-electron oxidative addition. Indeed the photochemical reactivity of these complexes is in agreement with this mechanism, with reactions proceeding only upon $\pi \rightarrow \delta^*$ excitation and the localization of the two-electron addition on one metal.

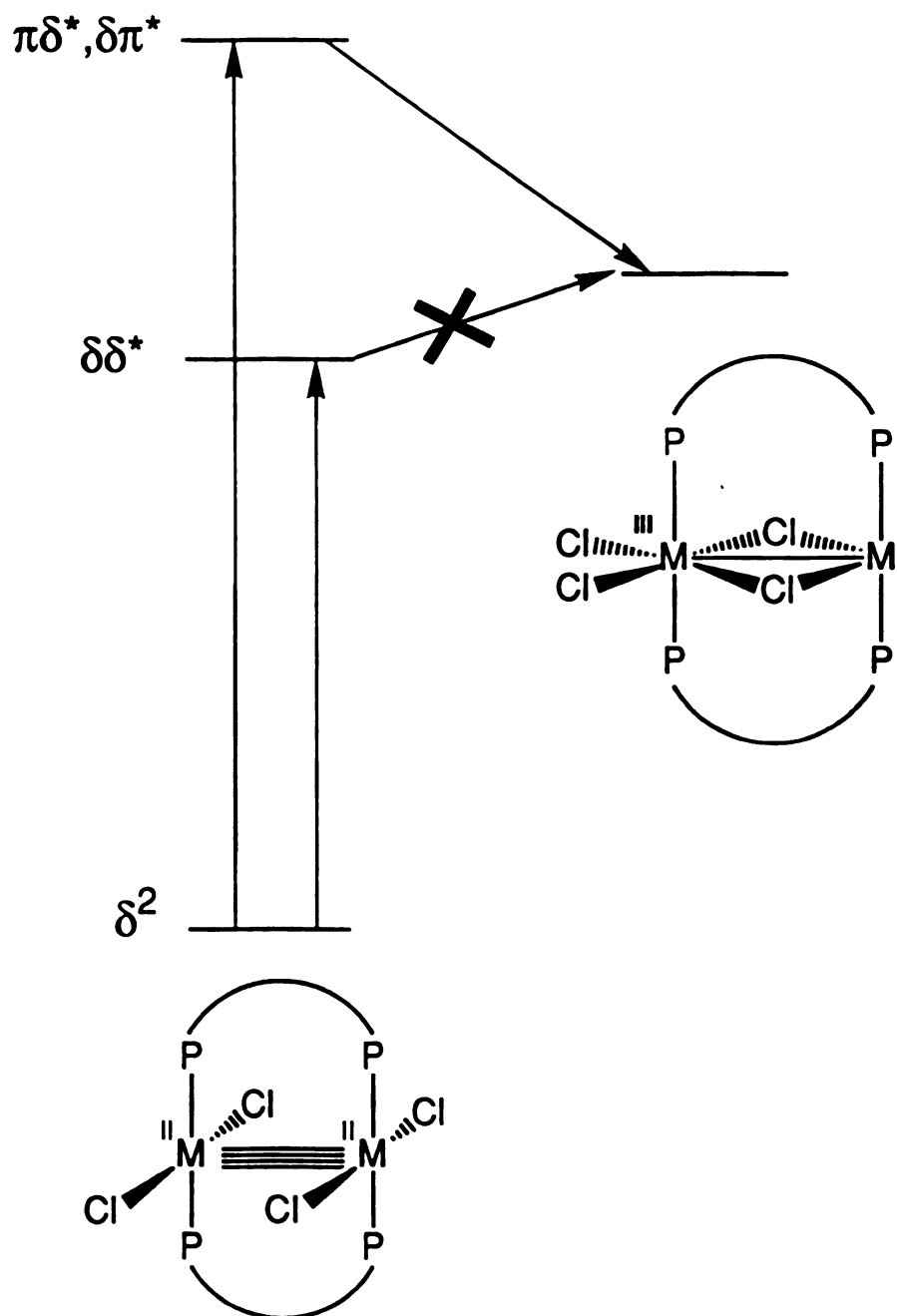


Figure 29. Proposed mechanism for the formation of the long-lived transient in D_{2h} complexes following high-energy excitation.

2. D_{2d} Complexes: $M_2Cl_4(PR_3)_4$

The $^1\delta\delta^*$ excited state of complexes in the $M_2Cl_4(PR_3)_4$ ($M = Mo, W$) series is for the most part highly emissive, and the luminescence lifetimes are typically in the 10 – 100 ns range. The emissive lifetimes and quantum yields are listed in Table IX for the $Mo_2Cl_4(PR_3)_4$ series, where $PR_3 = PMe_3, PEt_3, PBu_3, PPh_2Me, PMe_2Ph,$ and $PHPh_2$ ($PEt_3 =$ triethylphosphine, $PPh_2Me =$ diphenylmethyphosphine, $PMe_2Ph =$ dimethylphenylphosphine, and $PHPh_2 =$ diphenylphosphine). The transient absorption spectra for several of the Mo complexes following $\delta\delta^*$ excitation have been previously reported. For example, $Mo_2Cl_4(PBu_3)_4$ exhibits an absorption peak at 440 nm, which is characteristic of $\delta\delta^*$ spectra.^{31,32} The transient absorption spectrum of $Mo_2Cl_4(PHPh_2)_4$ decays with the unusually short lifetime of 180 ps, has a maximum at 420 nm, as shown in Figure 30, and is consistent with other $^1\delta\delta^*$ spectra.^{31,32} The transition giving rise to the absorption at 440 nm in the $^1\delta\delta^*$ excited state transient spectrum of $Mo_2X_4(PBu_3)_4$ ($X = Cl, Br, I$) has been assigned to be either metal-metal based or metal-to-phosphine charge transfer, since its energy remains constant along the halide series.³²

The transient absorption spectra collected following $^1\delta\delta^*$ excitation of the analogous tungsten series, $W_2Cl_4(PR_3)_4$, with $PR_3 = PEt_3, PBu_3, PPh_2Me$, are shown in Figures 31–33. In all cases there is weak absorption throughout the visible region (500 – 400 nm), with intensity increasing markedly toward the UV, in the 400 – 300 nm region. The transient decays of the tungsten complexes are comparable to the emissive lifetimes of the $\delta\delta^*$ excited state, which are in the 50 to 80 ns range. Unfortunately, with our present instrumentation, the decay of transients in this time regime cannot be accurately measured. The transient absorption and luminescence

Table IX. Lifetimes and Emissive Quantum Yields of the $\delta\delta^*$ Excited State of $\text{Mo}_2\text{Cl}_4(\text{PR}_3)_4$ Complexes and Non-Emissive Transient Lifetimes.

| PR_3 | $\tau_{\text{em}} / \text{ns}^a$ | ϕ_{em}^a | τ / ns^b |
|-------------------------|----------------------------------|----------------------|----------------------|
| PMe_3 | 135 | 0.259 | – |
| PEt_3 | 14 | 0.013 | 120 |
| PBu_3 | 21 | 0.013 | 120 |
| PPh_2Me | 11.4 | 0.011 | 80 |
| PMe_2Ph | <i>c</i> | <i>c</i> | 120 |
| PPh_2 | 0.18 | <i>d</i> | – |

^aRef. 22. ^bLifetime of long-lived transient; approximate values due to instrumental constraint (see text). ^cNot measured. ^dEmission not observed.

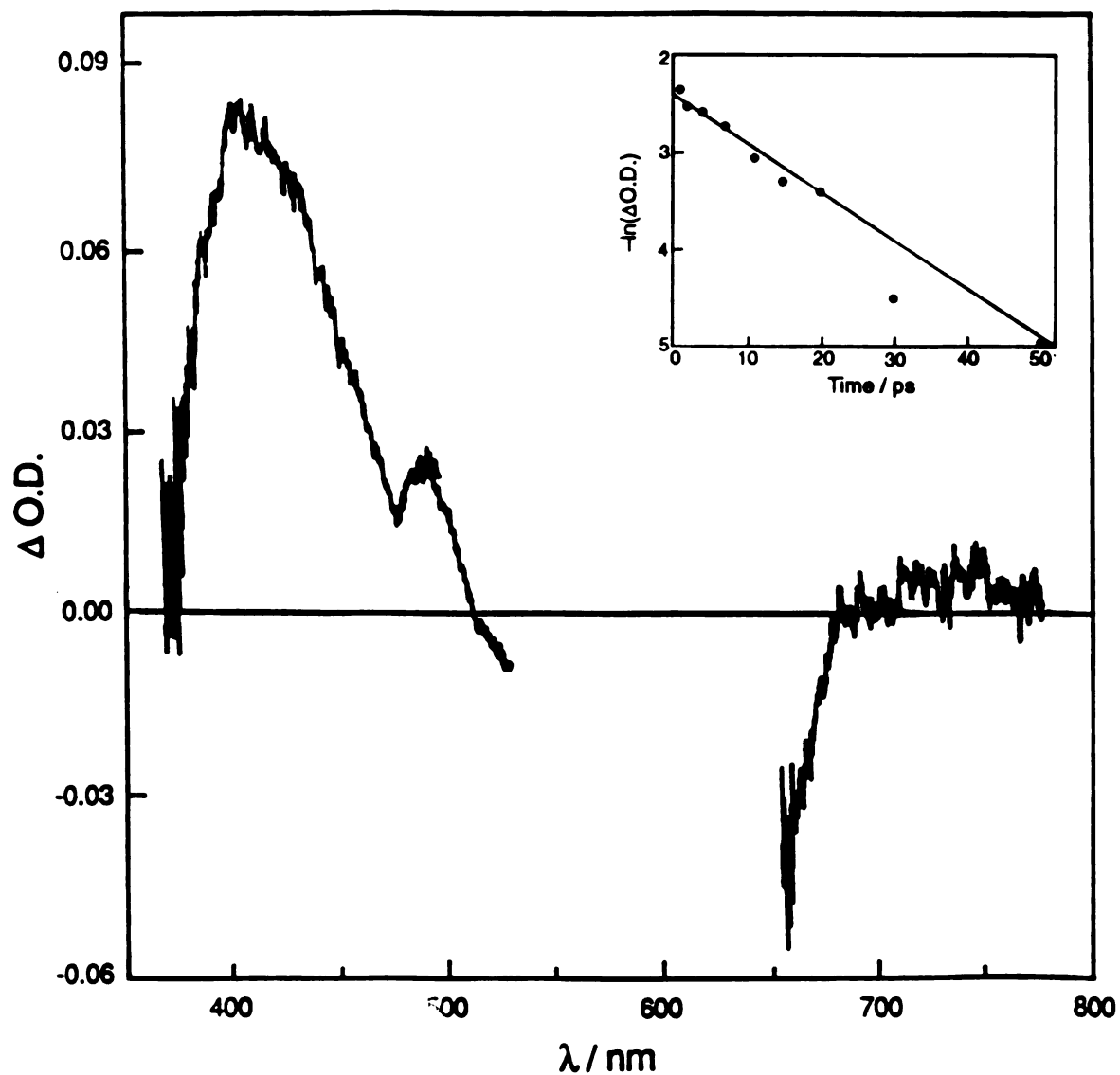


Figure 30. Transient absorption spectrum of $\text{Mo}_2\text{Cl}_4(\text{PPh}_2)_4$ in CH_2Cl_2 collected 2 ps after the 600 nm, 3 ps excitation. The inset shows the decay of the absorbance at 420 nm.

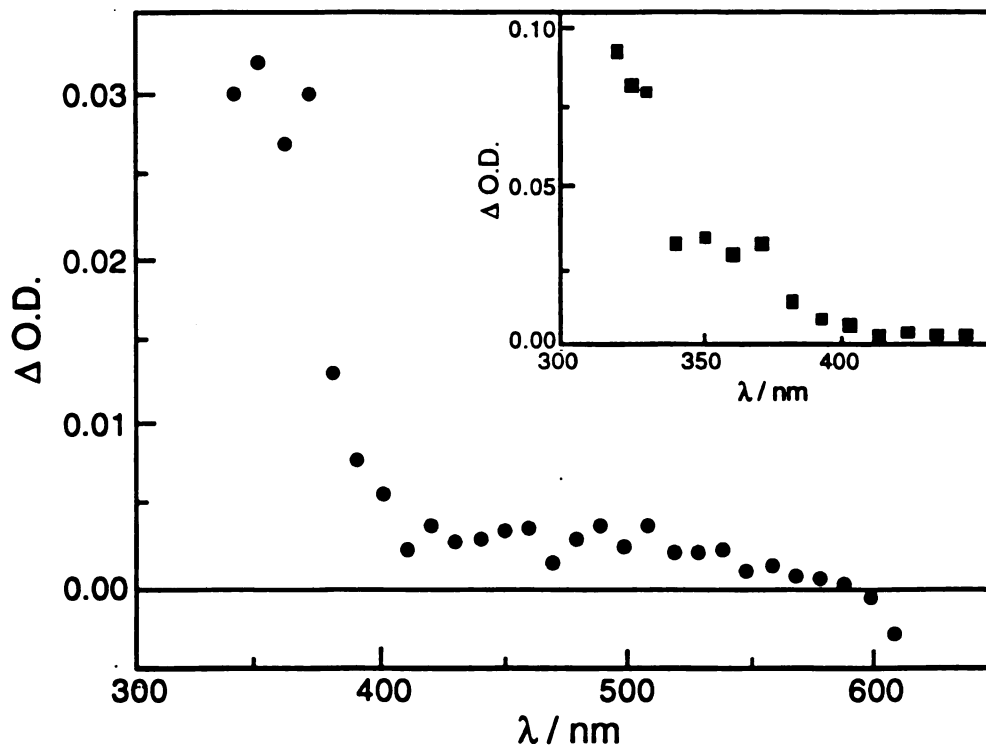


Figure 31. Transient absorption spectrum of $W_2Cl_4(PEt_3)_4$ in toluene recorded 70 ns after the 683 nm excitation pulse; the inset shows the spectral profile in the near UV region.

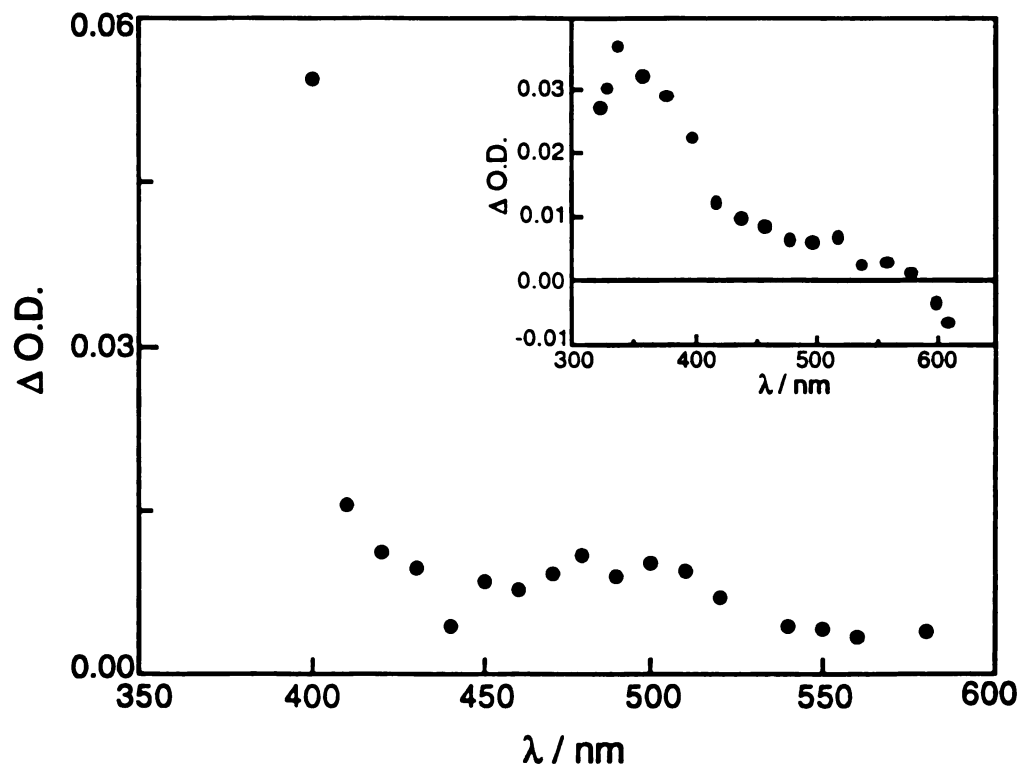


Figure 32. Transient absorption spectrum of $W_2Cl_4(PBu_3)_4$ in CH_2Cl_2 recorded 70 ns after the 683 nm excitation pulse; the inset shows the spectral profile in the near UV region.

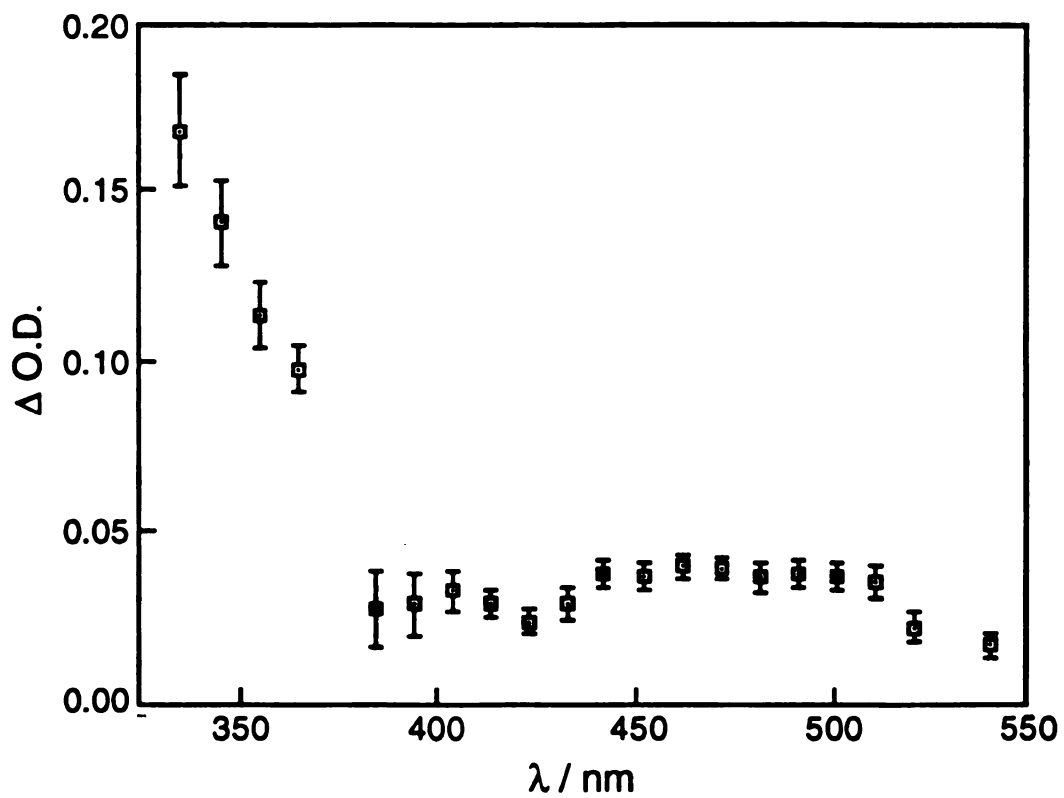


Figure 33. Transient absorption spectrum of $W_2Cl_4(PPh_2Me)_4$ in THF recorded 70 ns after 683 nm, 10 ns excitation.

decays of $W_2Cl_4(PMe_3)_4$ and $W_2Cl_4(PBu_3)_4$ are shown in Figure 34. It was therefore concluded from inspection of the decays that the transient absorption signal is due to the $^1\delta\delta^*$ excited state.

In addition to the signal from the $^1\delta\delta^*$ excited state, a second long-lived transient was observed for the molybdenum complexes when $PR_3 = PEt_3, PBu_3, PPh_2Me,$ and PMe_2Ph (the PMe_3 and PPh_2 complexes only exhibit a transient due to $^1\delta\delta^*$). In contrast to the bridged D_{2h} complexes discussed above, this long-lived transient is observed upon $\delta\delta^*$ excitation. The lifetimes of the long-lived non-emissive transients are listed in Table IX. The spectral profiles of the long-lived transients formed upon $^1\delta\delta^*$ excitation of $Mo_2Cl_4(PR_3)_4$ complexes, where $PR_3 = PBu_3, PPh_2Me,$ and $PMe_2Ph,$ are shown in Figure 35, where there the signal exhibits a maximum at ~ 400 nm. These spectra are in good agreement with those reported for $Mo_2Cl_4(PBu_3)_4$ in dichloromethane and acetonitrile, where a peak at 390 nm is observed.³¹ Figure 36 compares the decay of $Mo_2Cl_4(PPh_2Me)_4$ at 400 nm and 440 nm. At the former wavelength the long-lived transient is at a maximum, whereas at 440 nm only the $^1\delta\delta^*$ absorbs significantly. This difference is apparent from inspection of decays. At 400 nm both the signal from the $^1\delta\delta^*$ excited state and that from the long-lived transient are present, whereas only the short-lived $^1\delta\delta^*$ signal appears at 440 nm.

The nature of the long-lived transient remains unknown. However, phosphine dissociation has been ruled out as the origin of the non-luminescent transient, since the lifetime of the transient does not change upon addition of excess free phosphine to the solutions probed. No correlation was found in the comparison of phosphine basicity with the absence of the long-lived transient.

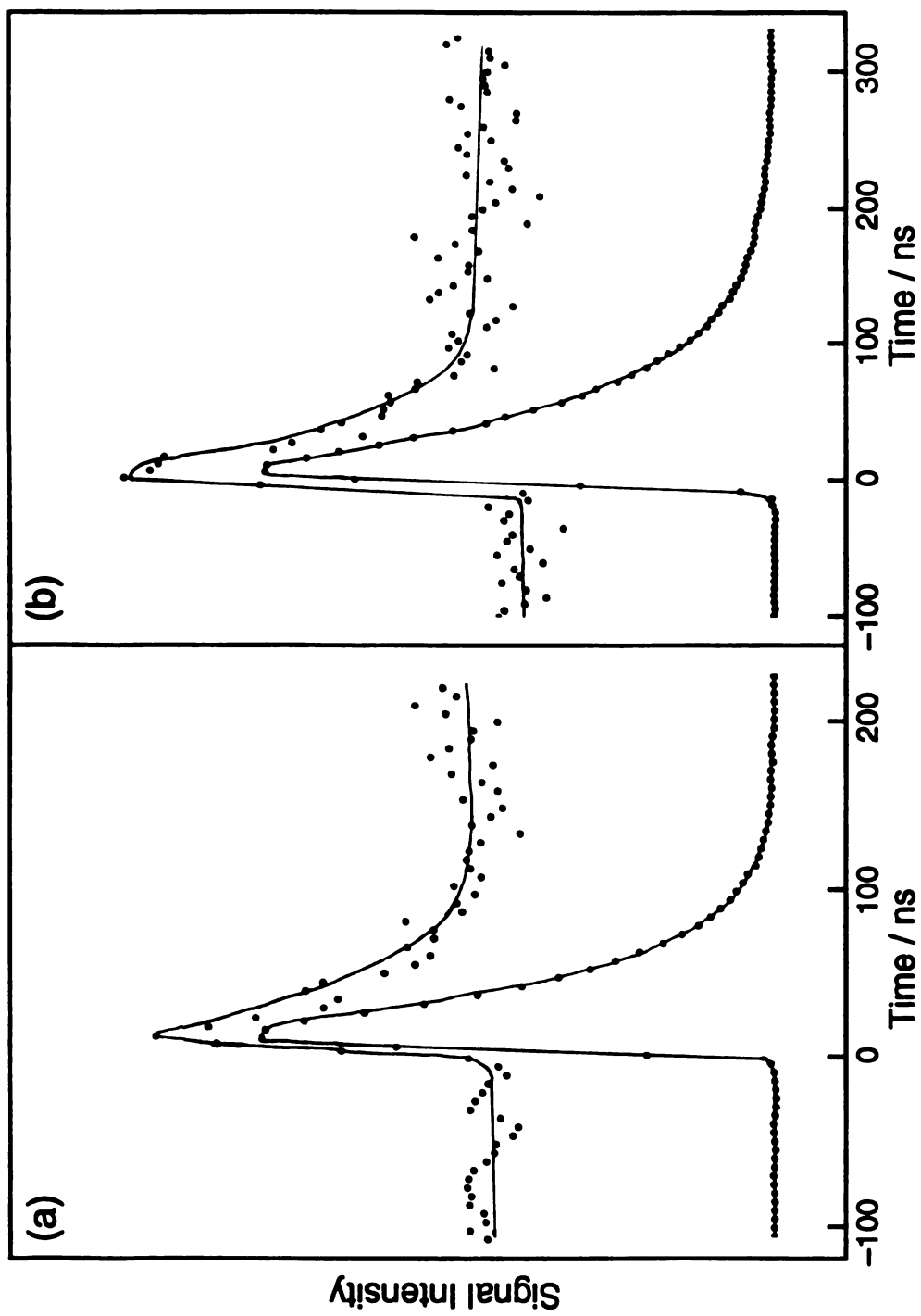


Figure 34. Decays of (a) $W_2Cl_4(PMe_3)_4$ and (b) $W_2Cl_4(PBu_3)_4$ following 683 nm excitation; in both cases the top curve is that of the transient absorption signal at 500 nm and the bottom corresponds to the luminescence decay at 800 nm.

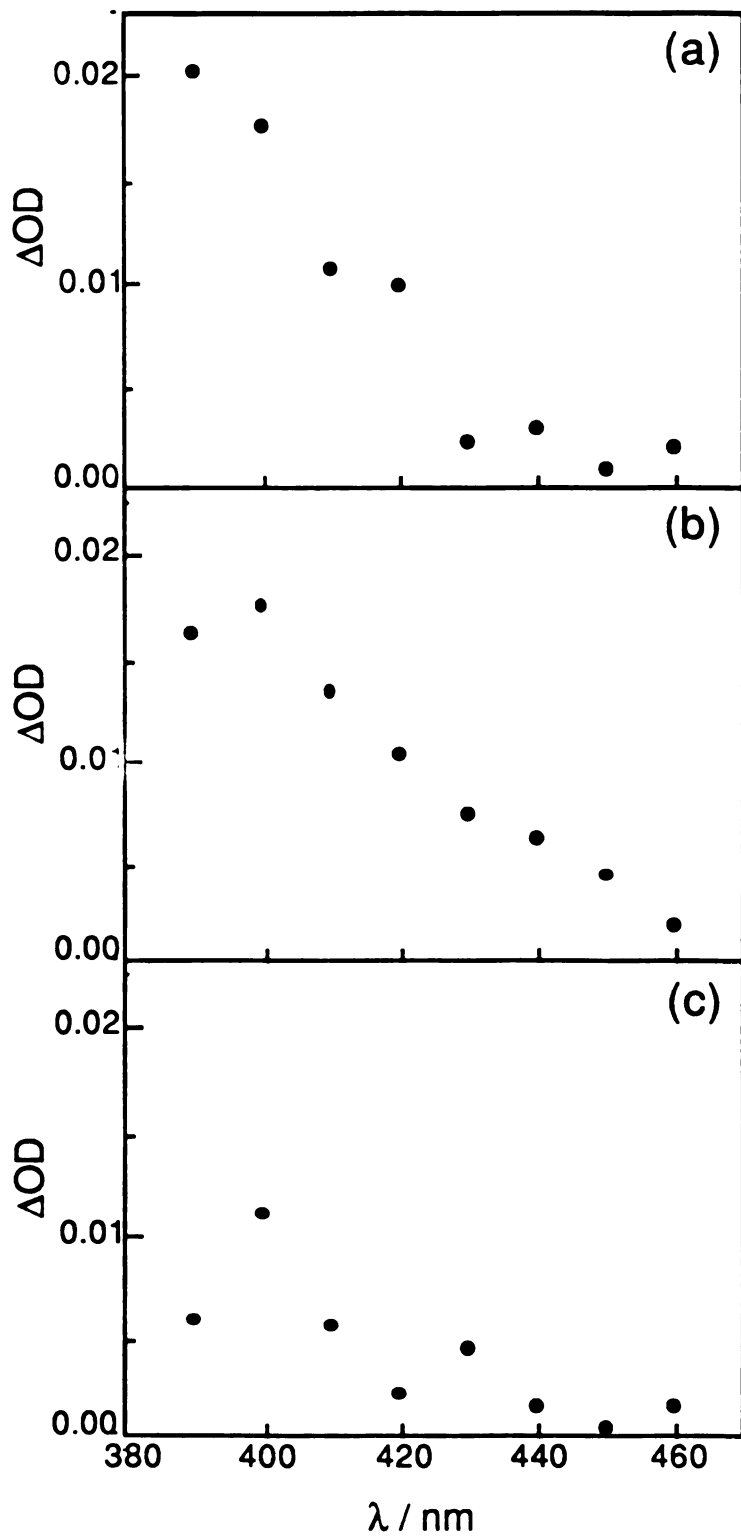


Figure 35. Transient absorption spectra recorded 60 ns after 532 nm excitation of (a) $\text{Mo}_2\text{Cl}_4(\text{PBu}_3)_4$, (b) $\text{Mo}_2\text{Cl}_4(\text{PMe}_2\text{Ph})_4$, and (c) $\text{Mo}_2\text{Cl}_4(\text{PPh}_2\text{Me})_4$ in CH_2Cl_2 ,

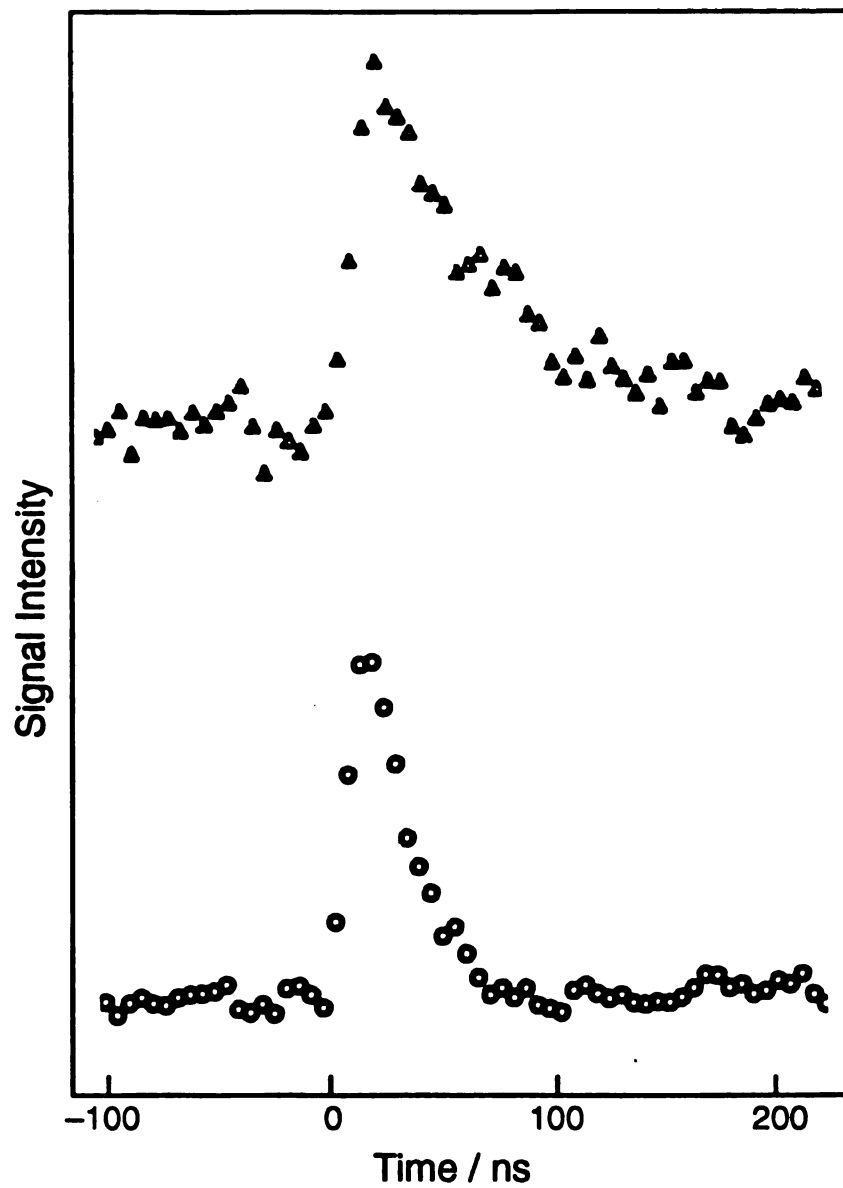


Figure 36. Decays of $W_2Cl_4(PPh_2Me)_4$ in CH_2Cl_2 followed at (Δ) 400 nm and (\circ) 440 nm after 532 nm, 10 ns excitation.

There are marked differences in emissive quantum yields and $^1\delta\delta^*$ lifetimes among the molybdenum complexes, $\text{Mo}_2\text{Cl}_4(\text{PR}_3)_4$. The magnitude of these differences is clearly observed in Figure 37, where the two parameters are plotted. The square point corresponds to $\text{Mo}_2\text{Cl}_4(\text{PPh}_2)_4$, whose emissive lifetime is two orders of magnitude shorter than those observed for most complexes. This excited state behavior is consistent with a faster deactivation pathway, different from that in action in the other complexes of the series. It may be suggested that the P–H bond, which has a higher vibrational frequency than the P–C bonds found in all the other complexes, may be involved in such deactivation. If this deactivation model is correct, the complex $\text{Mo}_2\text{Cl}_4(\text{PDPH}_2)_4$, with the deuterated ligand, should exhibit a longer lifetime than that of its protonated analog. In Figure 37, the open circle corresponds to $\text{Mo}_2\text{Cl}_4(\text{PMe}_3)_4$, whose lifetime and emissive quantum yield are one order of magnitude greater than those of $\text{Mo}_2\text{Cl}_4(\text{PEt}_3)_4$, $\text{Mo}_2\text{Cl}_4(\text{PBu}_3)_4$, and $\text{Mo}_2\text{Cl}_4(\text{PPh}_2\text{Me})_4$. Since the long-lived transient is not observed in the PMe_3 complex, the differences in $^1\delta\delta^*$ lifetime and emissive quantum yield suggests that deactivation of the $^1\delta\delta^*$ excited state in the PEt_3 , PBu_3 , and PPh_2Me complexes takes place through the state giving rise to the long-lived transient.³¹ The lifetimes of the molybdenum $\text{PR}_3 = \text{PMe}_3$, PEt_3 , PBu_3 complexes converge at 77K, which indicates that the formation of the long-lived transient from the $^1\delta\delta^*$ excited state is an activated process, consistent with a conformational rearrangement.^{31,41} Since the transition to the low-lying $^3\delta\delta^*$ is not expected to be activated, the long-lived transient is not believed stem from the $^3\delta\delta^*$.

It may be postulated that the size of the phosphine ligand, measured by its cone angle, plays a role in the formation of the non-emissive transient. In studies utilizing a series of $\text{Mo}_2\text{Cl}_4(\text{PR}_3)_4$ complexes, including only PR_3

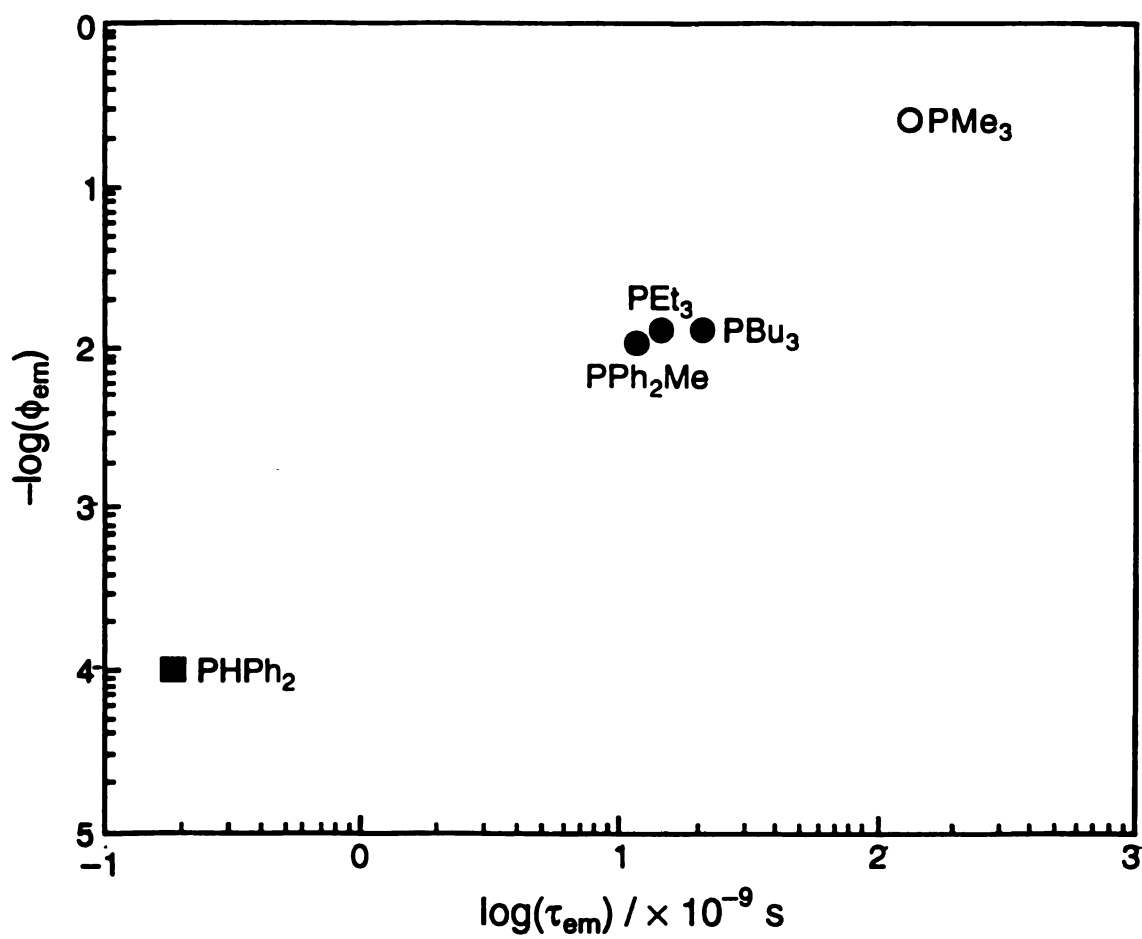


Figure 37. Log-log plot of the emission quantum yield vs the $^1\delta\delta^*$ lifetime of complexes in the $\text{Mo}_2\text{Cl}_4(\text{PR}_3)_4$ series.

= PMe_3 , PEt_3 , PPr_3 , and PBu_3 , a correlation between the observation of the long-lived transient and the phosphine cone angle had been proposed.³¹ The long-lived transient was not observed for PMe_3 , which has the smallest cone angle (118°) compared to the other members of the series ($\sim 132^\circ$).⁴² The cone angles of the phosphines utilized in our extended series, which includes PMe_2Ph , PPh_2Me , and PPhPh_2 , are listed in Table X. The correlation of cone angle with observation of the long-lived transient is obscured by PPhPh_2 , since its value lies between that of PMe_2Ph and those for PEt_3 and PBu_3 . However, as discussed above, the formation of the long-lived transient may not be an issue in the photophysics of $\text{Mo}_2\text{Cl}_4(\text{PPhPh}_2)_4$, since the $^1\delta\delta^*$ excited state may decay too quickly, by other non-radiative pathways, to

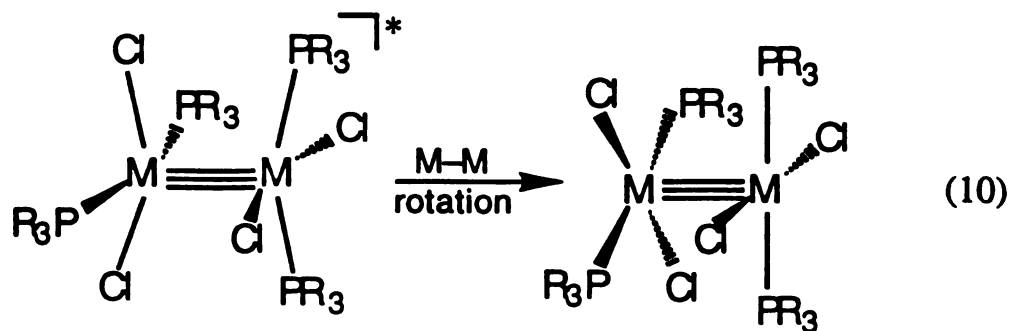
Table X. Cone Angles (ϕ) of PR_3 Ligands.

| PR_3 | ϕ / degrees ^a |
|-------------------------|-------------------------------|
| PMe_3 | 118 |
| PMe_2Ph | 122 |
| PPhPh_2 | 128 |
| PEt_3 | 132 |
| PBu_3 | 132 |
| PPh_2Me | 136 |

^aRef. 42; average value of the three angles, therefore PMe_2Ph has a large angle (145°) on one side associated with the phenyl group.

permit the formation of the long-lived transient. If this is the case, then its cone angle should not be compared with the others, and the only complex that does not have a long-lived transient is $\text{Mo}_2\text{Cl}_4(\text{PMe}_3)_4$, with the smallest cone angle.

The σ and π bonds are symmetric about the metal-metal bond in D_{2d} symmetry (Figure 23); therefore once the δ bond is broken, by placing the molecule in the ${}^1\delta\delta^*$ excited state, the $\text{MCl}_2(\text{PR}_3)_2$ fragments may rotate about the central bond. Thus, with small phosphines, such as PMe_3 , the fragment can rotate freely, whereas when a larger phosphine is present there may be steric hindrance to free rotation. However, in the molecules containing the bulky phosphines, there is significant repulsion between the PR_3 ligand and the adjacent Cl , as displayed by the large $\text{M}-\text{M}-\text{P}$ and $\text{M}-\text{M}-\text{Cl}$ bond angles, typically 105° and 108° , respectively.⁴³⁻⁴⁸ To minimize these steric repulsions in the eclipsed conformation, the molecules may rotate to attain a staggered (D_2) geometry, with subsequent relaxation of the bond angle to smaller values. Such rearrangement is shown in Equation 10, where after the initial rotation the phosphines become locked in place.



Such behavior is not unexpected, since it is well known that $\text{Mo}_2\text{Cl}_4(\text{PPh}_3)_4$ cannot be synthesized owing to the large phosphine.²² This observation is consistent with the postulated lack of steric strain in the $\text{Mo}_2\text{Cl}_4(\text{PMe}_3)_4$

complex, and the necessity of the sterically-hindered complexes to rearrange.

The electronic absorption spectrum of $\text{Mo}_2\text{Cl}_4(\text{dppe})_2$, which is known to be somewhat staggered across the Mo–Mo bond (torsional angle of bidentate phosphine $\sim 27^\circ$), is similar to that of long-lived transient.⁴⁹ The transient absorption spectrum of $\text{Mo}_2\text{Cl}_4(\text{PBU}_3)_4$, reported by Winkler over a larger spectral range, has marked similarities with that of the staggered complex.³¹ The transient exhibits absorption maxima at 750, 470, and 390 nm, which are similar to those of $\text{Mo}_2\text{Cl}_4(\text{dppe})_2$ at 762, 548, 469, and 345 nm.⁴⁹ The high energy absorption in $\text{Mo}_2\text{Cl}_4(\text{dppe})_2$ has been assigned to a $\pi \rightarrow \delta^*$ transition, whereas in the $\text{Mo}_2\text{Cl}_4(\text{PR}_3)_4$ complexes the same transition appears at ~ 440 nm. Therefore it is not unreasonable to correlate the peak at 345 nm in the staggered complex with that at 390 nm in the transient. Points in the 500 – 550 nm region were not collected in the transient spectrum, since the excitation was 532 nm; thus the small peak at 548 nm in $\text{Mo}_2\text{Cl}_4(\text{dppe})_2$ cannot be compared.

The long-lived transient was not observed for any of the complexes probed from the $\text{W}_2\text{Cl}_4(\text{PR}_3)_4$ series or in $\text{MoWCl}_4(\text{PMePh}_2)_4$. However, the metal-metal distances in the W_2 and MoW complexes are 0.13 Å and 0.08 Å longer than those in the corresponding Mo_2 series.⁴³⁻⁴⁸ The longer distance between metals may indeed provide sufficient space about the metal-metal core to reduce the steric constraints of the large phosphines. If the observation of the long lived transient is indeed dictated by the steric repulsions of the phosphines, then it would be expected that in the complexes with the longer metal-metal bonds the non-emissive transient may not be observed.

D. CONCLUDING REMARKS

Upon $\delta\delta^*$ excitation, the D_{2h} complexes exhibit transient features due only to the $^1\delta\delta^*$ excited state. In contrast, the D_{2d} complexes exhibit a longer-lived transient in addition to the $^1\delta\delta^*$ when excited with low-energy wavelengths, coincident with the $\delta\delta^*$ absorption. This long-lived transient in the D_{2d} complexes is believed to stem from a conformational rearrangement involving rotation about the metal-metal bond to minimize steric repulsions of bulky phosphines. Such rearrangement cannot occur in the bridged D_{2h} complexes, in agreement with the absence of long-lived transients in these complexes upon $\delta\delta^*$ excitation. The D_{2h} complexes, however, exhibit a long-lived transient when excited with higher-energy photons, coincident with their $\pi\delta^*$ transition. These non-emissive transients have been assigned to a conformationally distorted species, where the foldover of two chlorides to bridging positions form an edge-sharing bioctahedron.

E. REFERENCES

1. (a) Wikström, M. *Nature* **1989**, *338*, 776. (b) Wikström, M. *Chemica Scripta* **1987**, *27B*, 53.
2. (a) Malmström, B. G. *Chim. Scripta* **1987**, *27B*, 67. (b) Oliveberg, M.; Brzezinski, P.; Malmström, B. G. *Biochim. Biophys. Acta* **1989**, *977*, 322. (c) Malmström, B. G. *Chem. Rev.* **1990**, *90*, 1247. (d) Malmström, B. G. *Arch. Biochem. Biophys.* **1990**, *280*, 233.

3. Williams, R. J. P. *Nature* **1989**, *338*, 709.
4. Han, S.; Ching, Y.-C.; Rousseau, D. L. *Proc. Natl. Acad. Sci. USA* **1990**, *87*, 8408.
5. Hansson, O.; Wydrzynski, T. *Photosynth. Res.* **1990**, *23*, 131.
6. Ghanotakis, D. F.; Yocum, C. F. *Annu. Rev. Plant Physiol. Plant Mol. Biol.* **1990**, *41*, 255.
7. (a) Brudvig, G. W.; Crabtree, R. H. *Prog. Inorg. Chem.* **1989**, *37*, 99.
(b) Brudvig, G. W.; Beck, W. F. *Annu. Rev. Biophys. Chem.* **1989**, *18*, 25. (c) Thorp, H. H.; Brudvig, G. W. *New J. Chem.* **1991**, *15*, 479.
8. Babcock, G. T. In *New Comprehensive Biochemistry: Photosynthesis*; Amesz, J.; Ed.; Elsevier: New York, 1987; pp 125-158.
9. (a) Krishtakik, L. I. *Biochim. Biophys. Acta* **1986**, *849*, 162. (b) Krishtakik, L. I. *Bioelectrochem. Bioenerg.* **1990**, *23*, 249.
10. (a) Vincent, J. B.; Christou, G. *Adv. Inorg. Chem.* **1989**, *33*, 197. (b) Libby, E.; McCuster, J. K.; Schmitt, E. A.; Folting, K.; Hendrickson, D. N.; Christou, G. *Inorg. Chem.* **1991**, *30*, 3486.
11. (a) Micklitz, W.; Bott, S. G.; Bentsen, J. G.; Lippard, S. J. *J. Am. Chem. Soc.* **1989**, *111*, 372. (b) Bentsen, J. G.; Micklitz, W.; Bott, S. G.; Lippard, S. J. *J. Inorg. Biochem.* **1989**, *36*, 226.
12. (a) Chan, M. K.; Armstrong, W. H. *J. Am. Chem. Soc.* **1991**, *113*, 5055. (b) Chan, M. K.; Armstrong, W. H. *J. Am. Chem. Soc.* **1990**, *112*, 4985.
13. Proserpio, D. M.; Hoffman, R.; Dismukes, G. C. *J. Am. Chem. Soc.* **1992**, *114*, 4374.

14. Taube, H. In *Mechanistic Aspects of Inorganic Reactions*; Rorabacher, D. B.; Endicott, J. F., Eds.; ACS Symposium Series, vol 198; American Chemical Society: Washington, DC, 1982; p 151.
15. Taube, H.; Gould, E. S. *Acc. Chem. Res.* **1969**, *2*, 321.
16. Cox, L. T.; Collins, S. B.; Martin, D. S. *J. Inorg. Nucl. Chem.* **1961**, *17*, 383.
17. (a) Basolo, F.; Willis, P. H.; Pearson, R. G.; Wilkins, R. G. *J. Inorg. Nucl. Chem.* **1958**, *6*, 161. (b) Basolo, F.; Morris, M. L.; Pearson, R. G. *Discuss. Faraday Soc.* **1960**, *29*, 80.
18. (a) Erwin, D. K.; Geoffrey, D. K.; Gray, H. B. *J. Am. Chem. Soc.* **1977**, *99*, 3620. (b) Trogler, W. C.; Erwin, D. K.; Geoffrey, G. L.; Gray, H. B. *J. Am. Chem. Soc.* **1978**, *100*, 1160.
19. Chang, I-J.; Nocera, D. G. *J. Am. Chem. Soc.* **1987**, *109*, 4901.
20. Chang, I-J.; Nocera, D. G. *Inorg. Chem.* **1989**, *28*, 4309.
21. Partigianoni, C. M. Ph.D. Dissertation, Michigan State University, 1991.
22. Partigianoni, C. M.; Nocera, D. G. *Inorg. Chem.* **1990**, *29*, 2033.
23. Partigianoni, C. M.; Turro, C.; Shin, Y. K.; Motry, D. H.; Kadis, J.; Dulebohn, J. I.; Nocera, D. G. In *Mixed Valency Systems: Applications in Chemistry, Physics and Biology*; Prassides, K., Ed.; Kluwer: Netherlands, 1991; pp 91-106.
24. Partigianoni, C. M.; Turro, C.; Hsu, C.; Chang, I-J.; Nocera, D. G. In *Photosensitive Metal-Organic Systems: Mechanistic Principles and Recent Applications*; ACS Symposium Series, Reidel: Amsterdam, 1992; pp 0000.
25. (a) Cotton, F. A.; Mott, G. N. *J. Am. Chem. Soc.* **1982**, *104*, 5978. (b) Cotton, F. A.; Powell, G. L. *J. Am. Chem. Soc.* **1984**, *106*, 3371. (c)

- Cotton, F. A.; Diebold, M. P.; O'Connor, C. J.; Powell, G. L. *J. Am. Chem. Soc.* **1985**, *107*, 7438. (d) Chakravarty A. R.; Cotton, F. A.; Diebold, M. P.; Lewis, D. B.; Roth, W. J. *J. Am. Chem. Soc.* **1986**, *108*, 971. (e) Agaskar, P. A.; Cotton, F. A.; Dunbar, K. R.; Falvello, L. R.; O'Connor, C. J. *Inorg. Chem.* **1987**, *26*, 4051. (f) Canich, J. M.; Cotton, F. A.; Dunbar, K. R.; Falvello, L. R. *Inorg. Chem.* **1988**, *27*, 804. (g) Cotton, F. A.; Daniels, L. M.; Dunbar, K. R.; Falvello, L. R.; O'Connor, C. J.; Price, A. C. *Inorg. Chem.* **1991**, *30*, 2509.
26. Hopkins, M. D.; Gray, H. B.; Miskowski, V. M. *Polyhedron* **1987**, *6*, 705.
27. Manning, M. C.; Trogler, W. C. *J. Am. Chem. Soc.* **1983**, *105*, 5311.
28. Miskowski, V. M.; Gray, H. B.; Hopkins, M. D. *J. Am. Chem. Soc.* **1992**, *31*, 2085.
29. Agaskar, P. A.; Cotton, F. A.; Fraser, I. F.; Manojlovic-Muir, L.; Muir, K. W.; Peacock, R. D. *Inorg. Chem.* **1986**, *25*, 2511.
30. Zhang, X.; Kozik, M.; Sutin, N.; Winkler, J. R. In *Electron Transfer in Inorganic, Organic, and Biological Systems*; Bolton, J. R.; Mataga, N.; McLendon, G., Eds.; Advances in Chemistry Series, American Chemical Society: Washington, DC, 1991; pp 247-264.
31. Winkler, J. R.; Nocera, D. G.; Netzel, T. L. *J. Am. Chem. Soc.* **1986**, *108*, 4451.
32. Chang, I-J., Ph.D. Dissertation, Michigan State University, 1988.
33. Cotton, F. A.; Daniels, L. M.; Dunbar, K. R.; Falvello, L. R.; O'Connor, C. J.; Price, A. C. *Inorg. Chem.* **1991**, *30*, 2509.
34. Agaskar, P. A.; Cotton, F. A.; Dunbar, K. R.; Falvello, L. R.; O'Connor, C. J. *Inorg. Chem.* **1987**, *26*, 4051.

35. (a) Cotton, F. A.; Powell, G. L. *J. Am. Chem. Soc.* **1984**, *106*, 3372.
(b) Cotton, F. A.; Diebold, M. P.; O'Connor, C. J.; Powell, G. L. *J. Am. Chem. Soc.* **1985**, *107*, 7438.
36. Canich, J. A. M.; Cotton, F. A.; Dunbar, K. R.; Falvello, L. R. *Inorg. Chem.* **1988**, *27*, 804.
37. Fanwick, P. E.; Harwood, W. S.; Walton, R. A. *Inorg. Chem.* **1987**, *26*, 242.
38. Saillant, R.; Hayden, J. L.; Wentworth, R. A. D. *Inorg. Chem.* **1967**, *6*, 1497.
39. Shaik, S.; Hoffman, R.; Fisel, R.; Summerville, R. H. *J. Am. Chem. Soc.* **1980**, *102*, 4555.
40. Cotton, F. A.; Walton, R. A. *Multiple Bonds Between Metals*; Wiley-Interscience: New York, 1982, p 221.
41. Zietlow, T. C.; Hopkins, M. D.; Gray, H. B. *J. Solid State Chem.* **1985**, *57*, 112.
42. Tolman, C. A. *Chem. Rev.* **1977**, *77*, 313.
43. Cotton, F. A.; Extine, M. W.; Felthouse, T. R.; Kolthammer, B. W. S.; Lay, D. G. *J. Am. Chem. Soc.* **1981**, *103*, 4040.
44. Cotton, F. A.; Daniels, L. A.; Powell, G. L.; Kahaian, A. I.; Smith, T. J.; Vogel, E. F. *Inorg. Chim. Acta* **1988**, *144*, 109.
45. Cotton, F. A.; Czuchajowska, J.; Luck, R. L. *J. Chem. Soc. Dalton Trans.* **1991**, 579.
46. Cotton, F. A.; Jennings, J. G.; Price, A. C.; Vidyasagan, K. *Inorg. Chem.* **1990**, *29*, 4138.
47. Luck, R. L.; Morris, R. H.; Sawyer, J. F. *Inorg. Chem.* **1987**, *26*, 2422.
48. Cotton, F. A.; Falvello, L. R.; James, C. A.; Luck, R. L. *Inorg. Chem.* **1990**, *29*, 4759.

49. Bakir, M.; Cotton, F. A.; Falvello, L. R.; Simpson, C. Q.; Walton, R. A. *Inorg. Chem.* **1988**, *27*, 4197.

CHAPTER III

THE DRIVING FORCE DEPENDENCE OF BIMOLECULAR PROTEIN ELECTRON TRANSFER: $^*Ru(L)_3^{2+}$ /CYTOCHROME *c* SYSTEM

A. BACKGROUND

Measurements of electron transfer rates in the Marcus inverted region¹ have been limited to systems where the donor/acceptor distance is fixed, such as those which are covalently-bound,² in frozen media,³ in electrostatic complexes of proteins,^{4,5} or in covalently-modified proteins.⁶ Only recently has inverted region electron transfer been observed for bimolecular reactions between an Ir_2 complex and a series of pyridinium acceptors.⁸ It is now possible to design series of donors and acceptors of varying driving forces for which electron transfer kinetics in the bimolecular inverted region can be readily observed. The necessary conditions include an electron transfer rate sufficiently small compared to the rate of diffusion and a moderate reorganization energy to allow easy access of the inverted region. From the known electron transfer properties of cytochrome *c*, we have designed a series excited state ET reactions with Ru diimine complexes in which the inverted region is observed. The bimolecular cytochrome *c* ET with small molecules is characterized by a reorganization energy of 0.8 – 1.0 V which

allows access of the inverted region, and the quenching of $\text{Ru}(\text{phen})_3^{2+}$ by the protein is of the order of $10^8 \text{ M}^{-1}\text{s}^{-1}$, which is similar to the estimated rate of diffusion.

Described in this Chapter are the photoinduced bimolecular ET rates between Ru diimine complexes in their metal-to-ligand charge transfer (MLCT) excited state and cytochrome *c* in its reduced and oxidized states. For the exemplary complex $\text{Ru}(\text{phen})_3^{2+}$ (phen = 1,10-phenanthroline) the MLCT lies 2.1 eV above the ground state and is both a powerful oxidant ($E^{*/+} = -0.87 \text{ V vs NHE}$) and reductant ($E^{*/-} = 0.79 \text{ V vs NHE}$),⁹ whereas the protein is easily reduced or oxidized depending on its initial redox state ($E^{\text{FeIII/II}} = 0.26 \text{ V vs NHE}$).¹⁰ Systematic variation of the substituents of the parent ligand or utilization of mixed-ligand complexes provides a wide variation of the excited state oxidation and reduction potentials,⁹ which in turn control the driving force of the $^*\text{Ru}^{\text{II}}/\text{cyt } c$ ET reaction. A pictorial representation of the ligands utilized in this study is shown in Figure 38. Since in all complexes the excited state is MLCT in character, they should interact in an analogous manner with the protein thus providing a means to follow the driving force dependence of the ET rates without disturbing other rate-controlling parameters.

The highly charged residues in cytochrome *c* induce an overall charge of +7.5 and +6.5 in the oxidized and reduced forms, respectively.¹⁰ The electron transfer rates between the Ru^{2+} complexes chosen for our driving force dependence and cytochrome *c* are purely bimolecular, since binding is severely impeded by electrostatic repulsion. Nonetheless, the redox-active center of the protein, the heme, has an exposed edge, which is solvent accessible and is known to accelerate the ET rates of inorganic complexes containing hydrophobic ligands such as those in the phenanthroline family.

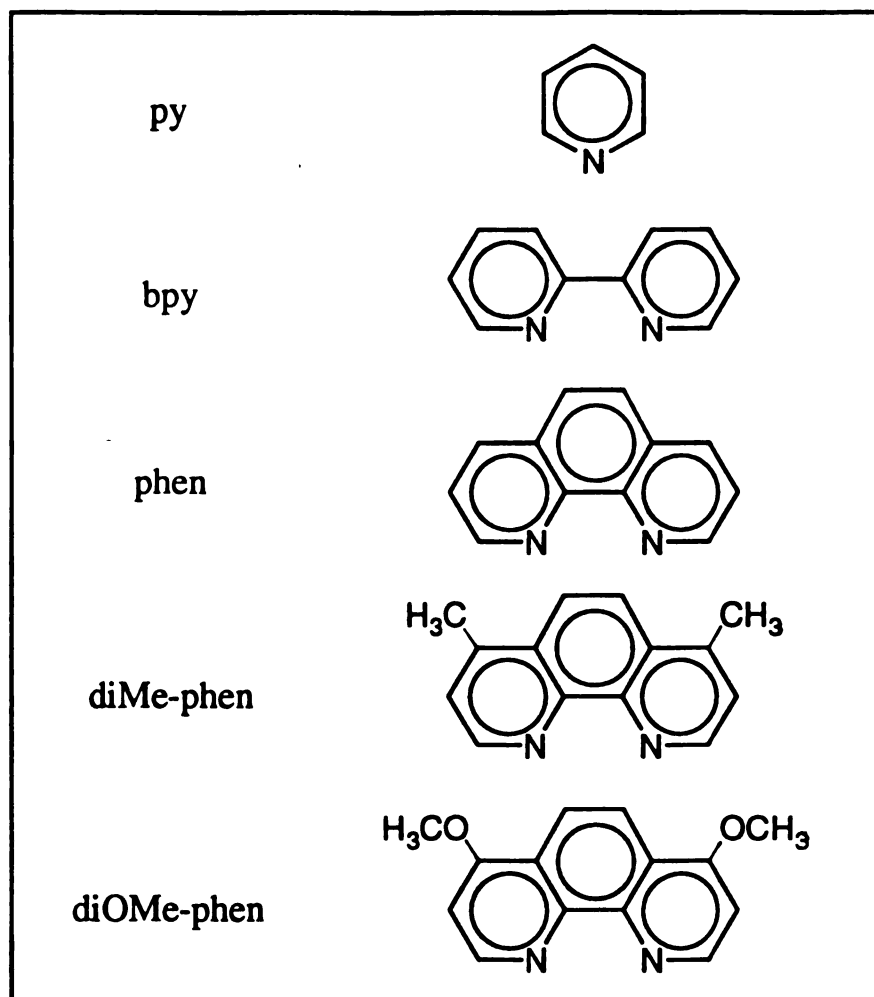


Figure 38. Schematic representation of the ligands utilized in the driving force dependence study of the ET rate.

B. EXPERIMENTAL METHODS

Horse heart cytochrome *c* Type VI was purchased from Sigma and was purified by standard methods.²² The oxidized protein, dissolved in $\mu = 10$ mM, pH = 7.4 phosphate buffer, was loaded onto a CM52 (Whatman) cation exchange column, and was subsequently eluted with the same buffer at a higher ionic strength ($\mu = 0.1$ M). Ferricytochrome *c* was reduced by addition of freshly prepared sodium ascorbate, or was fully oxidized with potassium ferrocyanide.²³ The protein was then eluted from a Sephadex LH-50 column with $\mu = 0.1$ M, pH = 5 ammonium bicarbonate buffer, to allow separation of the reducing or oxidizing agents. After the eluent was frozen with a dry ice/acetone bath, the water and buffer were removed under vacuum (10^{-3} torr). All manipulations of ferrocyanochrome *c* were performed under N_2 , and the oxidation state was carefully monitored utilizing the characteristic absorption features. The reduced heme possesses a sharp band at 550 nm ($\epsilon = 27.7$ mM⁻¹cm⁻¹),²⁴ whereas in the oxidized state a broad feature at 530 nm ($\epsilon = 10.1$ mM⁻¹cm⁻¹) is observed.²⁵

The ligands, pyridine (py), bipyridine (bpy), 1,10-phenanthroline (phen), 4,7-dimethyl-1,10-phenanthroline (diMe-phen), and 4,7-dihydroxy-1,10-phenanthroline (diOH-phen), and 4,7-di(*p*-phenylsulfonate)-1,10-phenanthroline (BPS) were purchased from Aldrich. The ligand 4,7-dimethoxy-1,10-phenanthroline (diOMe-phen) was synthesized by reported methods, where 4,7-dichloro-1,10-phenanthroline (prepared from diOH-phen)²⁶ was treated with NaOMe in benzene.²⁷ Characterization was conducted by ¹H NMR [phen arom.: 8.90 ppm (Area = A = 5.66), 8.22 ppm (A = 6.11), 7.25 ppm (A = 5.80); OCH₃: 4.15 ppm (A = 19.6)], melting point (200 °C), and elemental analysis (found: C = 64.6%, H = 4.2 %, N =

10.7%, O = 8.7%; calc.: C = 70.0%, H = 5.0 %, N = 11.7%, O = 13.3%). The Ru^{II} complexes were prepared by reported techniques.^{9,28} Typically RuCl₃ was refluxed in ethanol/water (80/20) with a six equivalents of ligand, L, to form the red/orange Ru^{II}(L)₃²⁺ complexes. Ru(bpy)₂(py)₂²⁺ was prepared in a similar manner, where Ru(bpy)₂Cl₂ (purchased from Aldrich) was refluxed with a four-fold molar excess of py ligand in ethanol/water. After evaporation of the solvent, the product was readily precipitated from acetone with ether. The Ru complexes were characterized by comparison with their known electronic absorption and emission spectra, emissive lifetime, and redox potentials.⁹

The lifetime quenching measurements were performed with an instrument that has previously been described in detail.²⁹ The luminescence decay was monitored at the emission maximum of the Ru complex, typically in the 600 – 630 nm range, following 532 nm, 8 ns excitation. Stock solutions (25 or 50 ml) containing 6×10^{-5} M of each Ru complex were prepared in $\mu = 0.1$ M, pH = 7.4 phosphate buffer. The protein was dissolved in 200 μ l of stock solution and placed in a 1 mm pathlength cuvette equipped with a stopcock; deoxygenation was attained by bubbling N₂ for ~5 min and closing the stopcock prior to the lifetime measurement. The protein concentration was varied by addition of known volumes of stock solution with a 250 μ l syringe to the initial 200 μ l, followed by deoxygenation and lifetime measurement. The concentration of cytochrome *c* was determined prior to each lifetime measurement from the absorbance at either 530 nm or 550 nm, depending on the protein's oxidation state, and was corrected for the absorbance of the Ru complex at each wavelength (typically 0.05 – 0.07). In this manner the concentration of the Ru

complexes remained constant and at least two orders of magnitude smaller than the protein concentration, as required to perform our kinetic analysis.

C. THEORY

Marcus predicted that as the driving force of the electron transfer (ET) reaction increases, the rate will initially increase, reach a maximum, and then decrease.¹ From the transition state formulation with parabolic potential energy surfaces the ET rate is given by¹

$$k_{\text{et}} = \nu_{\text{et}} \exp\left\{\frac{-(\Delta G + \lambda)^2}{4\lambda k_{\text{B}} T}\right\} \quad (11)$$

where ν_{et} represents the frequency of crossing the transition state, ΔG is the driving force, and λ is the reorganization energy. It can be readily observed from eq 11 that the ET rate will be fastest when $-\Delta G = \lambda$, as shown in Figure 39. In bimolecular reactions if the ET rate is much faster than the rate of diffusion, k_{diff} , then the observation of the inverted behavior will be obscured by the limiting kinetics (Figure 39b).^{11,12} The interaction between the reactant and product potential energy surfaces in the three regimes predicted by Marcus, $-\Delta G > \lambda$, $-\Delta G = \lambda$, and $-\Delta G < \lambda$, are depicted in Figure 40, where the reaction passes through the activationless state between the normal and inverted regions. The ΔG range where the rate decreases with increasing driving forces is referred to as the inverted region, and it is evident from Figure 39 that as either the ET rates or λ become larger, moving the curve up or to the right, respectively, the inverted region will move to higher driving forces.

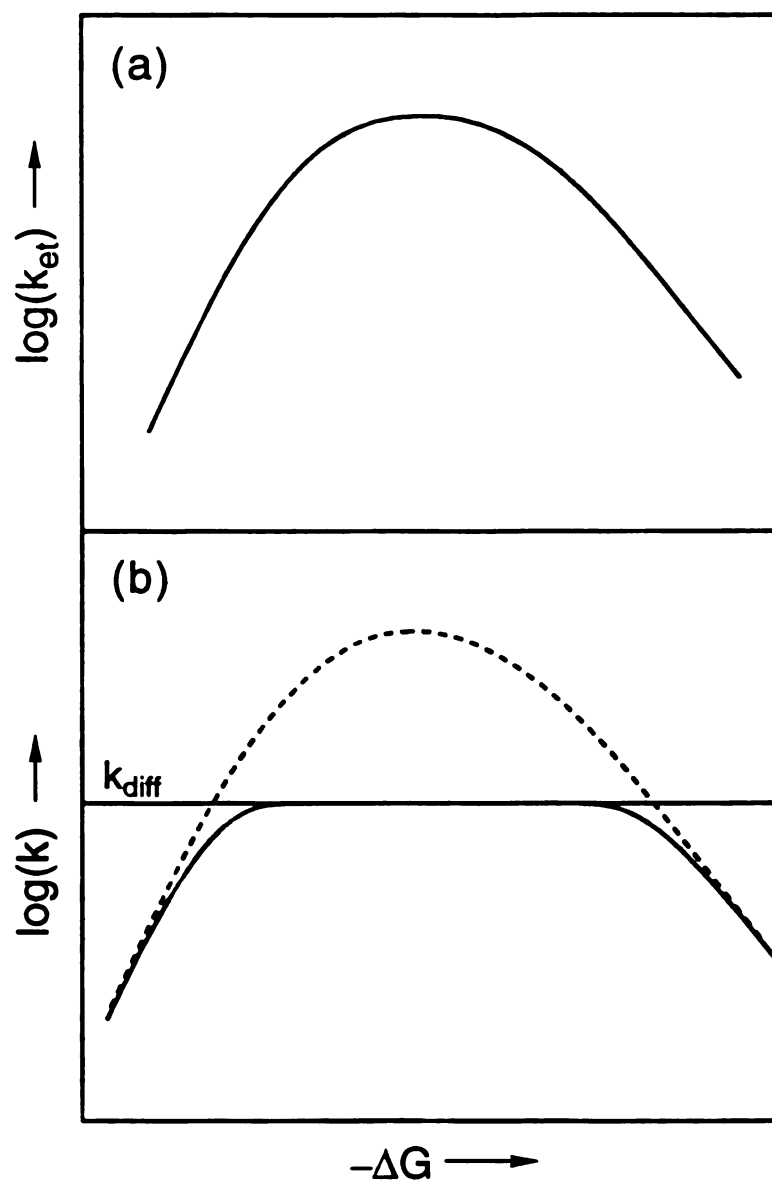


Figure 39. Driving force dependence of the ET rate in (a) fixed-distance systems and (b) diffusion controlled reactions.

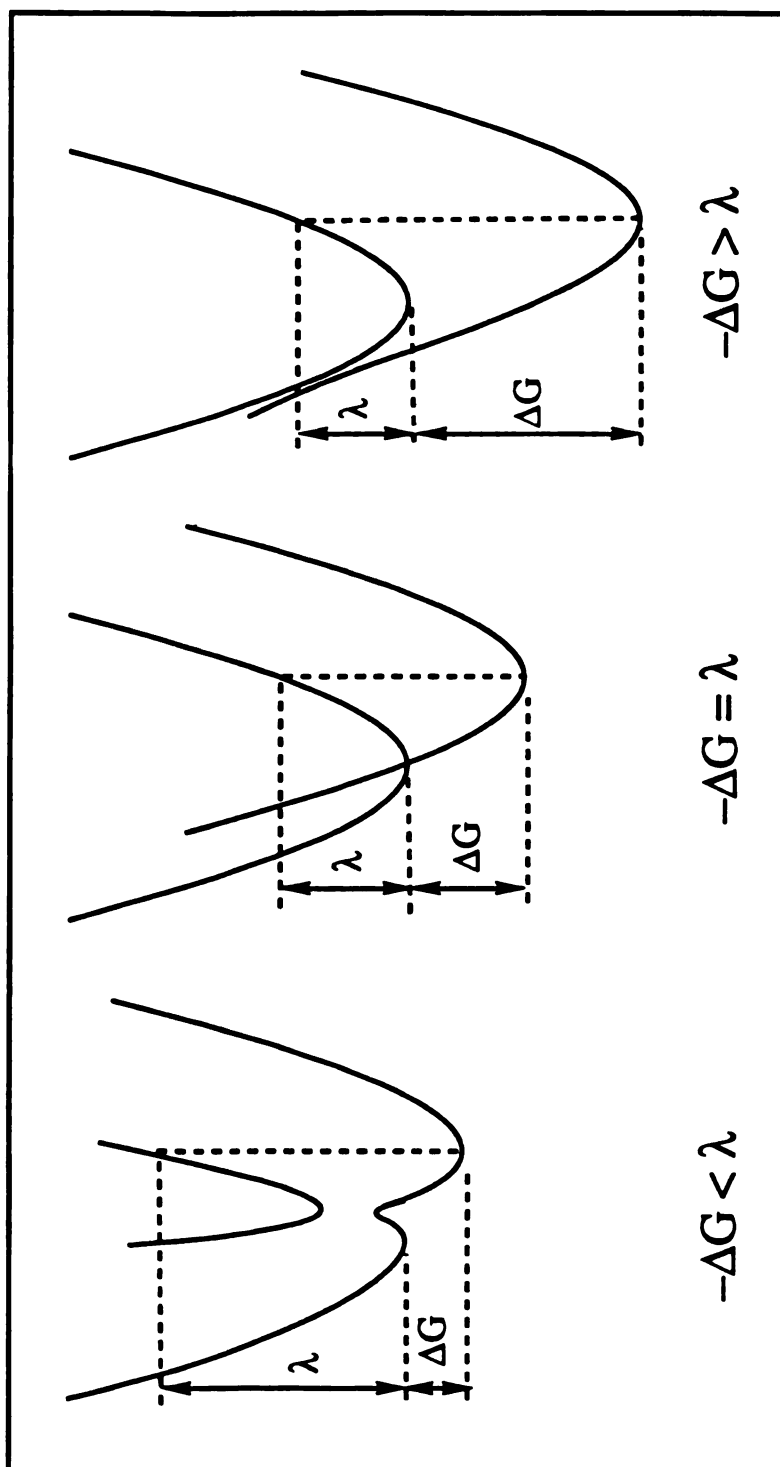


Figure 40. Schematic representation of the normal ($-\Delta G < \lambda$), activationless ($-\Delta G = \lambda$), and inverted ($-\Delta G > \lambda$) regimes of electron transfer (see text).

The electron transfer rates presented in this Chapter were measured by emissive lifetime quenching and determined from plots of the emissive lifetime as a function of protein concentration, which follow the Stern-Volmer relation¹³

$$\frac{\tau_0}{\tau} = 1 + k_{\text{obs}} \tau_0 [\text{Cyt } c] \quad (12)$$

where τ_0 and τ represent the lifetimes of the complex in the absence and presence of cytochrome *c*. The observed ET rate, k_{obs} , can be extracted from the slope of plots of τ_0/τ vs protein concentration. Since the ET reaction in this case is a bimolecular process, k_{obs} , depends on the rate of diffusion, k_{diff} , and the bimolecular ET rate, k_{act} , which are related by^{14,15}

$$\frac{1}{k_{\text{obs}}} = \frac{1}{k_{\text{diff}}} + \frac{1}{k_{\text{act}}} \quad (13)$$

The rate of diffusion can be estimated by¹⁶⁻¹⁸

$$k_{\text{diff}} = \frac{4\pi ND}{1000} \left[\int_{r=\sigma}^{\infty} dr g_e(r) r^{-2} \right]^{-1} \quad (14)$$

where N is the Avogadro's number, r is the center-to-center separation between reactants, $g_e(r)$ is the radial distribution function, σ represents the distance of closest contact, and D is the sum of the diffusion coefficients of the reactants, $D_A + D_B$. For reactant A, the diffusion coefficient is given by¹⁸

$$D_A = \frac{k_B T}{6\pi r_A \eta} \quad (15)$$

where k_B is Boltzman's constant, T is the temperature, r_A is the reactant's radius, and η is the viscosity of the solvent. The radial distribution function, $g_e(r)$, represents the forces between the reactants at distance r , and can be expressed as^{14,15}

$$g_e(r) = \exp\{ -U(r)/k_B T \} \quad (16)$$

where $U(r)$ is the attraction or repulsion energy of the reactants. In cases where both reactants are charged, electrostatic forces are strongest and therefore $U(r)$ for two spheres can be expressed as¹⁶

$$U(r) = \frac{Z_1 Z_2 e^2}{D_S r (1 + \beta_{DH} r \sqrt{\mu})} \quad (17)$$

where Z_1 and Z_2 are the charges on each reactant, e is the charge on the electron, D_S is the static dielectric constant of the solvent, and μ the ionic strength. From the Debye-Huckel formalism, β_{DH} , is given by¹⁶

$$\beta_{DH} = \left[\frac{8\pi N e^2}{1000 D_S k_B T} \right]^{1/2} \quad (18)$$

The bimolecular ET rate, k_{act} , involves the reactants coming sufficiently close for the ET event to take place, and can be written as the product $K(r)k(r)$, where $K(r)$ is the equilibrium constant for the reactants to form a reactive complex at a distance r and $k(r)$ is the ET rate at that separation. This leads to the expression^{14,15}

$$k_{act} = \frac{4\pi N}{1000} \int_{r=\sigma}^{\infty} dr g_e(r) k(r) r^2 \quad (19)$$

where $k(r)$ can be expressed as^{2,3,19}

$$k_{et}(r) = \frac{2\pi}{h} \left[\frac{1}{\lambda_o k_B T} \right]^{1/2} |V|^2 \sum_{w=0}^{\infty} \frac{e^{-S} S^w}{w!} \exp \left\{ \frac{-(\lambda_o + \Delta G + wh\nu)^2}{4\lambda_o k_B T} \right\} \quad (20)$$

where $S = \lambda_v/h\nu$, λ_v and λ_s are the inner vibronic and solvent reorganization energies, respectively, ν is the high energy vibrational frequency associated with the acceptor, V is the electronic coupling, ΔG the driving force, and w the density of vibronic states of the acceptor. This expression is more elaborate than that derived from transition state theory (eq 11), since it accounts for ET to excited vibrational states of the acceptor, which becomes important at high driving forces. The value of the solvent reorganization energy can be estimated from the two-sphere model^{12,14,15}

$$\lambda_s = (\Delta e)^2 \left[\frac{1}{2r_A} + \frac{1}{2r_B} - \frac{1}{r} \right] \left[\frac{1}{D_{op}} - \frac{1}{D_s} \right] \quad (21)$$

where r_A and r_B are the reactants' radii, and D_{op} is the optical dielectric constant of the solvent. In cytochrome *c* the transition between redox states has been found to involve a 0.2 eV reorganization in the protein matrix, which can be directly added to the solvent reorganization, λ_s .^{20,21} The total driving force, ΔG , includes the work required to bring the reactants together, w_r , and that to separate the products, w_p ^{12,14,15}

$$\Delta G = \Delta G^0 + w_r - w_p \quad (22)$$

where w_r and w_p are given by eq 17 and ΔG^0 can be calculated from the electrochemical reduction and oxidation potentials of the acceptor and

donor, respectively. The electronic coupling, V , contains a distance dependence term which can be expressed as^{12,14,15,19}

$$V = V^0 \exp[-\beta/2(d - d_0)] \quad (23)$$

where d_0 is the contact distance, which is 3 Å allowing for electronic clouds,¹² and d is the edge-to-edge distance between donor and acceptor. V^0 and β are the electronic coupling matrix element and the damping factor, respectively.

D. RESULTS AND DISCUSSION

The lifetimes and excited state redox potentials of the series of positively charged Ru^{II} complexes are listed in Table XI. As is evident from Table XI, the electron withdrawing or donating abilities of the substituents on the parent ligand, phen, provide a wide range of redox potentials. The bimolecular ET rates for each complex with *ferro*- and *ferricytochrome c* have been measured by the lifetime quenching method described above and are listed in Table XII, along with the driving force for each reaction. Exemplary Stern-Volmer plots (eq 12) for the quenching of the MLCT excited state of Ru(diMe-phen)₃²⁺ by both redox states of the protein are shown in Figure 41. As expected, the data points follow a linear distribution and exhibit the proper intercept of 1. Although it is possible that the lifetime quenching is due in part or fully to energy transfer, transient absorption studies have shown the distinct spectral profile of the reduced heme. The transient absorption spectrum of cytochrome *c* collected in the presence of

Table XI. Emission Lifetimes and Excited State Redox Potentials of the Ru^{II} Complexes Utilized in this Study.

| Complex | τ_0 (μs) | $E^{*/+}$ (V) ^a | $E^{*/-}$ (V) ^a |
|--|----------------------------|----------------------------|----------------------------|
| Ru(diOMe-phen) ₃ ²⁺ | 1.14 | - 1.20 | 0.94 |
| Ru(diMe-phen) ₃ ²⁺ | 1.76 | - 1.03 | 0.67 |
| Ru(phen) ₃ ²⁺ | 1.18 | - 0.87 | 0.79 |
| Ru(bpy) ₂ (py) ₂ ²⁺ | 1.13 | - 0.56 | 1.02 |

^aPotentials vs NHE (Ref. 9).**Table XII.** Driving Force and Observed Rates for the ET Reactions Between the MLCT Excited State of Ru^{II} Complexes and Cytochrome *c* in the Oxidized (Fe^{III}) and Reduced (Fe^{II}) States.

| Complex | Cyt. <i>c</i> | $-\Delta G^0$ (V) | k_{obs} (M ⁻¹ s ⁻¹) |
|--|-------------------|-------------------|---|
| Ru(diOMe-phen) ₃ ²⁺ | Fe ^{III} | 1.46 | 2.08×10^8 |
| Ru(diMe-phen) ₃ ²⁺ | Fe ^{III} | 1.29 | 2.10×10^8 |
| Ru(phen) ₃ ²⁺ | Fe ^{III} | 1.13 | 2.65×10^8 |
| Ru(bpy) ₂ (py) ₂ ²⁺ | Fe ^{III} | 0.82 | 3.45×10^8 |
| Ru(bpy) ₂ (py) ₂ ²⁺ | Fe ^{II} | 0.76 | 6.24×10^8 |
| Ru(diOMe-phen) ₃ ²⁺ | Fe ^{II} | 0.68 | 5.68×10^8 |
| Ru(phen) ₃ ²⁺ | Fe ^{II} | 0.53 | 4.36×10^8 |
| Ru(diMe-phen) ₃ ²⁺ | Fe ^{II} | 0.41 | 2.84×10^8 |

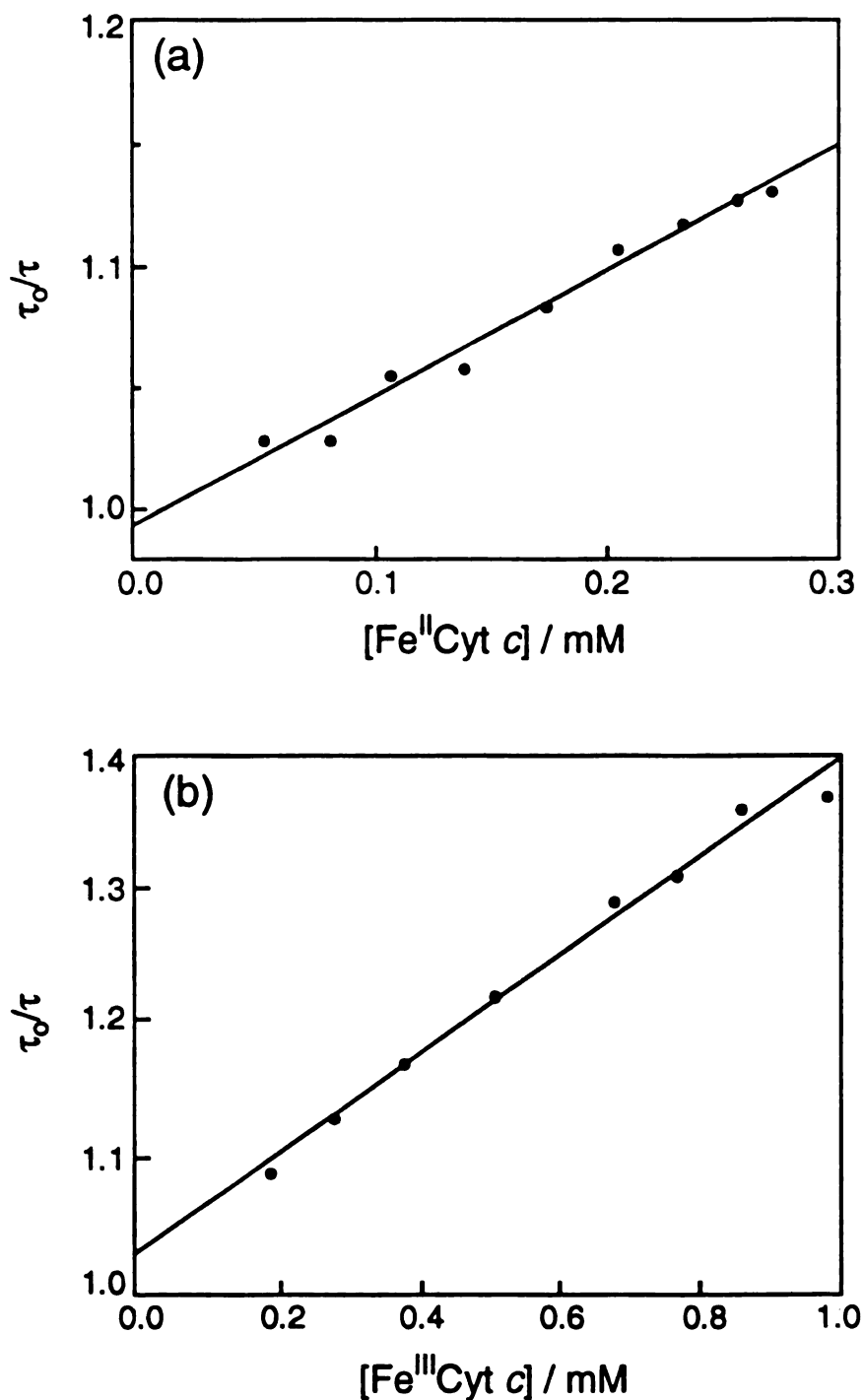


Figure 41. Stern-Volmer plots of the quenching of 6×10^{-5} M solutions of $\text{Ru}(\text{diMe-phen})_3^{2+}$ in pH = 7, $\mu = 0.1$ M phosphate buffer by (a) ferrocyanide *c* and (b) ferricyanide *c*, showing the linear fit through the data points.

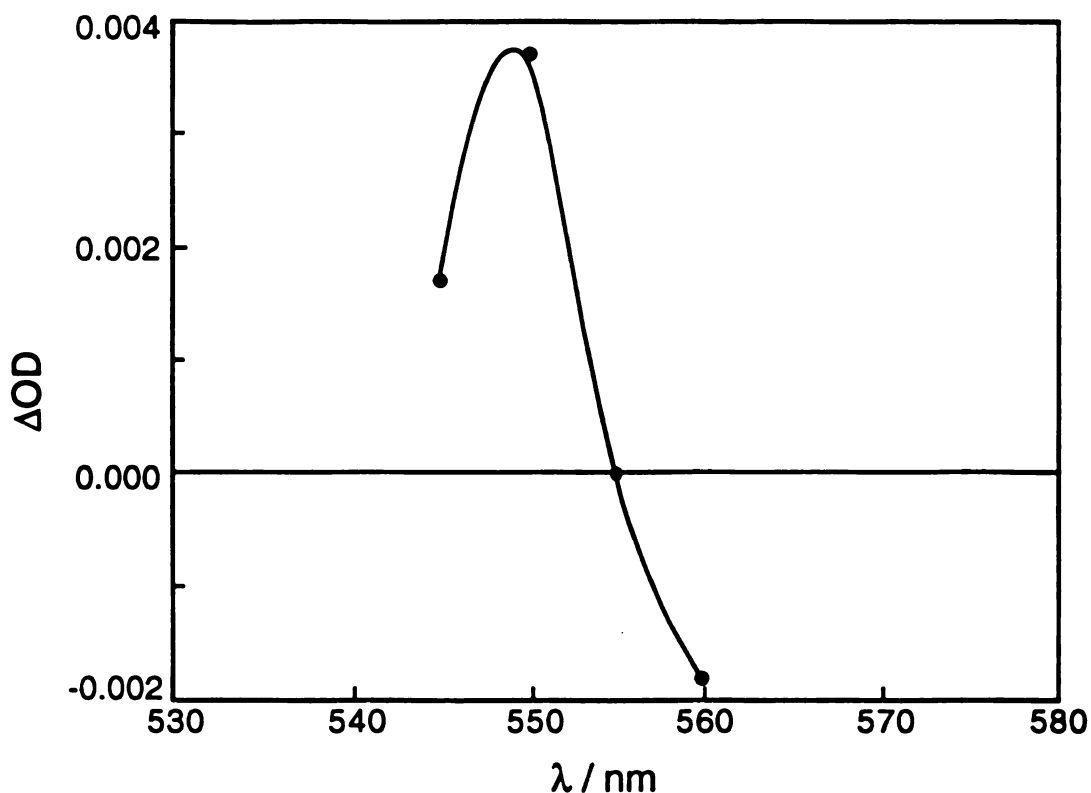


Figure 42. Transient absorption spectrum obtained from a $\mu = 0.1$ M, pH = 7.4 phosphate buffer solution of 1×10^{-3} M Ru(diMe-phen) $_3^{2+}$ and 1×10^{-3} M *ferr*-cytochrome *c* following 532 nm, 10 ns excitation.

Ru(diMe-phen) $_3^{2+}$ following 532 nm excitation is shown in Figure 42. The signal generated was too weak to determine the decay lifetime, but its disappearance was in the expected time range, which is in agreement with electron transfer quenching exclusively.

The semi-log plots of k_{obs} vs ΔG° are shown in Figure 43 for the two systems, $^* \text{Ru}^{\text{II}}/\text{Fe}^{\text{II}}\text{cyt } c$ and $^* \text{Ru}^{\text{II}}/\text{Fe}^{\text{III}}\text{cyt } c$. It is apparent from the data points that although the rates are near the diffusion limit, there is a significant contribution from k_{act} to the rate (eq 13). The observed ET

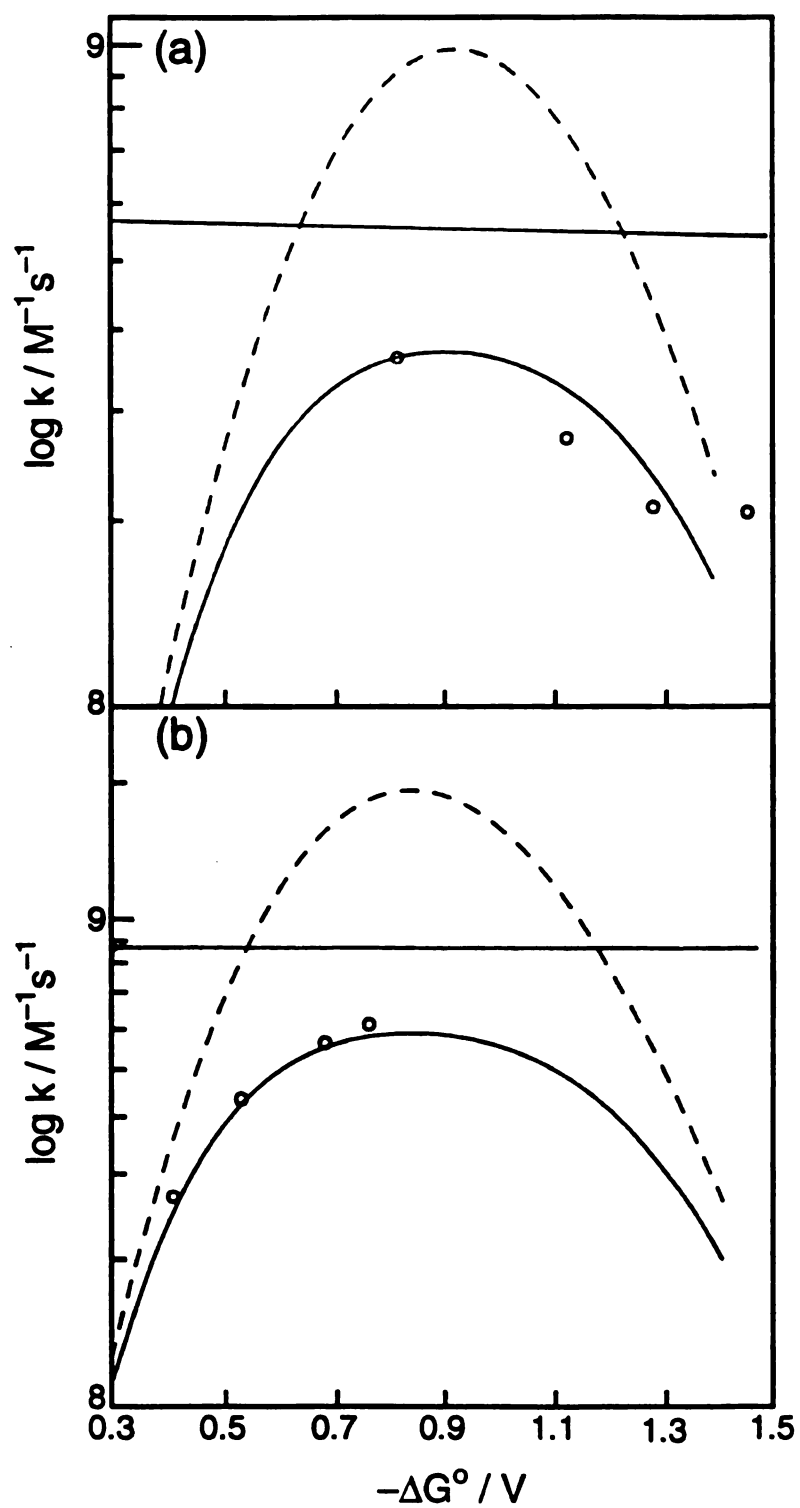


Figure 43. Plots of the electron transfer rates of Ru^{II} complexes with (a) Fe^{III} cyt. c and (b) Fe^{II} cyt. c, with their respective calculated k_{obs} (solid curve), k_{act} (dashed curve) rates, and diffusion limits.

rates lie near the estimated rates of diffusion calculated using Equations 14 – 18 at closest contact ($\sigma = 23.1 \text{ \AA}$, estimated from the known protein radius, 16.6 \AA ,¹⁰ and assuming an average radius of 6.5 \AA for all the Ru complexes³⁰), with $T = 298 \text{ K}$, $\eta = 0.89 \text{ g cm}^{-1}\text{s}^{-1}$, and $D_s = 78.5$. These values yield k_{diff} values of $5.4 \times 10^8 \text{ M}^{-1}\text{s}^{-1}$ and $8.8 \times 10^8 \text{ M}^{-1}\text{s}^{-1}$ for the $^*\text{Ru}^{\text{II}}/\text{Fe}^{\text{III}}\text{-cyt. } c$ and $^*\text{Ru}^{\text{II}}/\text{Fe}^{\text{II}}\text{-cyt. } c$ systems, respectively, with $\beta_{\text{DH}} = 3.29 \times 10^6 (\text{mol}^{-1}\text{m})^{1/2}$ from Equation 18. The order of magnitude of the calculated rate of diffusion is in agreement with others observed for like-charges in solution.³¹

The solid curves through the data points represent the calculated observed rate (Equations 12 – 23) as a function of driving force at closest contact with the following parameters: $D_{\text{op}} = 1.77$, $\lambda_v = 0.2 \text{ eV}$,²⁰ $v = 1372 \text{ cm}^{-1}$,³² and $w = 6$.³³ The electronic coupling, V , was the *only* parameter varied to fit all the experimental data with the calculated rates, and the value that best fit the data points was $V = 11.4 \text{ cm}^{-1}$. The ET rates for both systems, $^*\text{Ru}^{\text{II}}/\text{Fe}^{\text{II}}\text{cyt } c$ and $^*\text{Ru}^{\text{II}}/\text{Fe}^{\text{III}}\text{cyt } c$, were calculated utilizing the same parameters, with exception of the charges on the reactants and products, and therefore different k_{diff} .³⁴ The agreement between the calculated curves and the observed points is excellent for both systems. The calculated values of k_{act} (dashed line) for both systems, the electron transfer rate without the correction for k_{diff} (Equation 13), are also shown in Figure 43. A value of $V^0 = 228 \text{ cm}^{-1}$ is obtained from Equation 13 with $V = 11.4 \text{ cm}^{-1}$, $\beta = 1.2 \text{ \AA}^{-1}$,^{12,35} and $d = 8 \text{ \AA}$, where the ET distance was estimated by assuming that the heme lies 5 \AA from the surface of the protein and 3 \AA are assumed at the interface.³⁶ This value of V^0 is comparable to the 200 cm^{-1} utilized by Gray for cytochrome *c*.³⁷

The bimolecular ET rates were also measured for two neutral complexes, $\text{Ru}^{\text{II}}(\text{phen})_2(\text{bps})$ and $\text{Ru}^{\text{II}}(\text{phen})_2(\text{CN})_2$, and one which is negatively charged, $\text{Ru}(\text{bps})_3^{4-}$ with *ferricytochrome c*, whose Stern-Volmer plots are shown in Figure 44. The observed rates and driving force for ET are listed in Table XIII, along with the calculated rates of diffusion, the complexes' radii, and the calculated electronic coupling, V . For the negatively charged complex, a limiting ET rate is observed high protein concentrations. This is manifested in the non-linearity of the Stern-Volmer plot, which corresponds to the formation of a 1:1 electrostatic complex.

Table XIII. Driving Forces, Calculated Values of the Rates of Diffusion and Electronic Coupling, and Observed Bimolecular Electron Transfer Rates between Neutral and Negative Complexes and Fe^{III} cytochrome *c*.

| Complex | ΔG (V) ^a | k_{obs} ($\text{M}^{-1}\text{s}^{-1}$) | r (\AA) ^b | k_{diff} ($\text{M}^{-1}\text{s}^{-1}$) | V (cm^{-1}) |
|---|-----------------------------|---|-----------------------------------|--|--------------------------|
| $\text{Ru}(\text{phen})_2(\text{bps})$ | 1.14 | 4.00×10^8 | 6.7 | 1.22×10^{10} | 0.47 |
| $\text{Ru}(\text{phen})_2(\text{CN})_2$ | 1.34 | 8.36×10^8 | 6.0 | 1.32×10^{10} | 0.71 |
| $\text{Ru}(\text{bps})_3^{4-}$ | 1.27 | 1.15×10^9 | 7.2 | 1.29×10^{11} | 0.36 |

^aCalculated from the redox properties of each excited state (Ref. 31).

^bCalculated from standard bond lengths as the average of the distance from the central Ru to the edge of each ligand.

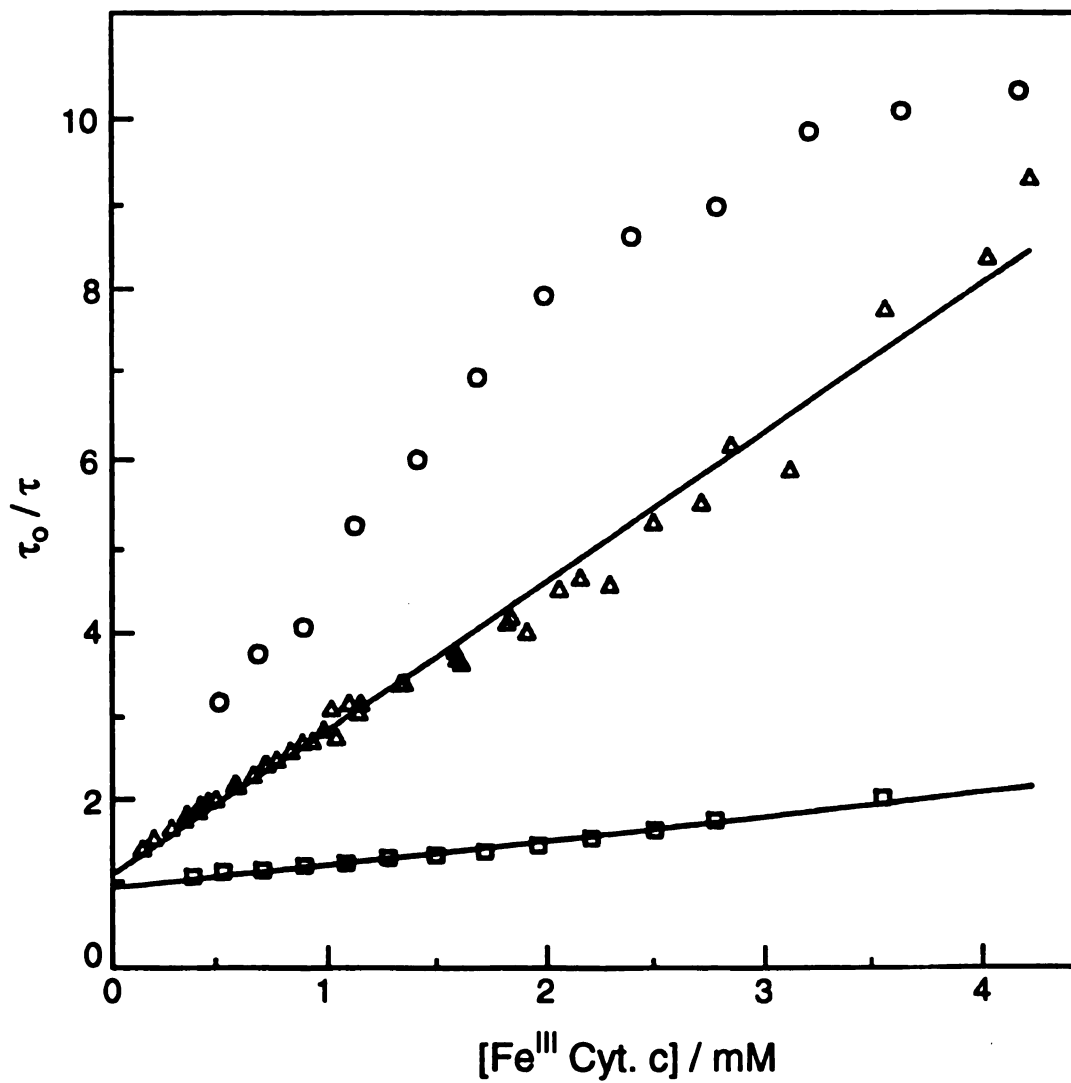


Figure 44. Stern-Volmer plots of $\text{Ru}(\text{bps})_3^{4-}$ (○), $\text{Ru}(\text{phen})_2(\text{bps})$ (Δ), and $\text{Ru}(\text{phen})_2(\text{CN})_2$ (□).

The value of the electronic coupling, V , calculated with the positively-charged reactants is larger than those found in protein-protein and substituted protein systems (Table XIV), but comparable to through-bond inorganic and organic systems at comparable separations (Table XV). It is well established that anions and cations react at different locations on the protein's surface, guided by the local charges on nearby residues.³⁸⁻⁴⁰ Positively charged reactants are known to be accelerated by modification of Lys27, whereas the reactivity of negative complexes is attenuated when the positive charge on Lys72 is neutralized.^{38,39} The reactivity of negative complexes at locations near Lys72 has also been demonstrated with NMR methods.⁴⁰ The different reactive sites for small negative and positive molecule and biological redox partners are schematically shown in Figure 45.

Recent calculations of the electronic coupling between the heme and different residues of the protein, taking into account the number of covalent and hydrogen bonds, as well as through space gaps, have shown that the coupling at Lys27, where cations react, is an order of magnitude greater than that at the anionic reaction site, Lys72.³⁵ These calculations have been tested experimentally by covalently binding Ru complexes to several residues of the protein.⁴¹ Other studies have shown that complexes containing hydrophobic ligands, such as phen, react much faster with cytochrome *c* than those with hydrophilic ligands.^{10,42,43} This effect is believed to be due to direct interaction of the ligand with the heme, by its penetration into the hydrophobic heme crevice. These π interactions have been shown to accelerate the ET rate by one order of magnitude.^{42,43} This is supported by studies of flavins and heme proteins, where the rate was slower when free hemin was utilized in place of the proteins.⁴⁴ These studies point

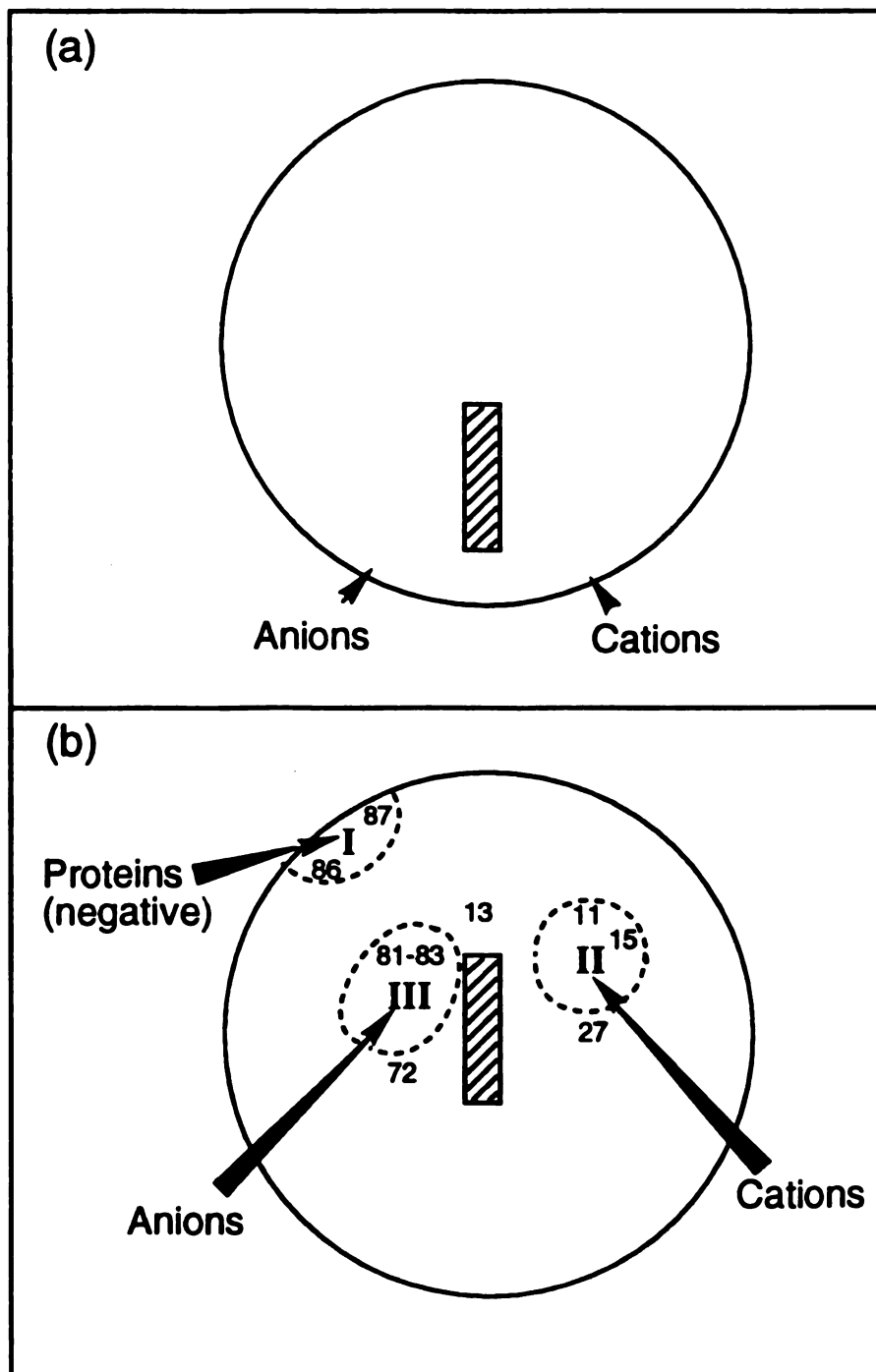


Figure 45. Schematic diagram cytochrome c viewed from the (a) top and (b) front. The dashed lines indicate regions I, II, and III, with some approximate residue numbers, where proteins, small anions, and cations react with the protein, respectively.

Table XIV. Comparison of reorganization energy and electronic coupling in ET reactions involving cytochrome *c*.

| System ^a | λ (eV) | d (Å) | V (cm ⁻¹) | Ref. |
|---|----------------|---------------|-------------------------|------|
| Co(C)–Glu66/69–cyt <i>c</i> | 2.1 | 14.5 | | 36 |
| Ru ^{III} (py)(NH ₃) ₄ –His33–*Zn–cyt <i>c</i> | 1.1 | 11.7 | 0.12 | 6b |
| Ru ^{II} (py)(NH ₃) ₄ –His33–*Zn–cyt <i>c</i> | 1.2 | 11.7 | 0.09 | 6b |
| Ru ^{II} (NH ₃) ₅ –His33–cyt <i>c</i> | 1.2 | 11.1 | 0.03 | 20 |
| Ru ^{III} (L)(NH ₃) ₄ –His39–cyt <i>c</i> | | 12.3 | 0.24 | 45 |
| Ru ^{II} (py)(NH ₃) ₄ –His62–cyt <i>c</i> | | 14.8 | 0.01 | 20 |
| *Ru(bpy) ₂ (im)–His39–cyt <i>c</i> | | 12.3 | 0.11 | 41 |
| *Ru(bpy) ₂ (im)–His33–cyt <i>c</i> | | 11.1 | 0.097 | 41 |
| *Ru(bpy) ₂ (im)–His62–cyt <i>c</i> | | 8.4 | 0.057 | 41 |
| *Ru(bpy) ₂ (im)–His72–cyt <i>c</i> | | 14.8 | 0.0060 | 41 |
| cyt <i>c</i> /cyt <i>c</i> | 0.7 | 8.9 | | 46 |
| cyt <i>b</i> ₅ /cyt <i>c</i> | 0.8 | 8 | 0.04 | 4a |
| cyt <i>c</i> peroxidase/cyt <i>c</i> | 1.4 | 16 <i>c/c</i> | | 4c |
| plastocyanin/Zn–cyt <i>c</i> | 1.0 | | | 47 |
| (M–uroporphyrin/M'–cyt <i>c</i>)* ^{CS} | 1.0 | ~ 8 | 0.090 | 5b |
| (M–uroporphyrin/Zn–cyt <i>c</i>) ^{CR} | 0.7 | ~ 8 | 0.088 | 5b |
| porphyrins + cyt <i>c</i> | 0.9 | ~ 8 | 1.84 | 7b |
| flavin semiquinones* + cyt's | 1.0 | ~ 8 | | 48 |

^aFor a detailed description of each system see its listed reference.

Table XV. Comparison of electronic coupling in ET reactions of organic and inorganic donor/acceptor systems.

| System | d (Å) | V (cm ⁻¹) | V _{8Å} (cm ⁻¹) ^a | Ref. |
|---|-------|-----------------------|--|------|
| Porphyrin–Quinone | 5.5 | 30 | 10.5 | 49 |
| R–Bz + (CN) _{2,3} An | 6 – 8 | 10.8 | 7.1 | 50 |
| Biphenyl–Sp–Acceptor | 10.3 | 6.2 | 16.3 | 2a |
| Os ^{II} –Pro ₁ –Ru ^{III} | 7.2 | 4.3 | 3.1 | 51 |
| Os ^{II} –Pro ₂ –Ru ^{III} | 9.8 | 2.2 | 4.6 | 51 |
| Os ^{II} –Pro ₃ –Ru ^{III} | 13.1 | 0.8 | 6.8 | 51 |

^aCalculated for distance of 8 Å using $\beta/2=0.42 \text{ Å}^{-1}$ (Ref. 35)).

to the direct reactivity with the heme of cytochrome *c* at its exposed, and perhaps π stabilization of the precursor complex by the protein matrix. This type of stabilization is expected to be absent when the ligands are hydrophilic, as is the case in our negative and neutral complexes. The extent of penetration of Ru ligands in the heme crevice is currently being tested by molecular modeling, utilizing the crystal structure coordinates of the protein.

The contribution from the electrostatic work terms ($w_r - w_p$) to the value of ΔG (Equation 12) was calculated to be -0.034 V and $+0.028 \text{ V}$ for the Ru^{II}/Fe^{II}cyt. *c* and Ru^{II}/Fe^{III}cyt. *c* systems, respectively. The calculated curves reach a maximum when the term in the exponent equals zero in Equation 20, and therefore when $(\lambda_S + \Delta G^0 + w_r - w_p + wh\nu) = 0$. Therefore from the numerical maximum of the calculated curves and the known values of ΔG^0 , $wh\nu$, and $(w_r - w_p)$, the values of λ_S for both systems can be

calculated. The reorganization energies, λ_s , obtained in this manner are 0.87 eV and 0.88 eV for Ru^{II}/Fe^{II}cyt. *c* and Ru^{II}/Fe^{III}cyt. *c*, respectively. These values are in excellent agreement with the values listed in Table XIV for ET reactions involving cytochrome *c*. The electrostatic nature of the ET reaction, however, obscures the value of λ , since the coulombic repulsion shifts the maximum of the observed rates when plotted vs ΔG° . It is thus important to take these interactions into consideration when estimating reorganization energy values from such reactions.

Our method of calculating the bimolecular electron transfer rates should also provide satisfactory results in other bimolecular systems. This is the case for data reported by McLendon for the bimolecular ET quenching rates of triplet excited state of Zn-substituted cytochrome *c* by viologens (V²⁺) of varying reduction potentials. Figure 46 shows the calculated values of k_{obs} (solid curve) and k_{act} (dashed curve) utilizing Equations 13 – 23, along with the experimental data points.⁵² The calculation was performed with all the same parameters utilized for the Ru complexes above, except for average radius the acceptors (3.5 Å). With this average radius and the electrostatic charges on the protein and acceptors taken as 6.5 and 2, respectively, yields $k_{\text{diff}} = 7.09 \times 10^8 \text{ M}^{-1}\text{s}^{-1}$. As is evident from Figure 46, there is little contribution from the rate of diffusion to the observed rates indicating that our model for the calculation of k_{act} is adequate (Equation 14). Similar electronic coupling between McLendon's system and ours is not surprising since the aromatic, planar V²⁺ acceptors and the Ru²⁺ complexes are expected to interact at the same location on the protein surface.^{20,38-40}

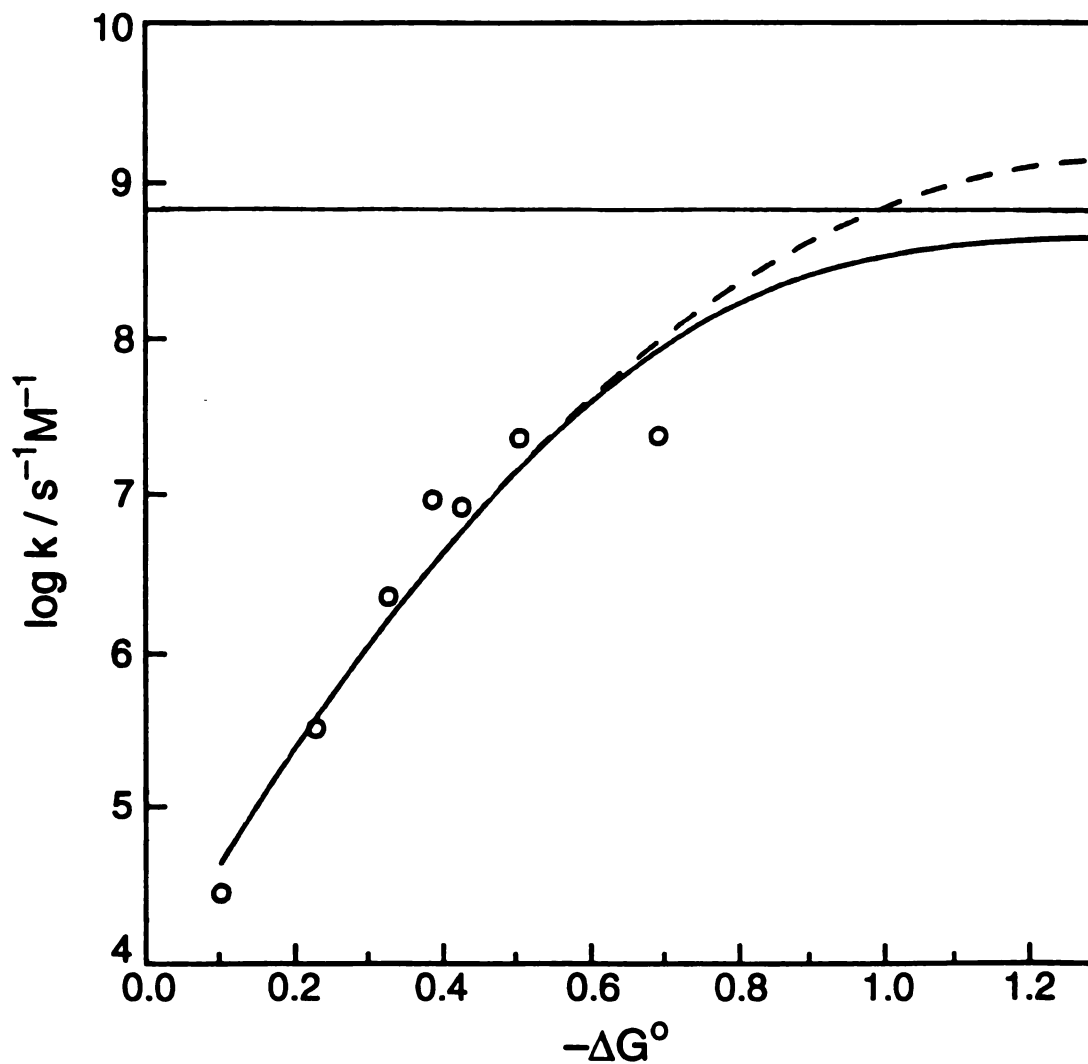


Figure 46. Plot of the data points from Ref. 52, showing the calculated rates, k_{obs} (solid curve) and k_{act} (dashed curve). The diffusion limit, k_{diff} , is shown at $7.1 \times 10^8 \text{ M}^{-1} \text{ s}^{-1}$.

The explanation for the observation of the inverted region in the ET reaction between the cationic complexes and cytochrome *c* is twofold: the relatively small value of k_{act} in relation to the rate of diffusion and the moderate value of the reorganization energy. The latter can be explained in that in organic systems the inner reorganization energy contributes greatly to the total value of λ ,^{2,3} whereas in ET reactions involving proteins and inorganic complexes most of the contributions are from the solvent. The combination of these two factors leads to the observation of the inverted region in bimolecular reactions. Other systems for which the reorganization energy is small or the intrinsic rate of ET is slow, perhaps due to large donor/acceptor separations, should also exhibit this behavior.

E. REFERENCES

1. (a) Marcus, R. A. *J. Chem. Phys.* **1956**, *24*, 966. (b) Marcus, R. A. *Ann. Rev. Phys. Chem.* **1964**, *15*, 155.
2. (a) Closs, G. L.; Calcaterra, L. T.; Green, N. J.; Penfield, K. W.; Miller, J. R. *J. Phys. Chem.* **1986**, *90*, 3673. (b) Closs, G. L.; Miller, J. R. *Science* **1988**, *240*, 440.
3. Beitz, J. V.; Miller, J. R. *J. Chem. Phys.* **1979**, *71*, 4579.
4. (a) McLendon, G.; Miller, J. R. *J. Am. Chem. Soc.* **1985**, *107*, 7811. (b) McLendon, G.; Pardue, K.; Bak, P. *J. Am. Chem. Soc.* **1987**, *109*, 7540. (c) Conklin, K. T.; McLendon, G. *J. Am. Chem. Soc.* **1988**, *110*, 3345. (d) Bashkin, J. S.; McLendon, G. In *Electron Transfer in Biology and the Solid State*; Johnson, M. K.; King, R. B.; Kurtz, Jr., D.

- M.; Kutal, C.; Norton, M. L.; Scott, R. A., Eds.; *Advances in Chemistry Series 226*; American Chemical Society: Washington, D.C., 1990; pp 147-159. (e) McLendon, G.; Hake, R. *Chem. Rev.* **1992**, *92*, 481.
5. (a) Zhou, J. S.; Granada, E. S. V.; Leontis, N. B.; Rodgers, M. A. J. *J. Am. Chem. Soc.* **1990**, *112*, 5074. (b) Zhou, J. S.; Rodgers, M. A. J. *J. Am. Chem. Soc.* **1991**, *113*, 7728.
 6. (a) Elias, H.; Chou, M. H.; Winkler, J. R. *J. Am. Chem. Soc.* **1988**, *110*, 429. (b) Meade, T. J.; Gray, H. B.; Winkler, J. R. *J. Am. Chem. Soc.* **1989**, *111*, 4353.
 7. (a) Cho, K. C.; Che, C. M.; Cheng, F. C.; Choy, C. L. *J. Am. Chem. Soc.* **1984**, *106*, 6843. (b) Cho, K. C.; Che, C. M.; Ng, K. M.; Choy, C. L. *J. Am. Chem. Soc.* **1986**, *108*, 2814. (c) Cho, K. C.; Ng, K. M.; Choy, C. L.; Che, C. M. *Chem. Phys. Lett.* **1986**, *129*, 521.
 8. Cleskey, T. M.; Winkler, J. R.; Gray, H. B. *J. Am. Chem. Soc.*, submitted for publication
 9. Juris, A.; Balzani, V.; Barigelletti, F.; Campagna, S.; Belser, P.; Von Zelewsky, A. *Coord. Chem. Rev.* **1988**, *84*, 85 and references therein.
 10. (a) Wherland, S.; Gray, H. B. *Proc. Natl. Acad. Sci. USA* **1976**, *73*, 2950. (b) Wherland, S.; Gray, H. *In Biological Aspects of Inorganic Chemistry*; Addison, A. W.; Cullen, W. R.; Dolphin, D.; James, B. R., Eds.; Wiley-Interscience: New York, 1977; pp 289 - 368. (c) Cummins, D.; Gray, H. B. *J. Am. Chem. Soc.* **1977**, *99*, 5158 (d) Mauk, A. G.; Scott, R. A.; Gray, H. B. *J. Am. Chem. Soc.* **1980**, *102*, 4360. (e) Cummins, D.; Gray, H. B. *Inorg. Chem.* **1981**, *20*, 3712.
 11. Guarr, T.; McLendon, G. *Coord. Chem. Rev.* **1985**, *68*, 1.
 12. Marcus, R. A.; Sutin, N. *Biochim. Biophys. Acta* **1985**, *811*, 265.

13. Balzani, V.; Moggi, L.; Manfrin, M. F.; Bolletta, F. *Coord. Chem. Rev.* **1975**, *15*, 321.
14. Marcus, R. A.; Siders, P. *J. Phys. Chem.* **1982**, *86*, 622.
15. (a) Sutin, N. *Acc. Chem. Res.* **1982**, *15*, 275. (b) Newton, M. D.; Sutin, N. *Ann. Rev. Phys. Chem.* **1984**, *35*, 437.
16. Debye, P. *Trans. Electrochem. Soc.* **1942**, *82*, 265.
17. Noyes, R. M. *Prog. React. Kinet.* **1961**, *1*, 129.
18. Steinfeld, J. I.; Francisco, J. S.; Hase, W. L. *Chemical Kinetics and Dynamics*; Prentice Hall: New Jersey; 1989; pp 156 - 168.
19. (a) Ulstrup, J.; Jortner, J. *J. Chem. Phys.* **1975**, *63*, 4358. (b) Jortner, J. *J. Chem. Phys.* **1976**, *64*, 4860.
20. Winkler, J. R.; Gray, H. B. *Chem. Rev.* **1992**, *92*, 369.
21. Churg, A. K.; Weiss, R. M.; Warshel, A.; Takano, T. *J. Phys. Chem.* **1983**, *87*, 1683.
22. Brautigan, D. L.; Ferguson-Miller, S.; Margoliash, E. *Methods Enzymol.* **1978**, *53*, 128.
23. Stellwagen, E.; Cass, R. D. *J. Biol. Chem.* **1975**, *250*, 2095.
24. Vanderkooi, J. M.; Adar, F.; Erecinska, M. *Eur. J. Biochem.* **1976**, *64*, 381.
25. Wikström, M.; Krab, K.; Saraste, M. In *Cytochrome Oxidase: A Synthesis*; Academic Press: New York, 1981.
26. Snyder, H. R.; Freier, H. E. *J. Am. Chem. Soc.* **1946**, *68*, 1320.
27. Rund, J. V.; Claus, K. G. *J. Am. Chem. Soc.* **1967**, *89*, 2256.
28. Krause, R. A. *Inorg. Chim. Acta* **1977**, *22*, 209.
29. Newsham, M. D.; Giannelis, E. P.; Pinnavaia, T. J.; Nocera, D. G. *J. Am. Chem. Soc.* **1988**, *110*, 3885.

30. The average radius is 6.5 Å for all the positively-charged complexes studied here, which range from 5.8 to 7.2 Å.⁹
31. Hemmes, P. *J. Am. Chem. Soc.* **1972**, *94*, 75.
32. Morikis, D.; Li, P.; Bangcharoenpaurpong, O.; Sage, J. T.; Champion, P. M. *J. Phys. Chem.* **1991**, *95*, 3391.
33. The density of states was chosen to be 6, since at high driving force (1.30 V) the calculated ET rate ceased to change above this value.
34. Integration of Equations 14 and 19 was performed numerically utilizing the trapezoidal method, with distance limits from closest contact to 30 Å and 5000 integration points.
35. Beratan, D. N.; Betts, J. N.; Onuchic, J. N. *Science* **1991**, *252*, 1285.
36. Conrad, D. W.; Scott, R. A. *J. Am. Chem. Soc.* **1989**, *111*, 3461.
37. With $\beta = 2.0 \text{ \AA}^{-1}$ in the Ru(NH₃)₅Ru^{II}(His33)–Fe–cyt. c system (Ref. 20).
38. (a) Butler, J.; Davies, D. M.; Sykes, A. G.; Koppenol, W. H.; Osheroff, N.; Margoliash, E. *J. Am. Soc.* **1981**, *103*, 469. (b) Butler, J.; Koppenol, W. H.; Margoliash, E. *J. Biol. Chem.* **1982**, *257*, 10747. (c) Butler, J.; Chapman, S. K.; Davies, D. M.; Sykes, A. G.; Speck, S. H.; Osheroff, N.; Margoliash, E. *J. Biol. Chem.* **1983**, *258*, 6400.
39. Armstrong, G. D.; Chambers, J. A.; Sykes, A. G. *J. Chem. Soc. Dalton Trans.* **1986**, 755.
40. Drake, P. L.; Hartshorn, R. T.; McGinnis, J.; Sykes, A. G. *Inorg. Chem.* **1989**, *28*, 1361.
41. Wuttke, D. S.; Bjerrum, M. J.; Winkler, J. R.; Gray, H. B. *Science*, **1992**, *256*, 1007.
42. Toma, H. E.; Murakami, R. A. *Inorg. Chim. Acta* **1984**, *93*, L33.

43. Sakaki, S.; Nishijima, Y.; Ohkubo, K. *J. Chem. Soc. Dalton Trans.* **1991**, 1143.
44. Marinov, B. S.; Gerasimenko, V. V. *Photochem. Photobio.* **1985**, *41*, 217.
45. Therien, M. J.; Selman, M.; Gray, H. B.; Chang, I-J.; Winkler, J. R. *J. Am. Chem. Soc.* **1990**, *112*, 2420.
46. Dixon, D. W.; Hong, X.; Woehler, S. E.; Mauk, A. G.; Sishta, B. P. *J. Am. Chem. Soc.* **1990**, *112*, 1082.
47. Zhou, J. S.; Kostic, N. M. *J. Am. Chem. Soc.* **1991**, *113*, 6067.
48. Meyer, T. E.; Przysiecki, C. T.; Watkins, J. A.; Bhattacharyya, A.; Simonsen, R. P.; Cusanovich, M. A.; Tollin, G. *Proc. Natl. Acad. Sci. USA* **1983**, *80*, 6740.
49. Wasielewski, M. R.; Niemczyk, M. P.; Svec, W. A.; Pewitt, E. B. *J. Am. Chem. Soc.* **1985**, *107*, 1080.
50. Chung, W.-S.; Turro, N. J.; Gould, I. R.; Farid, S. *J. Phys. Chem.* **1991**, *95*, 7752.
51. Isied, S. S.; Vassilian, a.; Wishart, J. F.; Creutz, C.; Schwarz, H. A., Sutin, N. *J. Am. Chem. Soc.* **1988**, *110*, 635.
52. Magner, E.; McLendon, G. *J. Phys. Chem.* **1989**, *93*, 7130.

APPENDIX

Table AI. IR Absorbances of DNBCOOH Utilized in the Self-Association Binding Constant Calculations Described in Chapter I.

| [DNBCOOH] (mM) | Absorbance | | |
|----------------|-----------------------|-----------------------|-----------------------|
| | 1751 cm ⁻¹ | 1715 cm ⁻¹ | 3478 cm ⁻¹ |
| 1.57 | 0.238 | 0.045 | 0.036 |
| 1.26 | 0.191 | 0.031 | 0.032 |
| 0.942 | 0.150 | 0.020 | 0.024 |
| 0.628 | 0.107 | 0.011 | 0.016 |
| 0.392 | 0.077 | 0.008 | 0.012 |

Table AII. IR Absorbances of ZnPCOOH Utilized in the Self-Association Binding Constant Calculations Described in Chapter I.

| [ZnPCOOH] (mM) | Absorbance | | |
|----------------|-----------------------|-----------------------|-----------------------|
| | 1744 cm ⁻¹ | 1713 cm ⁻¹ | 3489 cm ⁻¹ |
| 1.59 | 0.046 | 0.041 | 0.012 |
| 1.27 | 0.037 | 0.031 | 0.010 |
| 0.954 | 0.029 | 0.023 | 0.007 |
| 0.636 | 0.024 | 0.018 | 0.006 |
| 0.398 | 0.019 | 0.009 | 0.005 |

Table AIII. IR Absorbances of ZnPCOOH and DNBCOOH Utilized in the Hetero-Association Binding Constant Calculation Described in Chapter I.

| [ZnPCOOH] (mM) | Absorbance | | Absorbance 1751 cm ⁻¹ |
|----------------|-----------------------|----------------|-------------------------------------|
| | 1744 cm ⁻¹ | [DNBCOOH] (mM) | |
| 0.666 | 0.119 | 0.739 | 0.195 |
| 0.521 | 0.097 | 0.615 | 0.160 |
| 0.312 | 0.055 | 0.340 | 0.090 |
| 0.247 | 0.038 | 0.214 | 0.060 |

MICHIGAN STATE UNIV. LIBRARIES



31293007949831